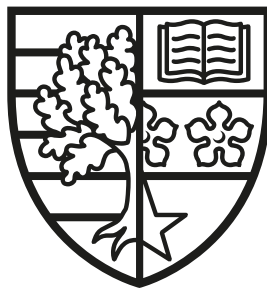# Advanced Data Acquisition For Multi-Photon Experiments

Peter Barrow

SUBMITTED FOR THE DEGREE OF

DOCTOR OF PHILOSOPHY

HERIOT-WATT UNIVERSITY

DEPARTMENT OF PHYSICS,

SCHOOL OF ENGINEERING AND PHYSICAL SCIENCES.

October, 2020

Abstract

The overarching theme of this thesis was to develop a state-of-the-art multi-photon experiment at telecom wavelengths. With this platform the following experiments in quantum information processing were performed: testing of local observer independence [1], multiqubit phase estimation [2], measurement-device-independent verification of quantum channels [3], assisted macroscopic quantumness [4] and experimental quantum conference key agreement [5]. My focus has been primarily on the signal processing / data analysis required in particular for the required engineering for the used single-photon sources [6] developed by our group and most prominently for the "big data" produced in measurement of the joint spectra such as our demonstration of time-frequency modes from engineered nonlinearites [7]. The analysis required for our source engineering efforts has resulted in the my development of a pair of models to determine accurate multi-photon detection rates and signal-to-noise ratios of each single-photon source. In order to extract the joint spectra from the measured "big data" I have developed a time-correlated single-photon counting toolkit. In this thesis I will outline the following, the requirements for building a high performance single-photon source, develop a pair of models for analysing the signal-to-noise ratio for a number of sources along with exploring the benefits that can be seen via multiplexing. Further, the design of time-correlated single-photon-counting hardware is discussed along with the methods needed to produced meaningful analytics from the data output from said hardware. Finally the joint spectra of a number of down-conversion based single-photon sources are reconstructed via dispersive spectroscopy allowing for the spectral purity to be estimated in each case, this is then extended by use of image processing techniques in order to determine whether our estimates can be improved. In all, this thesis discusses what we need from a single-photon source, how to optimise the experimental configuration for high detection rates and signal-to-noise ratios, how to analyse the resulting signals and then finally combining these into measurement of spectral purity resulting in a broad investigation of single-photon source performance with a view to multi-photon experiments.

Acknowledgements

HERIOT WATT UNIVERSITY

Research Thesis Submission

Please note this form should be bound into the submitted thesis.

Name*:*	Peter Barrow		
School:	EPS		
Version: *(i.e. First, Resubmission, Final)*	Final	Degree Sought:	PhD in Physics

Declaration

In accordance with the appropriate regulations I hereby submit my thesis and I declare that:
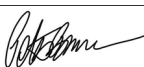
1. The thesis embodies the results of my own work and has been composed by myself
2. Where appropriate, I have made acknowledgement of the work of others
3. The thesis is the correct version for submission and is the same version as any electronic versions submitted*.
4. My thesis for the award referred to, deposited in the Heriot-Watt University Library, should be made available for loan or photocopying and be available via the Institutional Repository, subject to such conditions as the Librarian may require
5. I understand that as a student of the University I am required to abide by the Regulations of the University and to conform to its discipline.
6. I confirm that the thesis has been verified against plagiarism via an approved plagiarism detection application e.g. Turnitin.

ONLY for submissions including published works

Please note you are only required to complete the Inclusion of Published Works Form (page 2) if your thesis contains published works)

7. Where the thesis contains published outputs under Regulation 6 (9.1.2) or Regulation 43 (9) these are accompanied by a critical review which accurately describes my contribution to the research and, for multi-author outputs, a signed declaration indicating the contribution of each author (complete)
8. Inclusion of published outputs under Regulation 6 (9.1.2) or Regulation 43 (9) shall not constitute plagiarism.

*   *Please note that it is the responsibility of the candidate to ensure that the correct version of the thesis is submitted.*

Signature of Candidate*:*		Date:	01/10/2020

Submission

Submitted By (name in capitals):	Peter Barrow
Signature of Individual Submitting:	
Date Submitted:	01/10/2020

For Completion in the Student Service Centre (SSC)

Limited Access	Requested	Yes		No		Approved	Yes		No	
*E-thesis Submitted (**mandatory for final theses**)*										
Received in the SSC by (name in capitals):					Date:					

Inclusion of Published Works

Declaration

This thesis contains one or more multi-author published works. In accordance with Regulation 6 (9.1.2) I hereby declare that the contributions of each author to these publications is as follows:

Citation details	Proietti M, Pickston A, Graffitti F, Barrow P, Kundys D, Branciard C, Ringbauer M, Fedrizzi A. Experimental test of local observer independence. Science advances. 2019 Sep 1;5(9):eaaw9832.
Author 1, Author 2, Author 3, Author 4, Author 5	Performed the experiment and collected the data.
Author 1, Author 3	Analysed the data.
Author 7, Author 8, Author 6	Conceived the project and designed the experiment.
Author 6	Developed the theory results.
Signature:	
Date:	01/10/2020

Citation details	Proietti M, Ringbauer M, Graffitti F, Barrow P, Pickston A, Kundys D, Cavalcanti D, Aolita L, Chaves R, Fedrizzi A. Enhanced multiqubit phase estimation in noisy environments by local encoding. Physical review letters. 2019 Nov 1;123(18):180503.
Author 1, Author 2, Author 3, Author 4, Author 5, Author 6	Characterised the experimental setup.
Author 1, Author 2	Designed and performed the experiment, collected and analysed the data.
Author 10	Conceived the project.
Author 7, Author 8, Author 9	Developed the theory results.
Signature:	
Date:	01/10/2020

Citation details	Shahandeh F, Ringbauer M, Proietti M, Costa F, Lund AP, Graffitti F, Barrow P, Pickston A, Kundys D, Ralph TC, Fedrizzi A. Assisted Macroscopic Quantumness. arXiv preprint arXiv:1711.10498. 2017 Nov 28.
Author 2, Author 3, Author 6, Author 7, Author 8, Author 9	Designed and performed the experiment, collected and analysed the data.
Author 1, Author 4, Author 5	Developed the theory results.
Author 11, Author 12	Conceived the project.
Signature:	
Date:	01/10/2020

Citation details	Proietti M, Ho J, Grasselli F, Barrow P, Malik M, Fedrizzi A. Experimental quantum conference key agreement. arXiv preprint arXiv:2002.01491. 2020 Feb 4.
Author 1, Author 2, Author 4	Designed and performed the experiment.
Author 1, Author 2	Collected and analysed the data.
Author 3	Developed the theory results.
Author 5, Author 6	Conceived the project.
Signature:	
Date:	01/10/2020

Citation details	Graffitti F, Barrow P, Proietti M, Kundys D, Fedrizzi A. Independent high-purity photons created in domain-engineered crystals. Optica. 2018 May 20;5(5):514-7.
Author 1, Author 2, Author 3, Author 4	Designed and performed the experiment, collected and analysed the data.
Author 1	Developed the theory results.
Author 5	Conceived the project.
Signature:	
Date:	01/10/2020

Citation details	F. Graffitti, P. Barrow, A. Pickston, A. M. Bra ńczyk, and A. Fedrizzi, Direct Generation of Tailored Pulse-Mode Entanglement, Physical Review Letters 124 (2020) 053603
Author 1, Author 2, Author 3	Designed and performed the experiment, collected and analysed the data.
Author 1, Author 4	Developed the theory results.
Author 5	Conceived the project.
Signature:	
Date:	01/10/2020

Contents

Chapter 1

Introduction

Quantum technologies exploit the quantum principles of superposition and entanglement, promising to solve problems insurmountable to their classical counterparts, such as faster computation of classically hard problems, more precise sensors and encryption that can't be broken by current means. A wide variety of physical systems are being investigated for their use in quantum technologies. Amongst these, quantum photonics with single photons is currently a lead candidate because it can be applied to all areas of quantum information processing (QIP); computing, simulation, communication and metrology. In particular, since photons can be distributed over long distances either over free-space or existing telecommunications fibre networks it is and will remain the only suitable candidate for quantum communication.

A quantum photonics experiment broadly consists of three building blocks, the generation of quantum light, its coherent interaction, and, ultimately, its detection. The appeal of quantum photonics, and one reason it is so widespread, has long been that all three building blocks are relatively easy to implement. Components are comparably cheap, and it is straightforward to generate, manipulate and detect light even at the single-photon level. Since single photons do not couple to their environment, coherence is maintained almost indefinitely. However, this apparent ease of use comes with a significant drawback: all three building blocks, as currently implemented, are probabilistic in nature. Single-photon sources mostly emit either nothing at all or sometimes more than just one photon, two-photon interactions are, due to a lack of deterministic nonlinear gates, realised via probabilistic interference effects in linear optics, and photon detection will, while detectors have advanced

drastically, never reach 100% efficiency due to inevitable optical loss.

Nevertheless, there is a route to scalability which will overcome these problems; by multiplexing sources or making them deterministic, by loss-encoding with either massive overheads such as in the KLM scheme [8], or by cluster percolation [9] and by further developing and integrating already highly efficient detectors.

The overarching theme of this thesis was the development of state-of-the-art multi-photon experiments at telecom wavelengths. With this platform the following experiments in quantum information processing were performed: assisted macroscopic quantumness [4], testing of local observer independence [1], multiqubit phase estimation [2], measurement-device-independent verification of quantum channels [3], experimental quantum conference key agreement [5]. My focus has been primarily on the signal processing / data analysis required in particular for the required engineering for the used single-photon sources [6] and most prominently for the "big data" produced in measurement of the joint spectra such as our demonstration of time-frequency modes from engineered nonlinearites [7].

In order to achieve this the development of single-photon sources has been key with my focus primarily being that of signal processing and data analysis required for the creation of useful analytics surrounding the experimental configurations. As a result the thesis is organised as follows:

In chapter 2 we will start with a technical foundation, discussing the background of the above mentioned building blocks for quantum light creation $\rightarrow$ manipulation $\rightarrow$ detection. This will include an in-depth section on heralded photon sources, parametric downconversion theory, and an overview of current source and photon detector technology.

This is followed by defining a pair of models in chapter 3 to explore the effects of loss and those produced in having components with fixed reset times. Here we will include validation against measurements to assess their suitability.

Next in chapter 4 we will tackle the topic of speed limits present in quantum photonic experiments by using the models developed in the previous chapter. Included here is exploration of some of the key relations such as whether or not it an experiments clock rate should be faster than that of what can be observed by the detectors. Finally we will complete a global sensitivity analysis to determine out of

each of the features we have modelled has the greatest effect when considering the signal recorded and its associated signal to noise ratio.

Further in chapter 5 we give a full treatment of time correlated single photon counting (TCSPC) from the hardware required as well how the software needed to operate on the data produced should be constructed providing a general prescription of how to implement operations on the data.

Finally chapter 6 covers the measurement of the joint spectral intensity (JSI) of a bi-photon state, to do so we draw on the work in chapters 3 to 5 such that we have ideal conditions to conduct the experiment as well the tools to construct the JSI data. With this we cover the generation, detection and analysis of how to create photons that are pure in both their number and spectral degrees of freedom. chapter 7 closes the work presented with the application of image processing techniques applied to the reconstructed joint spectral intensity measurement of chapter 6 in order to improve estimations of spectral purity.

Chapter 2

Building Blocks of Quantum Photonics

To begin building a quantum photonics platform we must first consider the methods to generate single-photons. Single-photon sources have been developed since the 1970s [10], there are two broad categories, either probabilistic or deterministic single-photon sources. Where probabilistic sources require the generation of a pair of single-photons in which one of them is used to herald the existence of the other, defining our "single-photon". For the purpose of this thesis we will focus on probabilistic generation methods.

The ideal single-photon source has the following characteristics: it emits one — and only one — photon per trigger event, in a pure quantum state, at high brightness, i.e. the ability to emit a single-photon for a very small input powers. For photon pair sources, brightness is defined as the number of photon pairs per milliwatt of power used to trigger emission. An additional, desirable criterion, is a centre wavelength of 1550 nm and a reasonably narrow bandwidth. This would guarantee compatibility with telecom fibre infrastructure, including components such as wavelength-division multiplexers etc. with minimal loss and dispersion, and ultimately narrow-band quantum memories.

Single quantum emitters are artificial two-level structures that emit ideally one and only one single photon. These emitters can be constructed in semiconductors as quantum dots [11, 12], nitrogen vacancies [13] in diamond or other materials, individual trapped atoms [14, 15] or ions [16], molecules [17, 18] and more. Typically

each of the technologies listed here rely on similar operating principles where for single-photon emission the emitter is placed into an excited state via some external control system, relaxation from this excited state provides the emission. Whilst they promise near deterministic emission simultaneously achieving high output coupling into a fibre remains a key challenge in their development — the best examples make use of cavity designs using the Purcell effect [19, 20] while maintaining high brightness [21], a low $g^{(2)}(0)$ [22] and spectral purity, or indistinguishability [23]. In particular, despite much progress including with individual tunability, interference between dots remains of poor quality. However, there has been significant success with photons demultiplexed from individual dots [24, 25], taking multiple emissions from the same quantum dot and separating them over multiple spatial channels.

Ever since the first demonstration of a cascade emission [10, 26, 27] photon pair sources have been the driving force of experimental QIP, gaining increased interest with the first source of entanglement in nonlinear parametric downconversion [28, 29], where one photon of a pump laser converts into two lower energy photons maintaining conversation of energy and momentum. Photon pair sources can deliver very high brightnesses, are flexible in terms of operation wavelength and tunability and have been used to demonstrate many firsts in quantum photonics such as that of teleportation [30], the first three-particle entanglement [31], and can now the ability to entangle up to 12 photons [32]. However, a major drawback is that the probability to generate a photon pair is low, and while it can be increased by pumping with higher power, this leads to a concurrent decrease in the signal-to-noise ratio due to the probabilistic nature of emission. As a result both the single pair and multiple pair emission probabilities increase with increasing pump power, this will be discussed in detail later on.

Commonly, when discussing photon-pair sources, the polarisation basis is used to for manipulation of photons however other degrees of freedom (DOFs) are available for this task. These include: orbital angular momentum (OAM), time-bins [1], frequency as well as spatial and/or longitudinal modes. This thesis focuses primarily on polarisation based entanglement, reporting on the novel use of time-frequency modes in chapter 6.

---

[1]The temporal position of a photon can be shifted such that there exists both an "early" and a "late" arrival time for each photon.

Two-photon interactions are a much harder problem to overcome, since photon-photon interaction is much too weak to be exploited directly. Methods to interact with one or more photons can be described as making use of either linear, consisting of devices like beamsplitters and phase shifters, or nonlinear optical elements such utilisation of the Kerr effect or frequency mixing. The primary method is to use Hong-Ou-Mandel interference [33] with linear optical components, an effect causing identical photons that arrived at the input ports of a symmetric beamsplitter simultaneously to both exit at the same output port. This is the basis of all of optical QIP, however it leads to limited success probabilities which will have to overcome at the cost of overheads.

After manipulating our single photons we need single photon detectors to signal the creation and manipulation of photons within our experiment. It has been common place to employ semiconductor avalanche photo diodes in this role providing us up to around 60% detection efficiency at around $700 - 800$nm, with this efficiency getting much worse in InGaAs based diodes at telecom wavelengths. However, with the advent of superconducting detector technologies [34, 35] higher efficiencies are obtainable when operating at telecoms wavelengths. Further detectors making use of the transition between the normal and superconducting states (Transition edge sensors, (TES)) can reach near unity detection efficiency as well as determine the total number of photons that arrived simultaneously (photon-number resolution). This unfortunately comes with typical detector reset times of the order of microseconds, a limitation when high use of fast (MHz to GHz) signals. However superconducting nanowire single photon detectors (SNSPDs) possess reset times of a few tens of nanoseconds as well as beginning to approach 90% detection efficiency [36]. Further, by using an array of SNSPDs partial photon-number resolution is achievable [37]

This lack of determinism across the three basic building blocks of quantum photonics ultimately leads to scalable QIP being a difficult goal to achieve. In particular, it is clear that if a single photon is created, manipulated correctly, and detected with probability p, a generic N-photon QIP protocol will be successful with probability p^N, which will be near zero for anything other than p being very close to 1 or N being small. With this in mind various schemes have been developed to enable scalable linear-optical QIP schemes and universal linear optical quantum computers in

particular. Possibly the most famous of these proposed schemes is the KLM protocol, named after its inventors Knill, Laflamme and Milburn [8]. The KLM scheme can overcome the probabilistic nature of linear-optics two-photon interactions by making use of entangled single photons states, extra (ancilla) photons and quantum teleportation which allows to "carry forward" successful outcomes into the processing line by the teleportation process. In short, even though two-photon interference must be used, the inclusion of entanglement and teleporting successful results onto the ancilla (the processing line) allows us to get closer to unity success probabilities. The KLM protocol formed the basis for a proliferation of efforts into linear optics research. However, while it did provide a route to scalability for linear optical quantum technology, it was always clear that it was not the most practical due to a large overhead resource cost in the form of ancilla photons, additional interactions, and required classical feed forward stages.

Raussendorf [9] *et al* proposed the idea of quantum computation executed over cluster states as an implementation of measurement based quantum computing (MBQC [38–43]). Cluster states provide an alternative where instead of successive application of a series of one- and two-photon gates in the so-called circuit model, we build up a quantum state with a high degree of entanglement between each of its constituent photons and proceed to apply a series of measurements to it after creation to complete our information processing. Under this regime the overhead is now replaced with the challenge of constructing such a state. Under this scheme we eschew the large network of optical elements for a large network of entangled photons, with such a network we can then proceed to measure individual photons within the network, performing our processing as we do so. To pick a more desirable scheme to complete our quantum information processing means considering which is more scalable, construction of a large optical network or construction of a large network of entangled photons.

Working in the direction of *creation → manipulation → detection* of quantum light, we will first review some background theory on single-photon sources followed by detectors and then finally the processing of detection events. From fig. 2.1 we detail a typical laboratory scenario where we have a pump laser, some number of photon sources, our photonic circuit finalised with our detection and processing.
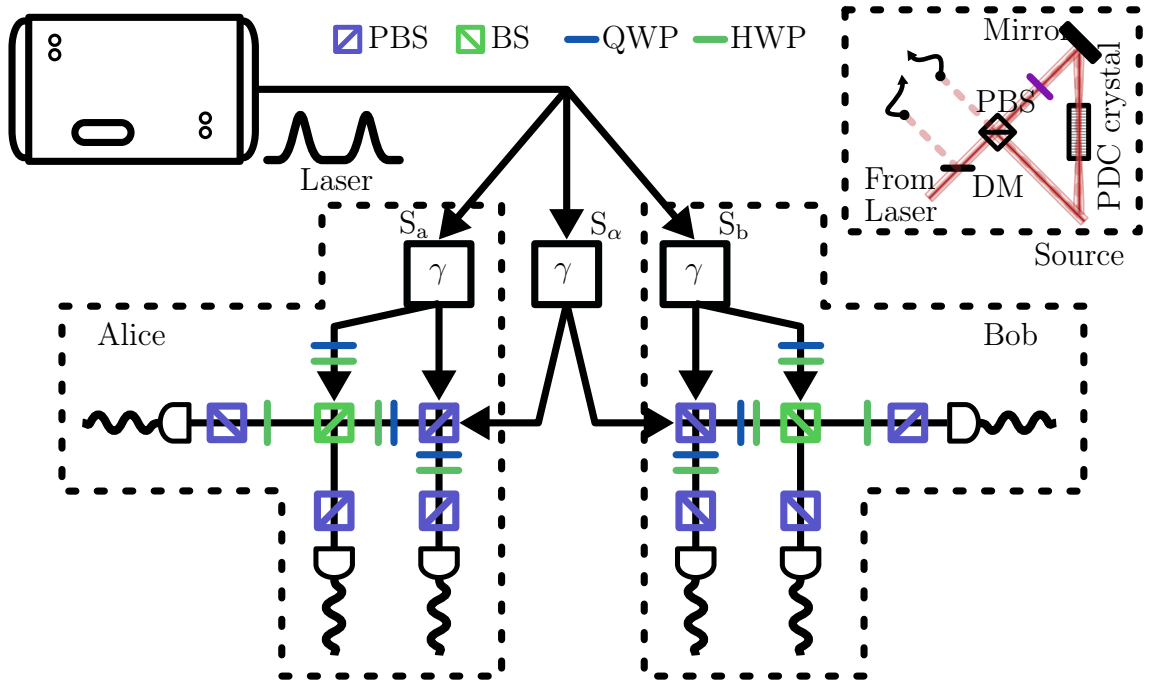
Figure 2.1: **The three building blocks for quantum photonics.** Replication of experimental scheme seen in [1], whereby a six photon experimental scheme was developed to test local observer independence. *Creation* : A laser pumps each of the sources, $S_{a,b,\alpha}$, generating pairs of entangled photons. *Manipulation* : Alice and Bob manipulate their own along with one photon each from the pair emitted by S_α. They do this though linear optical elements, in the form of beamsplitters, half-wave plates and quarter-wave plates. *Detection* : Each photon is detected by a separate detector and each detector output is processed by a timing device to determine if the generation and manipulation performed was successful.

2.1 Photon Sources

For photonics to be a suitable QIP platform a significant amount of attention must be afforded to how we create single photons. Single photon sources that emit photons only when triggered and each emitted photon must be indistinguishable from all previous and successively emitted photons from both the source they are emitted from as well all other sources. As such development of single photon sources has undergone continuous development since their inception.

Further we should take care to note that due to extraction losses (e.g. when trying to couple the light generated from a quantum dot held in cryostat, the required optics are not perfect) even sources with deterministic photon generation can be subject to probabilistic emission.

Categorising the realisation of single photon sources into either being single quan-
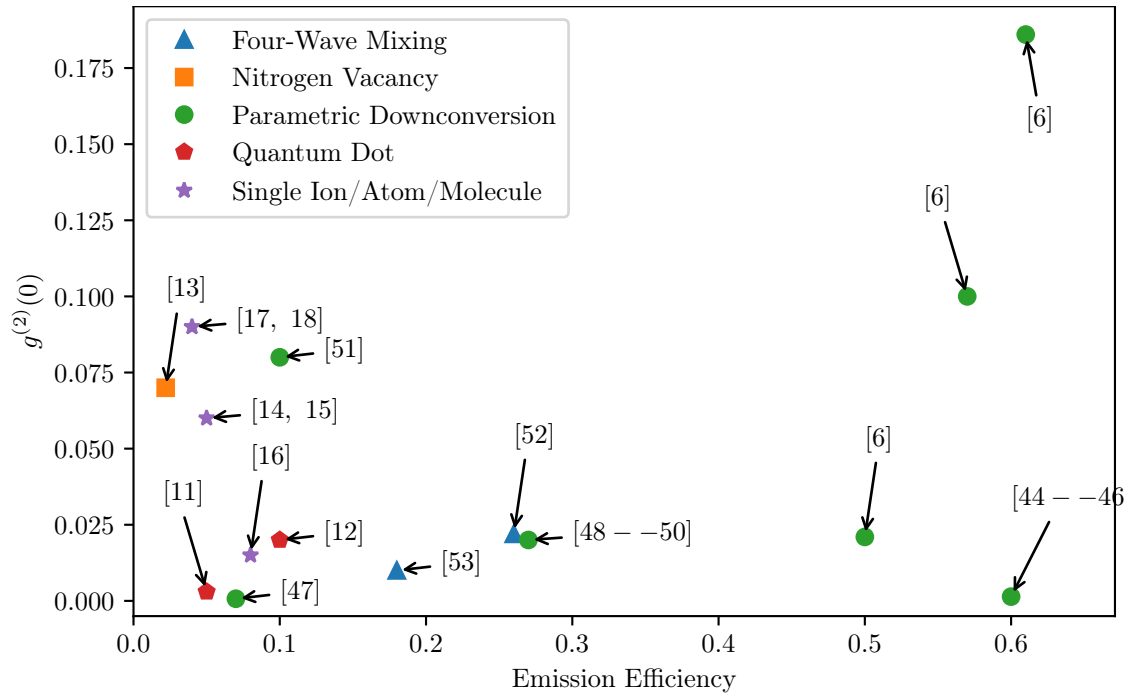
Figure 2.2: **Comparison between emission efficiency and** $g^{(2)}(0)$ **of a range of single-photon sources.** Detection efficiency represents how close a source is to be able to emit a photon every time we trigger it. Measuring $g^{(2)}(0)$ allows us to determine how pure the sources emission is in terms of the photon number. With these two values we can compare how well a source performs with the ideal source having as high an emission efficiency and as low a $g^{(2)}(0)$ as possible, under these conditions we would have one and only one photon every time we trigger the source.

tum emitters or parametric optical processes, consisting of the likes of quantum dots, nitrogen vacancy (NV) centres and trapped ions or parametric downconversion (PDC) and four-wave mixing (FWM), respectively, provides us a basis to consider how we want to build and utilise our source. In the realm of single quantum emitters it is possible to achieve a deterministic stream of single photons, producing an output each time the emitter is excited. Single emitters, such as quantum dots (QD), currently have the capability to produce high number and spectral purities along with high indistinguishability making them ideal in terms of performance as single-photon source [54]. Whilst QD based devices have suffered from low extraction efficiencies reducing the total rate of single-photons observed in the past, recent developments have resolved this allowing for extraction efficiencies > 70% [23, 55–60] by combining the QD with a nanoresonator. Further QDs have proven to be a powerful platform for multi-photon experiments [61, 62], so far allowing for the realisation of 20-photon experiments [63] by making use of active switching to de-

multiplex [25] the stream of single-photons into separate paths. Whilst QDs are a promising platform for QIP the focus here is with PDC based sources.

As for parametric optical processes, like PDC and FWM, the reliance on nonlinear processes results in probabilistic emission. This probabilistic nature includes not only the successful emission of photons from the source but also the number of photons emitted. Ideally in a PDC based source the emission of one and only one pair of photons would be the ideal case, from there one photon of the pair can be used to herald the existence of the other. However, in practice there exists the possibility of emitting more than one pair of photons. In order to characterise the probability of multi-photon emission from a single-photon source it is common to measure the second-order coherence, $g^{(2)}$, for PDC sources this is achieved by heralding one photon of each pair whilst directing its counterpart to a beamsplitter with detectors on both output ports. From the number of coincident detection events at both output ports of the beamsplitter it is possible to determine the number of multi-photon generation events that have occurred compared to the number of single pair generation events. A comparison between emission efficiency and second-order coherence can be seen in fig. 2.2 for a range of different types of single-photon sources. It has been shown by Christ *et-al.* [64] that the probabilistic nature of PDC sources can be overcome to achieve $> 99\%$ single-photon emission probability by use of 17-PDC sources, an N:1 switch and photon-number resolving detectors.

2.1.1   Source Brightness and Efficiency

To define fully the brightness of a PDC source and better define its efficiency we must first detail the quantum state created by the PDC source. Using the creation and annihilation operators, $a^\dagger$ and $b^\dagger$ for the signal and idler modes:

$$|n\rangle_i = \frac{(a^\dagger)^n}{\sqrt{n!}}|0\rangle_i \tag{2.1}$$

$$|n\rangle_s = \frac{(b^\dagger)^n}{\sqrt{n!}}|0\rangle_s \tag{2.2}$$

Here $|0\rangle_{i,s}$ represents the vacuum for both the signal and idler modes allowing us to represent the PDC state in terms of photon number as [65]:

$$|\psi_{\text{PDC}}\rangle = \sqrt{1 - \lambda^2} \sum_{n=0}^{\infty} \lambda^n |n\rangle_s |n\rangle_i, \tag{2.3}$$

with λ containing information about the nonlinear interaction and pump power and n representing the photon number. The interaction between the pump light and the nonlinear PDC medium along with the dependence on pump power are expressed through $\lambda = \sqrt{\gamma P}$ by γ and P respectively. This is an extension of the following representation $\lambda = \xi \tau$ found when deriving eq. (2.3) from the Hamiltonian describing the PDC process [65]:

$$\hat{H} = i\xi\hbar \left(\hat{a}_1^\dagger \hat{b}_1^\dagger + \text{h.c.} \right) \tag{2.4}$$

Here ξ encapsulates the nonlinear interaction strength present along with details of the pump lasers spectral properties.

We move to a picture in which we have the average pump power in P and have γ contain the information pertaining to spectral properties and interaction time, the effects of which will be the subject of chapter 4. From eq. (2.3) we can see that it is possible to have more than a single pair of photons emitted, we typically consider these higher order emissions as a source of noise causing a degradation to our signal-to-noise ratio. Considering the probability to emit a pair of photons from a PDC crystal is then:

$$P_{\text{pair}}(n) = (1 - \lambda P)(\lambda P)^n, \tag{2.5}$$

with n the number of pairs emitted. From this we can then define our signal-to-noise ratio as:

$$\text{SNR} = \frac{P_{\text{pair}}(1)}{\sum_{n=2}^{\infty} P_{\text{pair}}(n)} = \frac{1}{\lambda P} - 1. \tag{2.6}$$

Then defining our signal-to-noise ratio from the detected rate, R, for pairs and signal and idler modes separately as: For more practical situations, like when rates are being detected and measured from a PDC source eq. (2.6) can be considered to be of the form:

11

$$\text{SNR} = \frac{P_{\text{Coincidence}}}{\sqrt{P_{\text{Signal}} \times P_{\text{Idler}}}}. \tag{2.7}$$

With eq. (2.6) it becomes clear that λ plays a key role in determining the signal-to-noise performance of PDC sources; as this parameter increases so does the probability and with it emission (detection) rates for higher-order events. We can then also consider the brightness of the source typically defined as the emitted (detected) rate of photon pairs per milliwatt of pump power, under this definition we see that we must also find a method to increase the γ term of λ to create an intrinsically brighter source however that in doing so we also increase the probability of emitted more than a single pair of photons in turn reducing the signal-to-noise ratio.

2.1.2 Spectral Purity of PDC States

Above, we discussed the PDC state in the photon-number basis. Equally important for the quality of a photon source are its spectral properties, so we will now turn to a description of the PDC state in the frequency domain for a single pair of photons in the Fock space:

$$|\psi_{\text{PDC}}\rangle_{i,s} = \iint d\omega_i d\omega_s f\left(\omega_i, \omega_s\right) a^\dagger b^\dagger |0\rangle_i |0\rangle_s. \tag{2.8}$$

Here $f\left(\omega_i, \omega_s\right)$ defines the joint spectral amplitude (JSA), which determines the spectral purity of a photon heralded from a PDC photon pair. Through the JSA we can observe the spectral correlations in the photon pairs arising through conservation of energy and momentum in the PDC process. Through application of filters we can reduce the joint spectra to contain only the desired correlations. Group-velocity matching (GVM) provides a different method to achieve this, by finding the conditions under which the desired pump and PDC wavelength phase-match in crystals that allow the inverse group velocity of the pump to match either one of or the average of both the PDC photons inverse group velocities as experimentally demonstrated by Mosley *et-al.* [66]. There exists two possible cases for GVM: symmetric and asymmetric. In symmetric GVM, the group velocity of the pump lies exactly halfway between the group velocities of the signal and idler photons, whereas in asymmetric GVM either one of the signal or idler photons is matched to

the pump photons group velocity. In doing so the timing information between the pump and PDC photons can be erased which in turn provides a JSA with greater separability and so a higher spectral purity. The JSA, represented by f, is defined as following product of two other functions:

$$f(\omega_i, \omega_s) = \alpha(\omega_i, \omega_s)\phi(\omega_i, \omega_s).\tag{2.9}$$

These two functions are the pump envelope function, $\alpha(\omega_i, \omega_s)$, and the phase-matching function (PMF), $\phi(\omega_i, \omega_s)$. The pump envelope function described for pump pulses with a sech shape, normally it is taken to be Gaussian, we however work in the case of mode-locking leading to the sech shape:

$$\alpha(\omega_i, \omega_s) = \int_\infty^\infty dt\,\mathrm{sech}\left(\frac{t}{\tau_p}\right)e^{i\Delta\omega t} = \sqrt{\frac{\pi}{2}}\tau_p\mathrm{sech}\left((\omega_c - \omega_i - \omega_s)\frac{\pi\tau_p}{2}\right).\tag{2.10}$$

The parameter τ_p is dependent on the FWHM of the pump pulse whilst ω_c denotes the central frequency between the signal and idler modes. The phase-matching function depends on the nonlinearity of the PDC medium and the phase mismatch, defined as:

$$\phi(\omega_i, \omega s) = \int_\infty^\infty dz\, g(z)e^{i\Delta k(\omega_i,\omega_s)z},\tag{2.11}$$

where $\Delta k(\omega_i, \omega_s)$ provides the phase mismatch (i.e. the inefficiency in the PDC process brought about by material dispersion), $g(z) = \chi^{(2)}(z)/\chi^{(0)}$ provides the nonlinear interaction. For ppKTP crystals the following structure for the PMF follows:

$$\phi(\omega_i, \omega s) = \mathrm{sinc}\left(\left(\Delta k(\omega_i, \omega s) - \frac{2\pi}{\Lambda}\right)\frac{L}{2}\right)\tag{2.12}$$

The poling period present in the crystal is expressed by the Λ parameter whilst L is the length of the crystal. We can infer from eq. (2.12) that phase-matching is maximal when $\Delta k(\omega_i, \omega_s) - \frac{2\pi}{\Lambda} = 0$. The sinc nature arises from the transition experienced by the pump photons from travelling through an environment with no nonlinearity to nonlinearity then being present, and back again. This instantaneous

switching on and off of the nonlinearity results in rectangular nonlinearity profile the Fourier transform of which is the sinc function present in eq. (2.12).
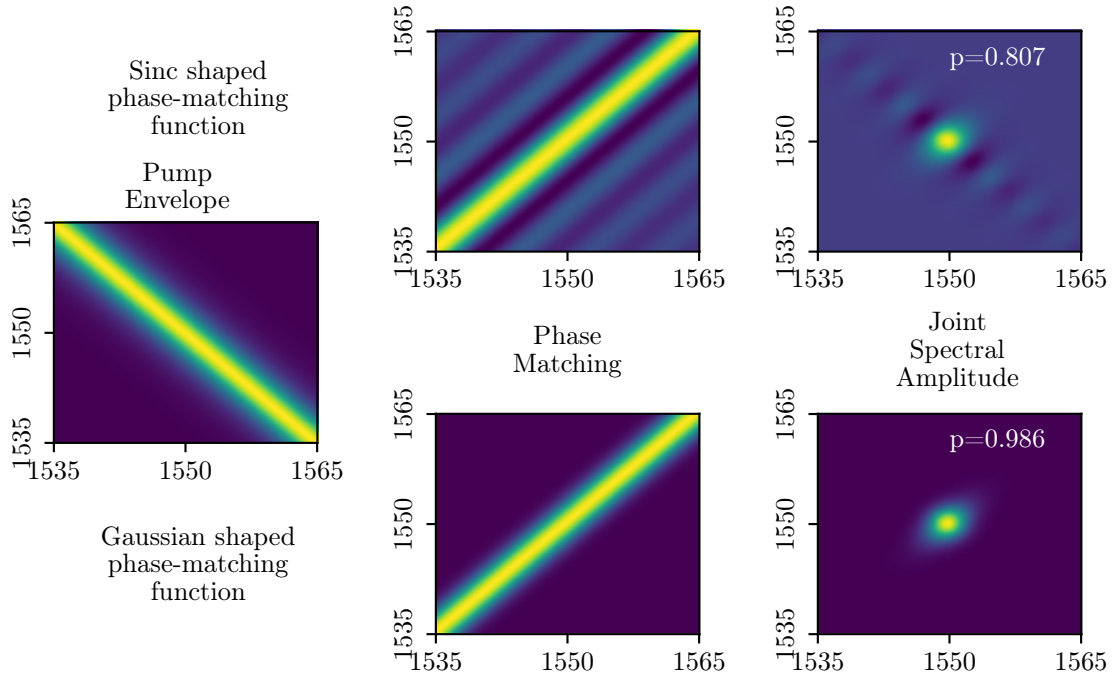
Figure 2.3: **Tailoring the phase-matching function allows for producing higher spectral purity heralded photons.** The upper and lower panels in the centre of the figure show the difference between a sinc shaped and Gaussian shaped phase-matching function respectively. We can clearly see the oscillations in the sinc function extending across the diagonal, whereas for the Gaussian we have only the central phase-matching. For the same pump envelope function we find that the resulting joint spectra in each case markedly different. The sinc oscillations persist into the joint spectra whereas for the Gaussian we are left with a single central lobe. In performing the purity calculation on each of these joint spectra we find a significant improvement in spectral purity in using a Gaussian PMF of $\approx 22\%$ over that calculated for a sinc PMF. The phase-matching functions here operate in a symmetric GVM scheme where the pump wavelength is at 775nm and both the signal and idler have a target of 1550nm.

The phase-matching function provides a method to increase the spectral purity of our PDC state, periodically poled crystals are subject to the shape of the sinc function and so their JSA contain a series of side lobes extended away from the centre, these side lobes have the effect of reducing the overall spectral purity. By tailoring the PMF, and so shaping the JSA, it becomes possible to design PDC crystals with inherently higher spectral purities without having to filter the emitted photons in order to remove the side lobes.This tailoring process is achievable by manipulating the crystal domain orientation along the longitudinal axis of the PDC

crystal combined with specifying the length of each respective crystal domain. The nonlinearity profile defined by the order of crystal domain orientations and lengths can be related to the joint spectra of the PDC photons by means of a fourier transform. A full consideration of the process required to tailor the nonlinearity profile along the longitudinal axis has been refined by our group [67, 68]. The experimental validation of a pair of different crystal designs have been completed, the first designed to emit higher purity PDC photons [6], and the second designed to emit photons with time-frequency mode entanglement [7].

Calculation of spectral purity from the JSA is achieved by means of Schmidt decomposition, returning a number of Schmidt magnitudes across the frequency space of the spectra. The Schmidt decomposition of the form:

$$f(x, y) = \sum_k \kappa_k g(x) h(y), \tag{2.13}$$

allows for the joint spectra of the PDC photons eq. (2.9) to be decomposed into a range of positive values, κ_k and a pair of complete orthonormal functions $g_k(x)$ and $h_k(x)$ that correspond to the signal and idler frequencies respectively. The decomposition process operates on the JSA as a continuous function over the parameters ω_s and ω_i, however analytical solutions are not necessarily convenient and so we instead translate the JSA to a discrete matrix comprised of a pair of orthogonal matrices for the signal and idler modes along with a diagonal matrix composed of the Schmidt magnitudes, κ_k. By taking the reciprocal of the Schmidt number:

$$K = \sum_k \frac{1}{|\kappa_k^2|} \tag{2.14}$$

we can extract the spectral purity from the JSA found in the two-photon PDC state eq. (2.7), allowing us to determine how indistinguishable the heralded photons are with a spectral purity of 1 being the maximum. Similarly, singular value decomposition can be applied to measurements of joint spectra as this produces an estimate of the Schmidt coefficients allowing for estimations of spectral purity to be made. This is explored further in chapter 6 where the joint spectral intensity of a range of PDC crystals is reconstructed.

2.2   Detectors
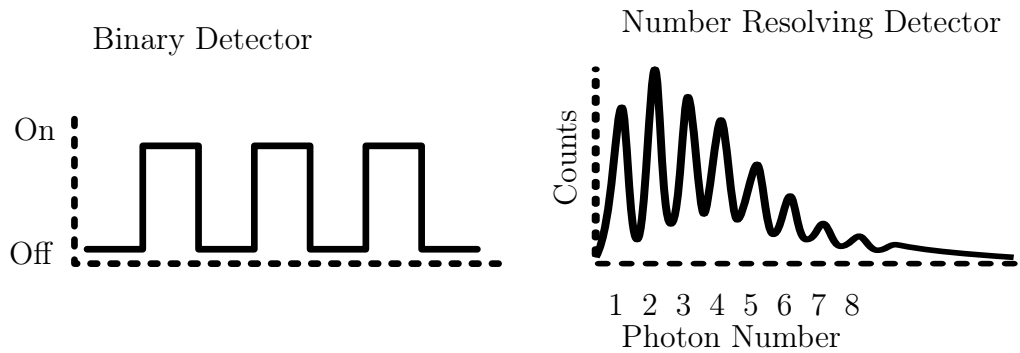
Figure 2.4: **Outputs of binary and photon number resolving detectors.** Binary detectors are only able to out put a signal showing if they are on or off resulting in all detection events in having a $|n > 1\rangle$ state. In contrast the photon number resolving detector allows us to distinguish between each $|n\rangle$ state within the limit it can resolve providing a distribution for each state reaching the detector.

Once it comes to detection of our quantum light we have a further number of decisions to make dependent on the type of detection that we want as well as what type of detector suits the application best. Detectors fall into one of two basic classifications; "binary" detectors in which the detector is either on or off (on when one or more photons arrive at it) and photon-number-resolving (PNR) detectors where the number of photons arriving at the detector can be observed instead of just whether or not a signal arrived. Further, the detection method then has its own types, photo multiplier tubes (PMT), micro channel plates (MCP), avalanche photo diodes (APD) and superconducting detectors. Each of these detection technologies have their own unique behaviours however they can all be benchmarked by a set of common descriptors such as, detection efficiency, dark count rate, detector jitter and detector reset time (or dead time). Each of these characteristics provide their own limiting factors and whilst one detector may be best in one it may not be suitable for certain applications, for example whilst PNR detectors give information into the photon number they are slow to reset and so might not be suitable choices for the like of quantum key distribution (QKD).

PMTs, one of the oldest technology for single photon detection, wherein a photon enters the tube hits the photocathode to release a primary electron which then proceeds to hit the first dynode producing the first release of secondary electrons

which in turn hit the next dynode and so on until all of the secondary electrons reach the anode to produce a detection signal. MCP operate under much the same principle, but also gain the spatial resolution given the fact that each channel behaves as its own PMT, optionally also containing a fluorescent screen as well as a CCD array.

From these older technologies we arrive at the current "standard", the avalanche photo diode (onwards referred to as a single photon avalanche photo diode (SPAD)), once a photon is absorbed it creates an electron-hole pair in the semiconductor (InGaAs/InP) detector causing an avalanche current (self sustaining) to produce an output pulse we can then process. APD's have seen successive improvements since first realised, initially implemented in silicon they have since been implemented on the CMOS process allowing for the realisation of SPAD arrays, comprising of a grid SPAD detectors with lower jitter, dark count rates and shorter dead times [69].
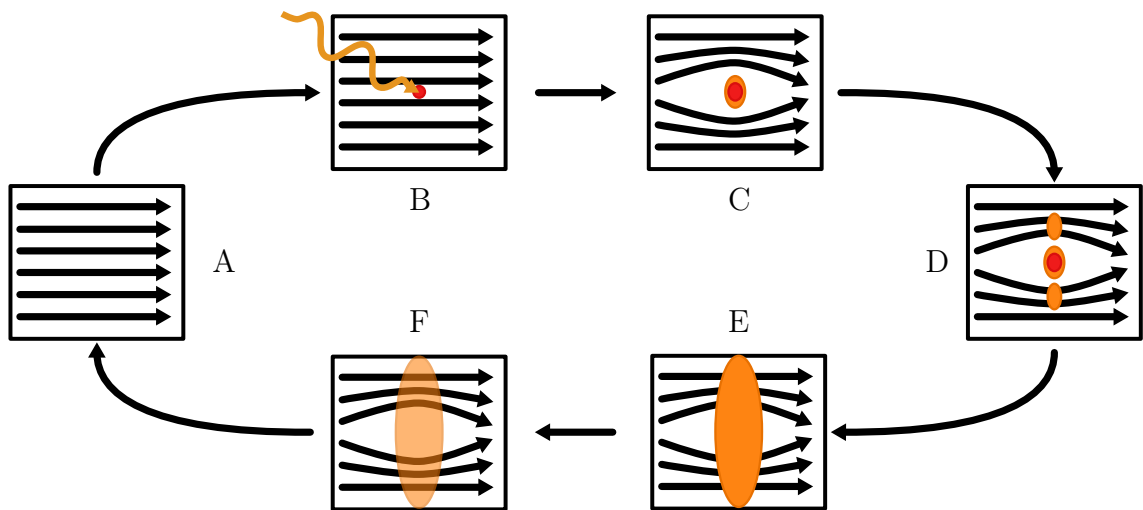
Figure 2.5: **Operating principle of superconducting nanowire single-photon detector.** (A) The nanowire is in the superconducting state well below the critical temperature and is biased slightly below the critical current. (B) Once the nanowire absorbs a single-photon a resistive hotspot is formed. (C) The current density surrounding the hotspot begins to increase. (D) Resistive barriers form on both sides of the hotspot. (E) This results in joule heating, increasing the size of the resistive region across the nanowire until the current flow is blocked, the bias current can then be readout by the amplifiers. (F) The resistive region now reduces and the nanowire can enter the superconducting state again.

Beyond these technologies are those of superconducting detectors which promise detection efficiencies in excess of 80% along with low jitter and even shorter dead

times and finally the possibility of photon-number resolution. Within the realms of superconducting detectors there exists two key technologies, transition edge sensors (TES) and superconducting nanowire single-photon detectors (SNSPD), functioning as PNR and bucket detectors respectively. TES based photon detectors employ a thin film of superconducting material ($\approx$20nm thick) weakly thermally coupled to a bath of coolant (for example liquid helium), by placing a bias current over the film resulting in an electrical resistance holding the material in the centre of its transition region. As a result when a photon is incident on the surface of the film, a small amount of localised heating is caused leading to a raising in resistance causing a drop in the current along with a drop in the joule power cooling the device back down, this process pushes the material past its transition edge to a traditional conductor and then cools it back down into its transition region. By means of inductive coupling between the superconducting film and a superconducting quantum interference device (SQUID) it is possible to provide a readout for this process as changes in the current over the film will result in changes in the flux across the SQUID. This process provides the TES's greatest feature but is also the reason they are known for long reset times of the order of microseconds, as the photon number incident on the film increases so does the time taken to return to the transition region due to the amount of heating caused [70].

Similarly nanowire based detectors (SNSPD) operate under a thermal process, in this case the impact of a photon on the nanowire causes the break down the superconducting phase leading to a localised temperature increase (creating a hotspot). Due to the bias current being set to a point lower than that of the critical superconducting current the creation of a hotspot produces an increase in resistance across the nanowire greater than 50 Ω (typical readout resistance). Subsequently this provides a shunt current towards the readout electronics amplifier resulting in an output detector pulse, in turn this process also provides a mechanism for the nanowire to return back to its superconducting temperature ready for detection again. Much like for APDs, arrays of SNSPDs can be constructed, providing further applications for imaging as well as to provide some degree of photon-number resolution [37] (by using a parallel readout, if multiple detectors are triggered at once, the output pulse can be summed to give determination into the number of photons that arrived).

All examples of these competing technologies can be evaluated through the same set of features, those of; detection efficiency, jitter, reset time and dark count rate. In an ideal detector we would have 100% detection efficiency, zero jitter, infinitely short reset time and no dark counts.

Detector type	Detection efficiency, wavelength $\eta(\%)$, $\lambda(nm)$	Timing jitter, $\delta t(ns)(FWHM)$	Dark-count rate, D (ungated) (1/s)	Max. count rate $(10^6/s)$	Citations
PMT (visible-near-infra-red)	40 @ 500	0.3	100	10	[71]
PMT (infra-red)	2 @ 1550	0.3	200 000	10	[72]
Si SPAD (thick junction)	65 @ 650	0.4	25	10	[73]
Si SPAD (shallow junction)	49 @ 550	0.035	25	10	[74]
Si SPAD (self-differencing)	74 @ 600	...	2000	16	[75]
Si SPAD (linear mode)	56 @ 450	...	0.0008	0.01	[76]
Si SPAD (cavity)	42 @ 780	0.035	3500	10	[77]
Si SPAD (multipixel)	40 @ 532	0.3	25000 - 500000	30	[78]
Hybrid PMT (PMT + APD)	30 @ 1064	0.2	30 000	200	[79]
Time multiplexed (Si SPAD)	39 @ 680	0.4	200	0.5	[80]
Time multiplexed (Si SPAD)	50 @ 825	0.5	150	2	[81]
Space multiplexed (InGaAs SPAD)	33 @ 1060	0.133	160 000 000	10	[82]
Space multiplexed (InGaAs SPAD)	2 @ 1550	...	...	0.3	[83]
InGaAs SPAD (gated)	10 @ 1550	0.37	91	0.01	[84]
InGaAs SPAD (self-differencing)	10 @ 1550	0.055	16 000	100	[85]
InGaAs SPAD (self-differencing)	10 @ 1550	...	...	...	[86]
InGaAs SPAD (discharge pulse counting)	7 @ 1550	...	40 000	10	[87]
InP NFAD (monolithic negative feedback)	6 @ 1550	0.4	28 000	10	[88]
InGaAs (self-quenching and self-recovery)	... @ 1550	10	...	3	[89]
CIPD (InGaAs)	80 @ 1310	...	...	0.001	[90]
Frequency up-conversion	8.8 @ 1550	0.4	13000	10	[91]
Frequency up-conversion	56-59@ 1550	...	460000	5	[92, 93]
Frequency up-conversion	20 @ 1306	0.62	2200	10	[94]
VLPC	88 @ 694	40	20000	10	[95]
VLPC	40 @ 633	0.24	25000	10	[96]
SSPM	76 @ 702	3.5	7000	30	[97]
TES (W)	50 @ 1550	100	3	0.1	[98]
TES (W)	95 @ 1556	100	...	0.1	[99]
TES (Ha)	85 @ 850	100	...	0.1	[100]
TES (Ti)	81-98 @ 850	100	...	1	[101, 102]
SNSPD	0.7 @ 1550	0.06	10	100	[103]
SNSPD (in cavity)	57 @ 1550	0.03	...	1000	[104]
Parallel SNSPD	2 @ 1300	0.05	0.15	1000	[105]
STJ	45 @ 350	2000	...	0.01	[106–108]
QD (resonant tunnel diode)	12 @ 550	150	0.002	0.25	[109]
QDOGFET (field-effect transistor)	2 @ 805	10000	150	0.05	[110–112]

Table 2.1: **Comparison of various single-photon detector technologies.** Single-photon detectors can be designed for use at a wide range of different wavelengths. Each of these technologies have their respective performance advantages and disadvantages. Ideally, for our desired operating wavelength, we want a detector with a dark count rate of zero, i.e. there are now accidental detection events that arise from the construction of the detector. Next we want unit efficiency such that we can detect as much of the signal that we produce as possible. In combination with detection efficiency we also need our detectors to have as short a possible reset time ($\approx \frac{1}{\text{Max. Count rate}}$) in order to avoid "dropping" photons as the detector isn't ready to detect them. And finally to maintain the precision of our measurements we need detectors with a small timing jitter. (Reconstructed from [113])

Finally after being able to detect the light that we have produced and manipulated we require a means to process the results.

2.3   Timing Logic

With our states generated and results detected it is now time to process the signals from the detectors. When it comes to the signal processing we are usually interested in a few pieces of information, the first being the time of when the photon arrived at the detector (either absolute or relative timing), the photon flux at each detector and then correlations between detector channels. Such correlations, the coincidences between channels, may not have arrived at the detectors simultaneously we can apply electronic delays to the signals or afterwards as a post processing action to account for any effects due to path lengths between the manipulation of quantum light and its detection.

Timing information can be carried out with the likes of a time-tagging device or a time-difference analyser (TDA), should we want to be looking at the detector signal between channels or against some reference clock signal. In both cases we can investigate the photon arrival times with both (either) absolute or relative timing, absolute timing being in relation to a clock signal (employed as part of the experiment) and relative timing being just the delays present between each channel. For example, if we were to investigate the biphoton spectra of an SPDC source we would require both relative and absolute timings, first we would use relative timings to find the delays between the channels connected to the SPDC source followed by finding the absolute timing between those channels and our reference clock such that we can then reconstruct the spectra (we will go into further detail on this topic in chapter 6). In the case of the TDA it is possible to find the correlations between detector channels as bins of a histogram and when using time tagging we can expand on this further, as in we become able to easily access the value for the flux at a given detector as well as the timing information for each photon arriving along with any and all of the combinations of coincident detection events. Further for time tagging it becomes possible to collect a stream of time tags in a buffer on a host computer for further processing, i.e. if we wanted to perform an experiment in which we needed a pair of SPDC sources but only had one we could use this to look for coincidence events that repeat in time along the buffer, providing us with further inspection. More commonly however, a stream of time tags can be written to a hard drive for storage of an experiments result for later post processing.

Timing devices like these can naively be considered to behave like stop watches with up to picosecond resolutions, this however is an oversimplification as to achieve resolutions like this the timing afforded by the likes of a quartz crystal is not nearly enough. Achievement of such high resolution timing requires more advanced electronics like a bit rate analogue to digital converters (ADC). One such method for measuring arrival time to this degree is that of the constant fractional discriminator (CFD), here a voltage is stepped from 0V to a maximum where each step corresponds to an increase of 1-bit in a register, once an incoming signal arrives at this voltage ramp the crossing of the signal will cause the value of the register to be read out, if we then assign each increase in this register to each tick of the devices internal clock we can output a value for when the detector pulse arrived at our timing electronics and so know when the photon arrived at the detector.

Alternatively it is possible to construct a series of "delay taps" to determine the arrival time of each photon, this is a frequently employed method on timing devices relying solely on what can be employed on an FPGA (whereas that of the CFD may also need an amount of dedicated digital electronics to also be employed)

Methods like these allow for the implementation of time correlated single photon counting (TCSPC), where we have both pieces of information, how many photons have been produced and at what time was each produced. Further this is a technique that has been extended to detector arrays allowing for time correlated imaging useful for techniques such as single photon microscopy. Due the flexibility of TCSPC it has become a staple technology across the field, providing a powerful tool to analyse our experiments with and provide a method to drive the actions necessary for active feed forward.

Chapter 3

Numerical Modelling of
Multi-Photon Experiments

3.1 Introduction

In most photonic quantum information experiments the primary source of errors
are higher-order photon emissions (i.e. events where more than one photon pair was
created simultaneously) in (PDC) sources [114].

When considering the expansion of eq. (2.3) in which the power of the pre-factor,
λ, increases with increasing photon number, a clear trade-off can be observed be-
tween having a high probability to create pairs of photons resulting in a reduction
of integration time and at the same time the option to minimise noise. Multiplexing
of PDC provides a means to facilitate this, either spatially, temporally, or both, and
may be of benefit given our motivation to build state-of-the-art entangled multipho-
ton experiments at telecom wavelengths. Application of multiplexing to the pump
pulse to increase clock rate is already known to suppress noise and as a result the
question then naturally arises for us as to what the optimal clock rate would be
given our constraints on pump power and detector reset times.

We then need to be able to accurately model both single PDC sources as well as
their use within multiplexing schemes that have the capability to increase the proba-
bility to herald a single photon. In the case of spatial multiplexing we would need to
consider a device consisting of several heralded single-photon sources using the first
heralding signal from any of the constituent sources to route the resulting single-

photon through a many-to-one switch yard into a common shared output mode [115]. From [64] it is shown that 17 PDC sources with photon-number-resolving detectors and an active switch yard is required to achieve a deterministic "on-demand" source of single photons and that these high requirements are needed in order to combat the effects of higher-order emissions. Further, passive temporal multiplexing [116, 117] schemes wherein the pulses of a pump source are interleaved are capable of suppressing higher-order emissions [118, 119] due to reduction of pump power while maintaining (or exceeding) observed count rates compared to schemes without multiplexing. In the expansion of eq. (2.3), in which we see this increase in the exponent associated with λ, the relation to power (more specifically the amplitude of the electric field), by interleaving the pump through splitting it in half and then recombining after offsetting one path we see that the pulse power must be halved and the repetition rate must be doubled for each split accordingly. This results in a reduction of $\frac{1}{2}$ for the $|11\rangle$ term (single pair emission), $\frac{1}{4}$ for the $|22\rangle$ term (double pair emission) and so on, the doubling of the repetition rate compensates for single pair emission whilst still providing a reduction in double pair and higher emissions. We should take care here to note that since photons follow Poissonian statistics that the probability for higher-order emission and that of single-pair emission from multiple sources are the same, i.e $p(1)^N \equiv p(N)$ where N is the number of sources or pairs respectively, meaning that whilst we can increase the number of pairs from a single source the probability of generating multiple pairs with one from each source is harder to increase. We can then consider this a method to increase the signal-to-noise ratio of a single source with respect to photon number.

Alternatively, active temporal switching with a delay line can be used to generate a predictable pulse train of single photons [120–122]. However, neither of these approaches is designed to improve the rate of multi-photon events explicitly, instead they aim to construct a deterministic single-photon source which can then be used for producing high multi-photon rates. Experimentally these schemes require a trade off between pump power as well as clock rate (laser repetition rate), increasing the pump power of an experiment (with PDC sources) allows for higher count rates however increases both the pair emission rate as well as the higher-order emission rate, the result of this is a reduction in the signal-to-noise ratio. Alternatively, increasing the

clock rate increases count rates however detector saturation will occur sooner.

Further, in an experimental setting this requires making considerations for detection efficiency (η) and detector reset/dead times (τ)[1], along with clock rate and pump power. Each of these considerations acts as limiting cases in their own way, with η providing us with an upper bound on count rates and τ limits the maximum clock rate we can benefit from [123–125]. Given these factors and a want to generate ever larger multi-photon states we are left with a need to balance these factors in order to know how fast an experiment can be run in order to achieve the desired result within a "reasonable time" frame. The result of the need to balance these factors including the effects arising from multiplexing leads us to the two models we present here. Further the presented models have been used to inform decisions made when constructing and refining our quantum photonics platform such as our decision increase the repetition rate of our pump source at the expense of power for a better signal-to-noise ratio without too great a loss total emission rates.

3.2 Single-Photon Emission and Detection Models

Here we present a pair of models for the emission and detection of single-photons emitted from single or multiple sources designed to include the effects of different source nonlinearities, loss [126] as well as reset/dead times of potential switches, the detectors and the timing logic such that we can tune them them to optimise system performance. Previous models [127–129] have employed matrix exponentiation to analyse photon generation, transmission and detection and omit the effects of detector reset times. The first of our methods makes use of combinatorics allowing for us to model the probability that a detector is ready based on experiment clock speed and reset time. We present a framework to apply these effects to any system. Secondly we present a Monte-Carlo sampling based method to simulate the individual emission events, this encompasses the features of the combinatorial model while allowing us to add specific behaviours relating to the manipulation of time bins and mixing of modes present in multiplexing schemes. This however all comes at the expense of computational overhead due to the volume of samples

---

[1] The parameter τ related here to detector reset/dead times is different to the source parameter in section 2.1.1.

needed when compared to the combinatorial method. The models defined here are validated against experimental data and values for the free parameters associated with λ and detection efficiency are determined.

3.2.1 Combinatorial Model

In contrast to previous models developed for photon generation and detection [127–129], we use a combinatorial approach that does not require matrix exponentiation. This approach requires calculating the emission probability for each photon number n, see eq. (2.3) so as to cover all possible emissions from the source. The usual approach would be to truncate the Fock space to some very limited n. Here we instead use mathematical toolkits that calculate infinite sums by means of convergence.[2] Under this description all major design constraints of single-photon experiments can be taken into account: the probabilistic nature of photon emission[3], losses, imperfect detection efficiency, and the finite speed of current photon detectors. The model consists of three distinct stages: generation, manipulation, and detection. In the following we will not include state evolution, as it does not significantly affect the trade-offs we are interested in.

Quantum light, i.e. Fock states, exhibits a sub-Poissonian photon number distribution whereas single-mode thermal radiation is described by a super-Poissonian distribution. Further, thermal light sources emit a multi-mode field and as a result can be described as the convolution of the number distributions for several thermal fields. The ability for PDC sources to emit more than a single pair at a time represents a system with multi-mode output constructed from an infinite number single-mode distributions, from this we can turn to the Poissonian distribution as a basis for our model [130]. The distribution, characterized by the pump power P and the nonlinearity of the source, described by the parameter γ as well as the number of photon pairs n.

---

[2] It should be noted that this model relies the on binomial coefficient and as a result makes heavy use of the factorial function which places a limit of 20! as the largest calculable value under the 64-bit limit. We choose to make use of arbitrary precision numbers to remove this limitation at the cost of computational expense. Numbers under the 64-bit limit provide for faster execution of the model, which may be of use for estimations at the cost of truncation.

[3]Note that this includes "on-demand" sources, since inevitable losses turn also these into probabilistic sources, albeit with probability on the order of currently 0.1.

$$p_{\text{em}}(P, n, \gamma) = \frac{(\gamma P)^n e^{-\gamma P}}{n!} \tag{3.1}$$

To obtain the probability for a detector to click, p_{det}, we have to take into account all cases where at least k out of n single-photons in a single mode are absorbed by the detector. In general this probability is given by

$$p_{\text{det}}(\eta, n, k) = 1 - \sum_{i=0}^{k-1} \binom{n}{k} \eta^i (1 - \eta)^{n-i} , \tag{3.2}$$

where $\binom{n}{k}$ is the Binomial coefficient for choosing k out of n, and η is the detection efficiency for a given mode.

The final probability required for making predictions about count rates is the probability that a pair of detectors connected to the same source are ready for detection, in the sense that they are not currently recovering from a recent detection. This is obtained from the probability of a photon having been present within the time t (in seconds) that the detector takes to reset, prior to the current time slot, and the probability of that photon not having been absorbed.

$$p_{\text{ready}}(P, R, t, \gamma, \eta_1, \eta_2) = \tag{3.3}$$

$$\left(\sum_{j=0}^{\infty} p_{\text{em}}(P, j, \gamma) p_{\text{det}}(1 - \eta_1, j, j) p_{\text{det}}(1 - \eta_2, j, j) \right)^{\lfloor R \times t \rfloor} .$$

Here, R is the repetition rate of the laser in Hz, and $\lfloor x \rfloor$ denotes the floor function, rounding x to the nearest integer less or equal to x. η_1 and η_2 are the detection efficiencies for the two modes involved. With this the effects of reset (dead) times can be included in the model, given that we are considering a model operating in the pulsed regime (as opposed to continuous wave, c.w.) we can consider the reset times of components as providing a number of pulses where they are unable to function. The floor function used here seeks to quantise the reset time to the number of time bins it occupies (where one pulse is one time bin). Note that this expression also captures the case of a single-photon source, rather than a pair source, by simply setting $\eta_2 = 0$.

Equipped with these basic functions, we can now compute the detected count rates for single emission events, as well as multiple emission events for any number of independent sources. In particular, this lets us calculate the signal-to-noise ratio due to higher-order emissions. We now explicitly illustrate the use of our model to describe the case of producing $2N$-photon states using N independent photon-pair sources. The first of these is the single channel detection rate of a PDC source, defined as:

$$R_s(P, R, t, \gamma, \eta) = \tag{3.4}$$

$$R\left(\left[\sum_{j=1}^{\infty} p_{\text{em}}(P, j, \gamma) p_{\text{det}}(\eta, j, 1)\right] p_{\text{ready}}(P, R, t, \gamma, \eta, 0)\right),$$

Detailed in eq. (3.4) we define single emission rates as the infinite sum over all photon numbers requiring that only one detector is ready, conversely for the detection rate of multi-photon events (assuming only a pair of photons is produced from each source) we require only the product of pair emission from each source and the corresponding number of detectors to be ready. Defining this case as:

$$R_{cc}(P, R, t, \gamma, \eta_1, \eta_2, N) =$$

$$R \cdot \prod_{i=1}^{N} \left(p_{\text{em}}(P, 1, \gamma_i) p_{\text{det}}(\eta_{1,i}, 1, 1) p_{\text{det}}(\eta_{2,i}, 1, 1) \right.$$

$$\left. p_{\text{ready}}(P, R, t, \gamma_i, \eta_{1,i}, \eta_{2,i}) \right). \tag{3.5}$$

Finally, for the detected rate with the inclusion of higher-order emissions eq. (3.6) we combine eq. (3.4) and eq. (3.5) as we need the contribution from photon numbers > 1.

$$R_{cc+}(P, R, t, \gamma, \eta_1, \eta_2, N) =$$

$$R \cdot \prod_{i=1}^{N} \Bigg(\sum_{j=1}^{\infty} \Big(p_{\text{em}}(P, j, \gamma_i) p_{\text{det}}(\eta_{1,i}, j, 1)$$

$$p_{\text{det}}(\eta_{2,i}, j, 1) \big) p_{\text{ready}}(P, R, t, \gamma_i, \eta_{1,i}, \eta_{2,i}) \Bigg). \qquad (3.6)$$

For the exploration of experimental schemes other than a number of sources connected directly to detectors the functions defined here can be extended to encompass effects from the likes of optical switches, as they also have a probability of them being ready (i.e. in the correct state) and some success probability behaving in the same manner as the detectors.

3.2.2 Monte-Carlo Model

The second model we present here takes a completely different approach for applying loss, timing effects and the calculation of detection rates. Instead of calculating individual probabilities for all parameters affecting each order of emission we instead make use of a statistical distribution to determine PDC source emission. The emission is subject to random sampling of a statistical distribution. As a result we describe either a process that creates photons or one that removes photons. This allows us to generate a sample as a single pulse from our pump source and manipulate the population of photons in each spatial mode to observe the effects of loss and relative timings of components. Further, this also provides a way to simulate optical circuits (i.e. networks of beamsplitters) as we have a method to manipulate (re-order and mix) both modes and time bins providing insight into the resulting coincidence rates seen at the detectors.

The probability for a sample to contain photons produced from any given source is governed by a geometric distribution. Whilst a Poissonian distribution was required for the combinatorial model the choice to use geometric distribution here is born from defining each sample as being either successful or unsuccessful in producing photons. We can consider each single-photon source to behave in this way

as photons are either produced or not. Much like in the combinatorial model we use the γ parameter as well as the power P to define the success probability to generate a pair[4] of photons, i.e. the success probability of the distribution. Much like the generation of photons in this model, the effects of loss are also subject to a statistical distribution, in this case we incorporate loss into the model by defining a series of weights,

$$\left[\binom{m}{k} \eta^i (1-\eta)^{m-i} \text{for } \{k : (0 \to m+1)\} \right], \tag{3.7}$$

where each weight corresponds to the probability for a given value of m (where m is the number of possibilities for a given process). We can then use this as the basis for determining whether or not a photon, or how many photons of a given mode, are detected. To do so we require a list of of photon numbers ranging from 0 to the total number in that mode, calculating the weights for the detection efficiency η and proceeding to randomly choose a value for the photon number list according to the detection weights. Further, we can apply the same method for determining the distribution of photons after one mode arrives at a beamsplitter, in this case the options are constructed as $(k, m-k)$ for $\{k : (0 \to m+1)\}$, meaning that we can have any combination of photon numbers produced from the value in the impinging mode in the two output modes.

With generation and loss of photons from probabilistic means now covered we must now consider the final effect, that brought about by timing. Just like in the combinatorial model, we must also quantise the length of the reset time of our components to that of the clock rate of the pump source. Here however we quantise with a ceiling function resulting in any photon arriving at the detector whilst it resets being lost. Ideally, this should be considered with a further sampling of a statistical distribution because certain detectors, such as SNSPD's, allow for detection whilst still resetting, albeit at lowered efficiency, however to consider a more general case we forgo this feature.

In summary, to apply this model, we first generate an array of all our pulses for each mode, then apply our optical scheme with any lossy elements present, next

---

[4]With this condition both output modes of an SPDC source must contain the same value for the number of photons emitted, application of loss later in the model then provides cases where we may have only one photon emitted from the source to be detected at the detector.

applying lossy detection, these processes are all completed assuming no timing effects like those of reset times. After this we then apply timing effects by analysing the arrays by counting the first event in each array as a valid event and then jumping forward in the array by the quantised reset time (if there is no event we move only to the next index in the array and see if that contains a valid event and so on).
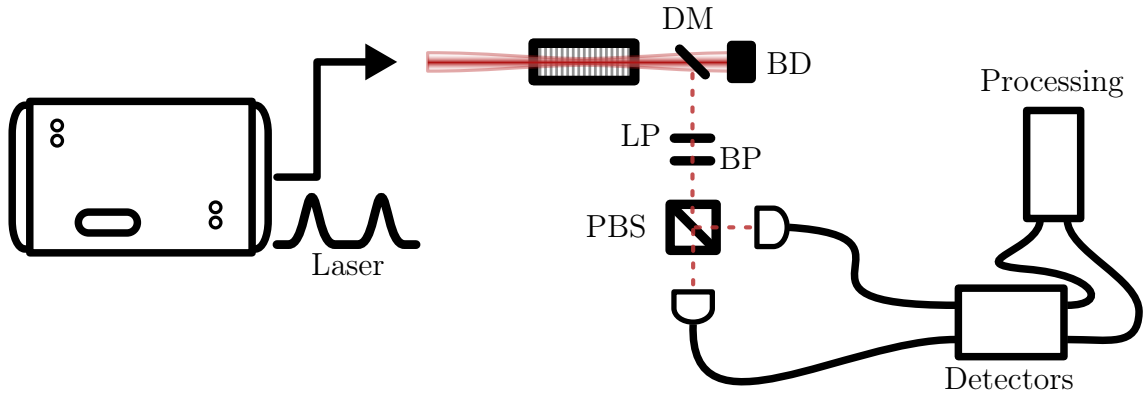
3.3   Model Validation With Experimental Data

Figure 3.1: **Experimental configuration used to validate models** A pulsed Ti:Sapphire laser with 80 MHz repetition rate, 1.3 ps sech^2 pulses at 775 nm is focused into a KTP crystal to create 1550 nm photon pairs via collinear, type-II PDC. The orthogonally-polarised down-converted photons are filtered from the pump with a dichroic mirror (DM), a long-pass (LP) and a loose band-pass (BP) filter (with a bandwidth ≈ 3 times larger than the PDC photons' bandwidth). Signal and idler photons are collected after the PBS to send to the detectors (Quantum Opus SNSPDs) before processing with a UQDevices Logic-16.

Having now defined two models for the behaviour of a generic quantum photonics experiment driven by a number of photon sources we must first validate it. In order to do this we have chosen to first find a value for γ (our effective nonlinearity) and second the system detection efficiency, η. We know the repetition rate of our pump laser is at 80.9MHz and we have chosen to use the quoted detector efficiency of 80% (the value supplied by the manufacturer, Quantum Opus) as a starting point for the model to find η.
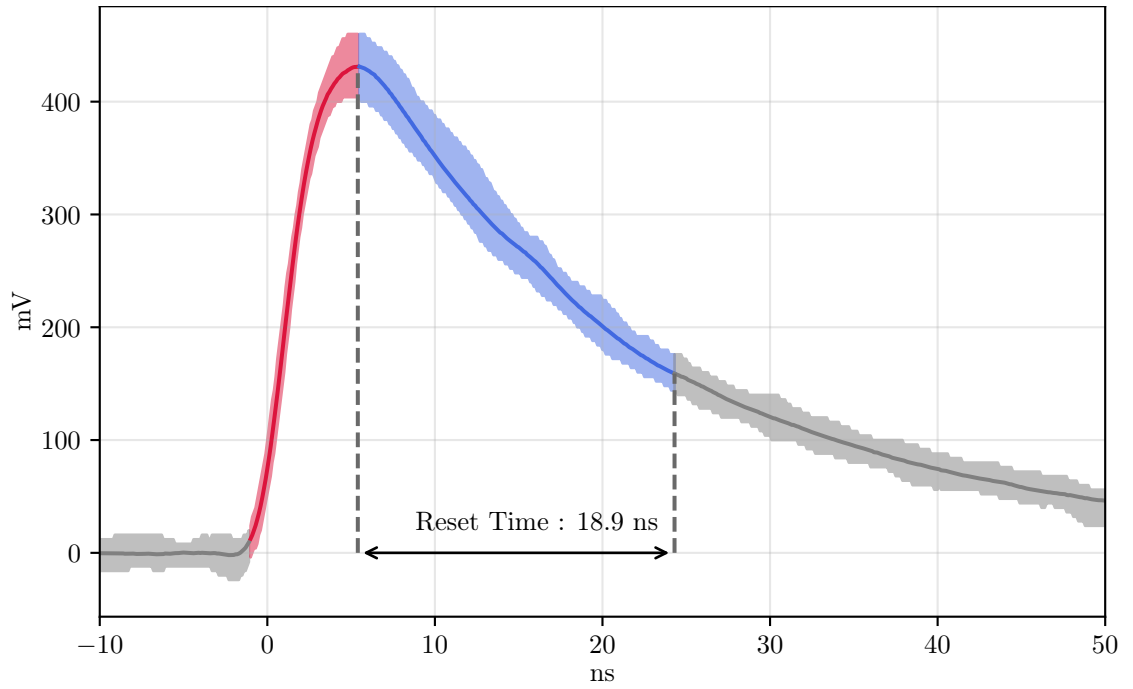
Figure 3.2: **Detector reset time.** Here we see the output waveform produced by a photon detection event at a Quantum Opus superconducting nanowire detector. To measure reset time we calculate the $\frac{1}{e}$ fall time of the waveform, this is the time taken for the amplitude, A, to go from its maximum to $\frac{A_{\max}}{e}$. The result here of $\approx$ 19ns agrees closely with the quoted value from the manufacturer of a nominal reset time of $\approx$ 25ns suggesting that these detectors are capable of detection events without the need for the output to reach the signal floor fully. Considering that this is a superconducting detector we can assume that detection efficiency will reduce if we input a stream of single photons with this spacing as the nanowires will not have had time to fully cool down. Alternatively the "90→10" reset time could be used, where we measure the time between 90% and 10% of the maximum amplitude.

3.3.1 Reset Time

A final parameter to be determined before validation is the detector reset time τ_{detector}. Fortunately, this can be easily measured with a fast oscilloscope. In order to gain an average value for the reset time across all available detector channels we recorded 10 traces for each detector channel and calculated the average reset time.

In fig. 3.2 our average detector response is displayed. We define the reset time as the time between the maximum recorded voltage and the point it reaches $\frac{1}{e}$ of this level. Here we find that value to be 18.9ns.

3.3.2   Combinatorial Model Validation

Now with a complete set of input parameters we can proceed to validate the combinatorial model. In doing to so we will be estimating the values for γ and for η (on each detector channel), first this will be through a simple power dependent characterisation of an SPDC pair source.
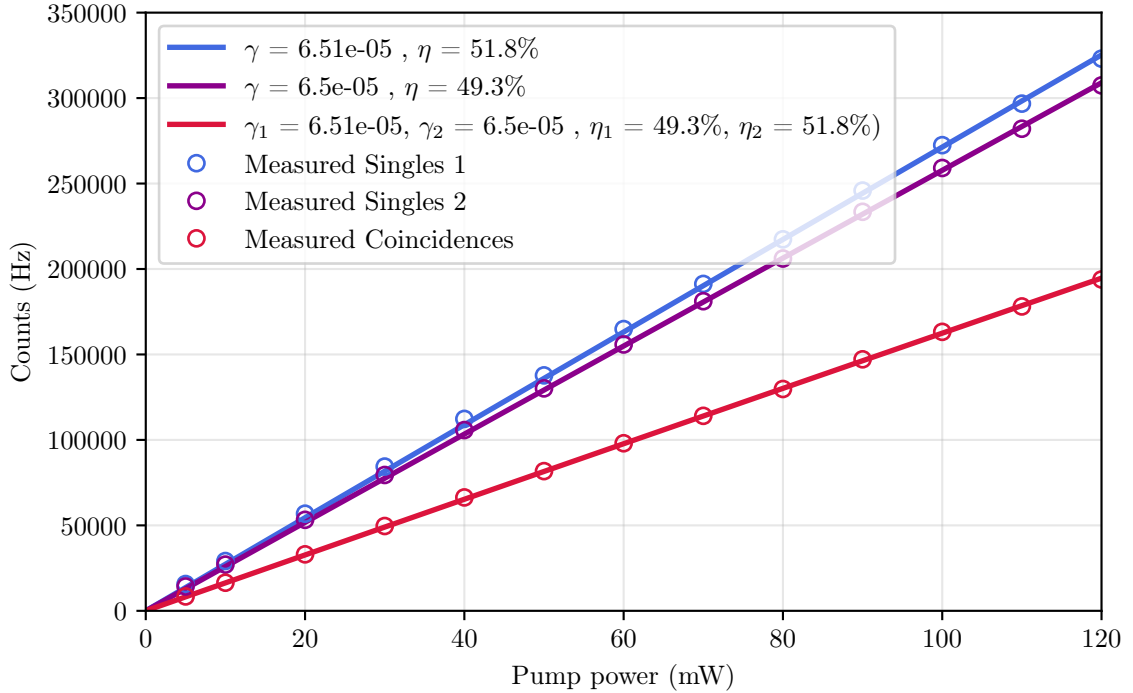
Figure 3.3: **Calibration of combinatorial model against power dependent single photon and photon pair detection events.** The circles here represent measurement data points with the lines a regression fitting of the model against them, produced error bars are smaller than the symbols. We use linear regression to estimate the γ and η parameters of our model to determine the "nonlinearity" and detection efficiencies seen in the measurement. Here the "nonlinearity" is in fact an encapsulation of the pump pulse — PDC crystal interaction. Given the measured 60% heralding efficiency the fitted efficiency of $\approx 50\%$ gives us confidence in the model when considering the quoted 80% detection efficiency from the manufacturer.

Power dependence

Just like in all of our experiments mentioned throughout this thesis, an 80 MHz picosecond pulsed laser operating at 775 nm pumps a 28 mm long ppKTP crystal to generate photons at 1550 nm which, after some beam-conditioning, are coupled into single-mode fibres an then detected with SNSPDs. We record photon pair rates as a function of pump power P as shown in fig. 3.3 Here we have fitted against the

count rates seen at each independent detector as well as the resulting coincidences. From the legend in fig. 3.3 we can see that the resulting values for γ and η in both of the singles count rates as well as the coincidence count rates are consistent between the combinatorial model and the laboratory measurements, with one detector operating at a slightly higher efficiency than the other and with all γ values being approximately equal. Whilst a simple case to test against, this proves promising for further application of the model.

Second-Order Coherence, $g^{(2)}(0)$
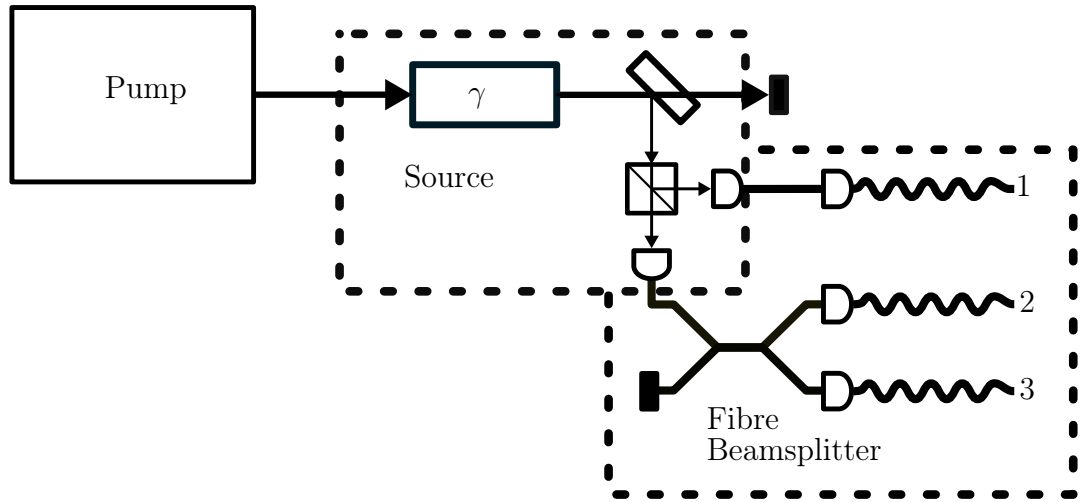
Figure 3.4: **Experimental scheme for $g^{(2)}(0)$ measurement.** Channel 1 is sent straight from the source to the detectors whilst the second output of the source sent to both detectors 2 and 3 after arriving at a fibre beam splitter. From this measurement we can determine the probability of the source emitting more than just a single pair of photons at a time.

Next, we move on to a slightly more complicated case for the model, although one we planned for it to be able to analyse, the second-order coherence $(g^{(2)}(0))$, the experimental configuration for which can be seen in fig. 3.4. Second-order coherence is an important metric to measure when developing a single-photon source since it benchmarks the photon-number purity of the state. A true single-photon source would have a $g^{(2)}(0) = 0$. Here we estimate the γ and η values found from data collected in a power-dependent $g^{(2)}(0)$ experiment, this involves passing one of the outputs of the SPDC source over a beam splitter in doing so the volume of multiple

emissions being generated per pump pulse can be determined.

Figure 3.5: **Fitting the single and pair photon detection events from a** $g^{(2)}(0)$ **measurement.** Fitting against the power dependent count rates from series of $g^{(2)}(0)$ measurements we can see our comb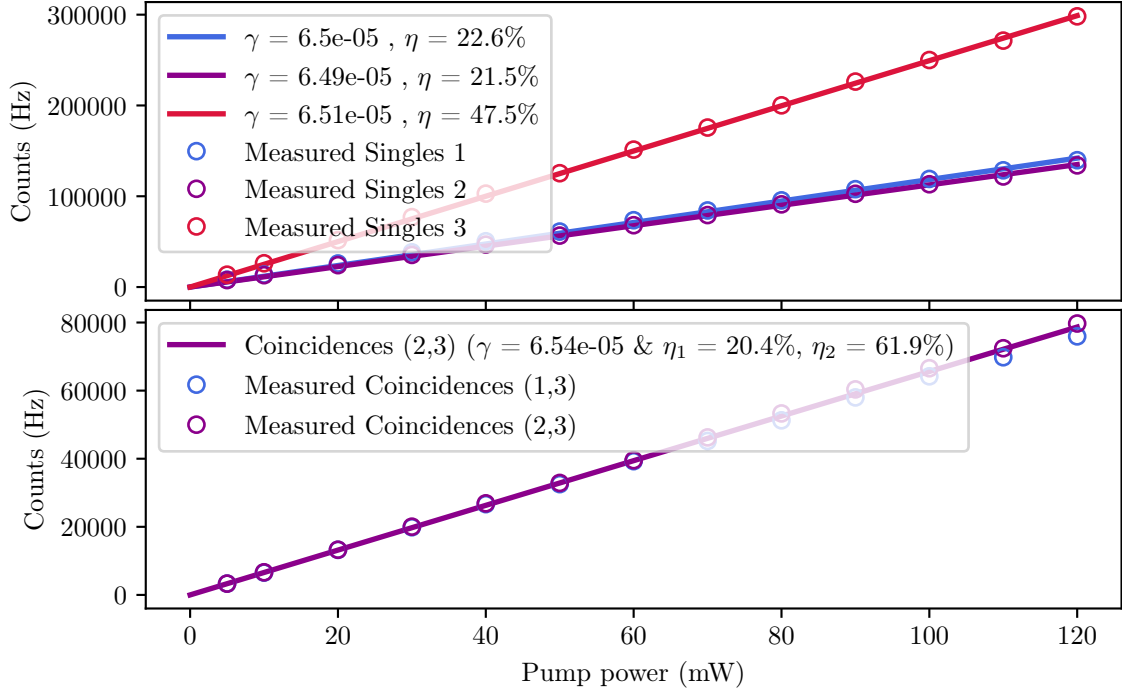inatorial model successfully estimate the γ parameter for each channel consistently with those estimated in fig. 3.3. Further the estimated value for the system detection efficiency on each channel matches our expectations with the channel sent straight to the detector producing an efficiency comparable to those in fig. 3.3. Next for emissions split on the beamsplitter we see an approximate halving in efficiency which we expect given that the number of photons produced is being roughly equally shared between a pair of detectors.

First we fit the count rates observed at the individual detectors. From fig. 3.5 we can see that two of the three channels have efficiencies in the 20% range and one in the 40% range corresponding to the splitting of one output of the beamsplitter. Again we can see that the γ value is consistent across the data and with the values shown in fig. 3.3.

Now we turn our attention to the coincidence counts seen between each of the detector channels. First we have the pair rates seen between each arm of the beamsplitter with the unsplit arm of the source. Again we see consistent parameter estimation. Next, the coincidences observed between all three detector channels, fig. 3.6 shows that the model can fit this more complicated case whilst still returning values for $g^{(2)}(0)$ consistent with those found in the "simpler" cases.

Finally we use the model to fit the resulting $g^{(2)}(0)$ data in fig. 3.6. As shown

here we find it safe to operate under the assumption that the model is suitable for answering our questions relating to optimal conditions and speed limits present in optical experiments.
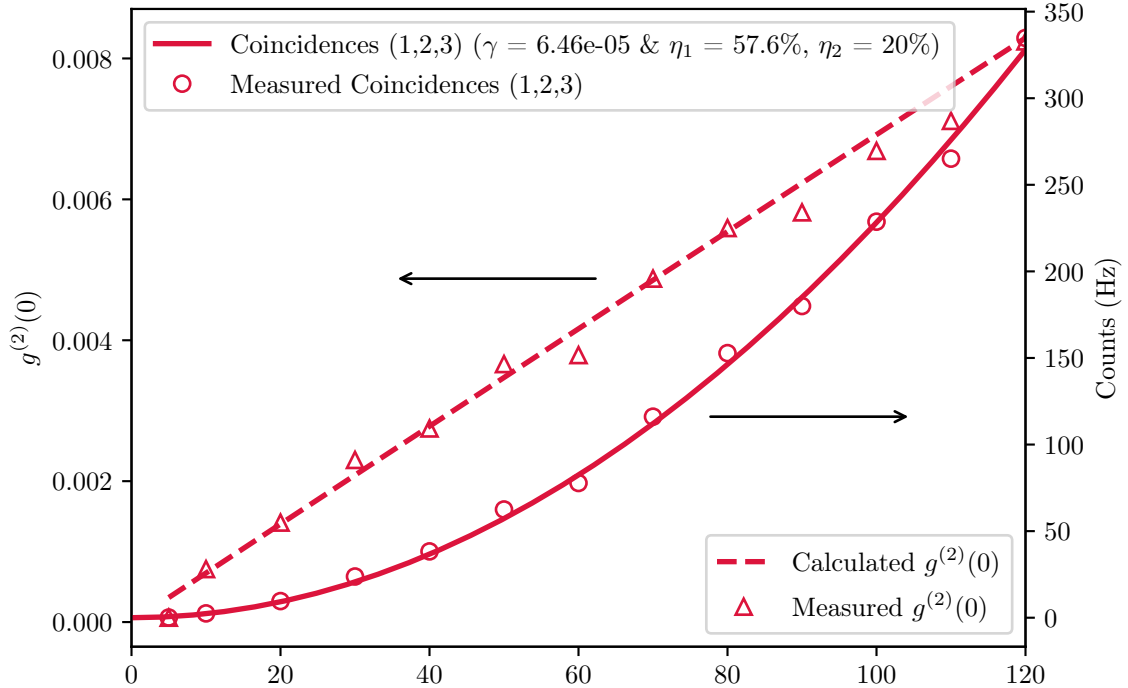
Figure 3.6: **Calibration of combinatorial model against power-dependent** $g^{(2)}(0)$ **values and three-photon detection events.** For full validation of the combinatorial model we now compare the three-photon detection events across each of the detectors along with the estimations from the model for the second-order coherence. The symbols represent the measured data with the lines displaying the result of linear regression fitting of the model against the data points. We see in both cases our model agreeing closely with that of the measured data, telling us that the model is capable of estimating effectively the amount of higher-order emissions produced for every single pair emission. This is a useful capability in cases where we want to be able to estimate the effective nonlinearity present in a PDC source.

3.3.3   Monte-Carlo Model

We must also validate the Monte-Carlo based model, for this we have used the same experimental data to fit against. As can be seen from the accurate fits in section 3.3.3 the Monte-Carlo model is equally suitable for predicting $g^{(2)}(0)$.

The curves in the figure were produced from 8×10^9 samples (where each pulse is considered one sample, this is then broken down into 100 super samples of length 8×10^7). Using the same source and detection parameters found from the combinatorial model the Monte-Carlo based method calculates a value for $g^{(2)}(0)$ approxi-

mately equal to the experimental data, showing the ability for both models to map effectively onto out measured data.

Since this method relies on sampling instead of calculation of a value outright to make prediction for $g^{(2)}(0)$ we show both the mean and standard deviation for each power setting. Doing so shows that with this sampling based method we are capable of fitting the measurement accurately and reliably with each of the measurements lying within the shaded region defined by the standard deviation.
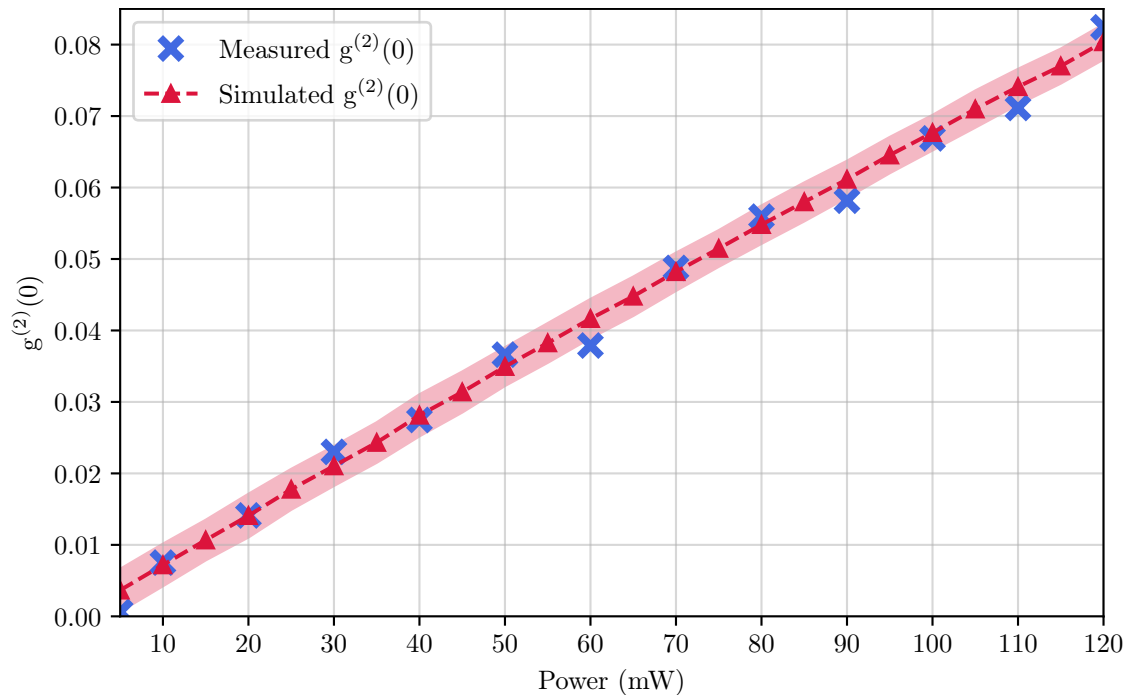
Figure 3.7: **Resulting of Monte-Carlo model estimation of** $g^{(2)}(0)$**.** From the combinatorial method we use the γ and η estimations as input parameters for the Monte-Carlo based model. We see that this model is capable of closely estimating the measured values at each power also providing an error range arising from the sampling process. The dashed line marked by triangles represent the mean $g^{(2)}(0)$ calculated for 8×10^8 samples in 5mW increments upto 120mW. We use the model to generate estimates at smaller power intervals to avoid the chance of missing any unexpected behaviours arriving, the result we see here provides us confidence in the suitability of this method.

To conclude, both of the models developed provide a suitable fit to the experimental data are both promising candidates for exploring the effects present in generation and detection of photons taking into account features like detection (or switch) efficiency as well as the reset/dead times of various components. It should be noted whilst the data can be fitted with both models they do not produce identical values, we see a tendency for the combinatorial model underestimate signal-to-noise

ratio while the Monte-Carlo model overestimates it. This discrepancy comes from the Monte-Carlo model considering the case where one photon is lost from each mode of a double (or higher) emission event from the source to be a successful detection event. In other words, it considers it to be signal, whereas the combinatorial model always considers these as noise. However given the consistency in the results for $g^{(2)}(0)$ and for the number of events seen at the detectors we can consider them both to be suitable methods for optimising the performance of multi-photon experiments for quantum information processing.

Chapter 4

Speed Limits for Quantum Photonics

With two models defined in chapter 3 we can now turn our attention to fine tuning the free experimental parameters available to us in order to optimise multi-photon QIP experiments. One question of particular interest to us relates to passive temporal multiplexing: is there a "speed-limit", or in other words an optimal laser clock rate assuming finite pump powers. To ensure that the detected state is the one we intended to generate we need to collect enough samples such that the statistical errors have been constrained enough. This leads to one of two cases, either operating with a high signal-to-noise ratio and short measurement times or the opposite — low signal-to-noise and long measurement times. In these terms we define the signal as the number of single pair events per source created and noise as the number of higher-order events created per source. This behaviour is outlined in the expansion of eq. (2.3) [131]

$$|\Psi_{SPDC}\rangle = \sqrt{1 - |\lambda|^2} \sum_{n=0}^{\infty} \lambda^n |n_s, n_i\rangle \tag{4.1}$$

where the single pair events correspond to $|1, 1\rangle$ and the higher-order events come from $|n_{i,s} \geq 2\rangle$ (where subscripts s and i denote signal and idler modes respectively).

Before diving into the details present in the interactions between the various free parameters available to the models it is perhaps worthwhile to cover some of the more immediate intuitions we have as to what defines speed limits. We should first remember that we are restricting all of our discussion to that of PDC sources and as a result we can say that regardless of our sources' ability to emit single photons

there exists a limit to how fast the source can be triggered, once the pump pulses begin to overlap we can no longer increase the clock speed. Typically this clock speed is well beyond the rate of single photons detected but nevertheless provides an absolute upper bound on the maximum emitted and so detectable rate. Next we should consider that our detectors are saturable given that they posses a reset time, providing a further limit on the maximum detectable rate. With just these two initial conditions we can define how fast it is possible for experiments to be able to operate, whichever of the two provides the lowest maximum rate sets our absolute maximum detectable count rate. We can group together power and γ parameter as these both influence the emission probability for SPDC based sources in the same way in that increasing either will lead to an increase in detected count rates. Finally the detector efficiency η provides our final limiting condition, however it may prove more useful here to consider this to behave more like an inclusion of loss in the system rather than an upper bound as defined by clock speed and reset time. Considering detection efficiency as loss can be useful here as it determines how quickly we reach the saturation limit of our detectors, this is an idea that will prove useful as we explore the behaviours that limit us when considering the creation and detection of multi-photon events.

4.1   Signal-to-noise Ratio (SNR)

Discussion of speed limits present here is further complicated when considering the SNR produced by any given combination of input parameters. Whilst it may be possible to produce incredibly high rates of photons it may include a larger than desired volume of noise with it in the form of more than one photon being present in each detection mode. From the model we define the "Signal Counts" as the emission and detection of only the photons we want to detect for example only the photon pairs emitted by a PDC source and then "All Counts" to include the emission of multiple pairs. From this we can define the SNR as:

$$\text{SNR} = \frac{\text{Signal Counts}}{\text{All Counts - Signal Counts}}, \tag{4.2}$$

we can evaluate our models for the condition where we have signal produced in

which one photon is detected per mode and in the presence of noisy emissions in which more than one photon is present per detection mode.

4.2   Parameters

In our desire to increase multi-photon generation and detection rates we need to explore the behaviours presented by the interactions between clock rates, pump power, detection efficiencies and detector reset times. To understand the relations found between these parameters here we look specifically to the effects brought about through timing (clock rates and reset times) as well as the emission probability (nonlinearity of the crystal and pump power).

4.2.1   Clock Rates

Whilst we may see the ability to increase the clock rate as the most obvious means to increase our overall detection rates we must remember that this brings with it a couple of limiting cases, aside from the lack of tuneability of the repetition rate of commonly used titanium-sapphire lasers for QP experiments. Increasing of the repetition rate with fixed pulse width eventually leads to the continuous-wave limit and discrete pulses can no longer be distinguished, under this condition we are also met with the loss of timing information as well as lowering the emission probability (granted, this will increase the signal-to-noise ratio however it is at the cost of overall emission rates). It is worth noting here, there exists some interplay between clock rate and pump power, i.e we can't increase the clock rate and the pulse power simultaneously, at best we can maintain the average pump power whilst increasing the clock rate. The interplay present here can be clearly seen in the case of temporally multiplexing a pump source, in which we choose to split the path of the pump source and apply a delay of half the clock width to one arm before recombining such that we trade in half the pulse power to gain a doubling in clock speed [65]. Secondly, as the clock rate gets increasingly high we will eventually reach the maximum detectable rate of our detectors as this will no longer be able to reset quickly enough. So, we either run into the condition that such a high clock rate eventually reduces our emission rate or we operate beyond the capabilities of our
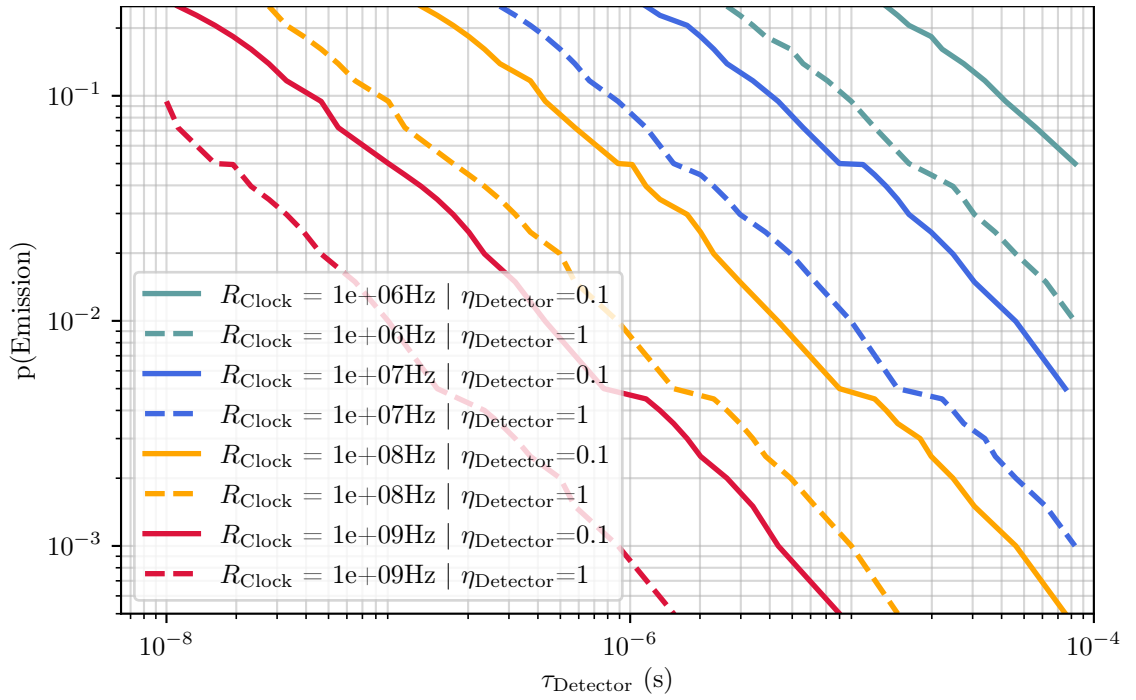
Figure 4.1: **Emission probability to saturate a detector at a given clock speed.** Illustrated here are the ranges over which a given emission probability and detector reset time τ will reach saturation. For clock speeds ranging from 1 MHz to 1 GHz we have a region bound by the detection efficiencies of $\eta = 0.1$ and $\eta = 1$ indicating how quickly we would expect a certain emission probability or reset time to lead to detector saturation. Increasing the clock rate by an order of magnitude causes saturation of the detectors at lower and lower emission probabilities, fortunately given that we might need to trade in pump power (emission probability) in order to increase the clock rate we can still maintain high detection rates even at lower pump powers, as the saturation points shown here highlight.

detectors. Ideally we would like to operate as close to the limit of the detectors as we can but below the point at which our pumps pulses begin to overlap with each other.

The connection between power and clock rate can be exploited by a rephrasing of the clock source, instead of considering a single pulse per clock cycle we can instead move to a picture where we have multiple time bins per clock cycle. In this reference frame we have chosen to group a number of pulses together. The previously mentioned temporal multiplexing of the pump source provides a convenient example of this concept as we maintain the definition that the repetition rate of our pump is our clock rate but we now choose to break this up into a series of pulses with lower pulse power at equally spaced time bins. In having a number of time bins per clock cycle, we can take the increased SNR due to the lower power and now choose to use

the grouping of time bins (and so the increased number of opportunities to generate single photons) to increase the probability per clock cycle of our sources.

4.2.2 Emission Probability (Nonlinearity and Pump Power)

To increase our detected count rates we may alternatively choose to increase the emission probability of our sources either by use of a longer crystal to increase the interaction time time with the pump, use of a crystal with rectangular nonlinearity profile or by increasing the pump power (or any combination thereof). Both of these options will provide an increase in the volume of higher-order emissions from the source as well and as a result degrade the SNR.
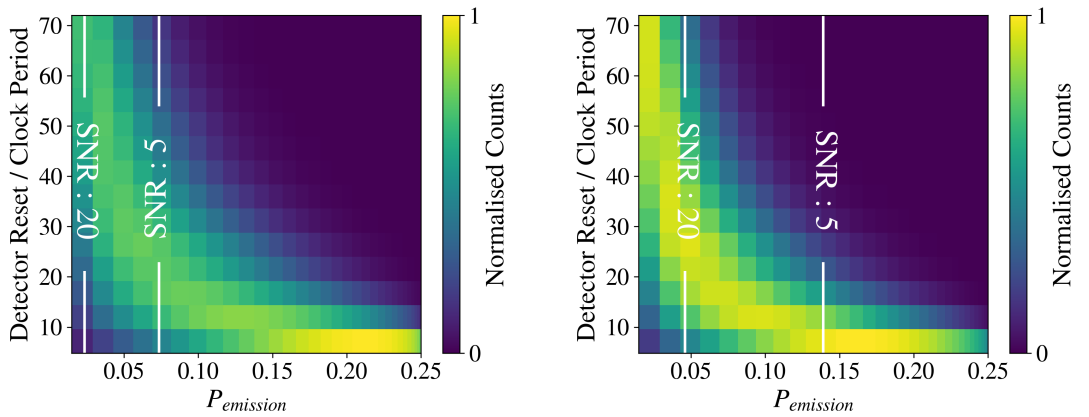
Figure 4.2: **Detector saturation behaviour for** $\eta = 0.5$ **(left) and** $\eta = 1$ **(right).** As the clock period is reduced (increased clock speed) whilst detector reset time is held constant it remains possible to reach detector saturation even at low emission probabilities (low power / low nonlinearity). Detector saturation is, as expected, more easily reach as detection efficiency increases, however it can also be seen that there exists a region where maximum count rates can be observed whilst still maintaining good SNR. SNR contours plotted over each heat map illustrates the benefit from operating in these regimes as it points to the ability to maintain high count rates at low operating powers. Counts have been normalised according to the maximum count rate seen over the entire map respectively to allow for comparison between higher and lower detection efficiencies.

The relation between clock speed, detector reset time and emission probability (power and nonlinearity) is displayed in fig. 4.2 for SPDC sources. We see that increased emission probabilities from an increase in power do not always provide an improvement in the detected count rates. It is worth noting that power and

nonlinearity have been grouped together as we can use these to define the emission probability, clock rate and reset time have been grouped together as well in fig. 4.2 Doing so we can move away from the specifics that exist for a given combination of sources and detectors, instead looking at the general behaviour existing between high or low emission rates compared with "good" or "bad" detectors (good being high efficiency and short reset time).

Naively, it would appear that there is little sense in operating beyond what is possible to detect. However, in the presence of loss and noise and with the use of probabilistic sources we are not met with a single (or more) emission per pump pulse (clock cycle) at the detectors. Instead more often than not signal will reach the detectors, this implies operating at clock rates much higher than what is detectable can be beneficial [125]. From our models this becomes something that can be easily explored, as we proceed to increase the clock rate we encounter a significant problem for building these larger states, detector saturation occurs earlier for multi-photon detection events than it does for single detection events. In essence if we wish to detect 8-photon coincidence events the production (detection) of all smaller coincidence patterns (a pattern being any combination of n out of k detector channels) will saturate the detectors, as a result lower order events blind the detectors to the higher-order events that we want to detect.

4.3   Multi-Photon Detection

As stated in the previous section, detection of higher-order events (which due the Poissonian nature of the sources has the same probability to that of multi-photon events produced from multiple single-photon sources) becomes increasingly difficult as the rate of single detection events also increases. These single detection events effectively result in a blinding of the detectors to the multi-photon events. Since we are investigating the speed limits present for multi-photon generation we are limiting our analysis towards bucket detectors rather than including number resolving detectors, due to the long reset times present in current superconducting transition edge sensor. Number resolution with faster SNSPD's at high efficiency may soon be available though [37], in which case it would be worth revisiting this scenario.

In fig. 4.3 we show the limitations in trying to detect 2, 4 or 8 photons from PDC sources (1, 2 and 4 heralded sources). In each case to access the higher generation rates we want to operate a quantum photonics scheme we need to increase the brightness of the sources, this however comes at the cost of greater higher-order
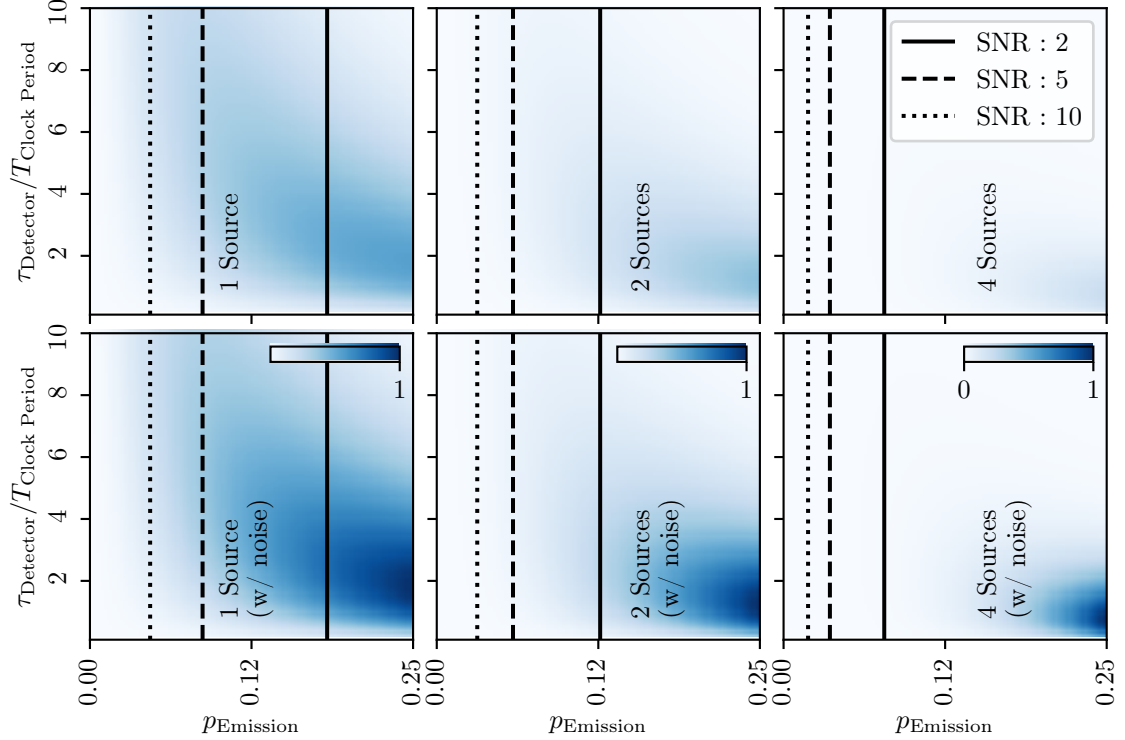

Figure 4.3: **Detector saturation behaviour for a range of single photon sources: left — 1 source, centre — 2 sources, right — 4 sources.** Here we see the detectable rates of 1, 2 and 4 heralded PDC sources where we increase the clock rate of the pump laser with respect to a fixed detector reset time so as to observe the effect of faster operation. For each source both the pure signal and the signal with higher orders are shown as the top and bottom rows respectively, further lines have been added to note the contour for where signal-to-noise ratio decrease (left of each line the ratio is lower and right of each line the ratio is higher). For each source the count rates in each plot have been normalised to the maximum of its respective plot with higher order effects so the effect of each alone can be more clearly seen. Given that PDC sources are capable of emitting more than a single pair of photons, we expect that these extra photon pairs should cause earlier detector saturation, as shown by the lower row predicting higher count rates than the upper row. With the contours added to show coarse regions for certain signal-to-noise performance limits the difficulty of producing a larger and larger multiphoton detection events becomes increasingly apparent, however we can begin to see that increasing the clock speed (decreasing the clock period) when compared to the detector reset time that it should become possible to achieve a high signal-to-noise ratio at a high count rate (corresponding to the darker regions of the above plots). In order to do this we have to reduce our emission probability so that we can suppress the volume higher order emissions.

emission and so lower signal-to-noise ratios. Alternatively we could choose to increase the rate at which we pump our sources (shown on the y-axis of each plot with respect to fixed detector reset time) allowing for a target signal-to-noise ratio to be maintained while operating closer to the detector peak count rate. This outlines the problem in trying to generate large multi-photon states before even considering how we want to use any of the photons. Generation of larger and larger multi-photon detection events is limited by emission characteristics of the source in use.

4.4 Multiplexing

As has been pointed out now a few times, the only way to make PDC photons more deterministic is by multiplexing several heralded sources, so in this section we will be modelling various multiplexing schemes while looking at the same speed trade-off as before, i.e. what are the benefits from running at much faster clock rates then e.g. the detector peak rates suggest. Multiplexing of single-photon sources can be realised either spatially or temporally (or by a combination of the two), alternatively there exists the option of frequency multiplexing.
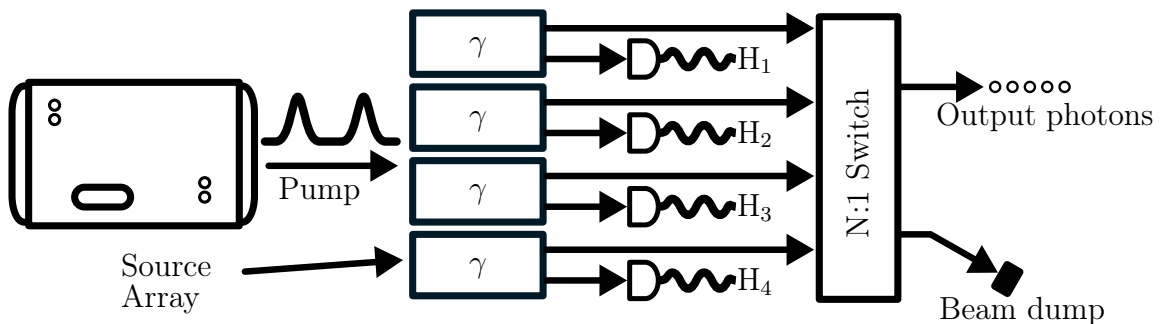
Figure 4.4: **Spatial multiplexing schematic.** By operating a series of single-photon sources in parallel and connecting the output of each through either a beam splitter network or an N:1 switch yard using active feed forward conditioned on the first source to herald a photon, we can combine their outputs into a single output mode. From the work seen in [64] it could be possible to achieve near deterministic output from 17 PDC sources should number resolving detectors be used.

Migdall *et-al.* proposed in [132, 133] that one could switch several heralded single photons into a common output mode using a series of 2:1 switches [64, 115, 134]. Ma et-al. then realised the first of these schemes with 2 PDC sources and

a 2:1 switch implemented via polarisation switching in a Pockels cell [135], more recent implementations have been done in integrated photonics [115] where both spatial and temporal multiplexing have been combined to increase the probability of successful multi-photon events whilst simultaneously increasing the signal-to=noise ratio. Discussion of several active spatial switching schemes (e.g. Jennwein *et-al.* [135], Francis-Jones *et-al.* [128, 136], Hoggarth *et al* [122] and Zhang *et-al.* [37, 116]) will be undertaken later within the chapter. Earlier numerical modelling of various switching schemes [114, 129] showed that a N:1 switch-yard performs better than an 2:1 switch-yard due to fewer switches, and that overall it would be desirable to have photon-number resolution, however, practical devices are still subject to too higher loss reducing the probability of successful multi-photon detection events. Both of these cases come with their own advantages and disadvantages, passive schemes may be simpler to construct and operate with lower loss however come with increased noise as we can have more than one photon per clock pulse whereas active schemes are subject to higher loss, limited switching speeds and increased complexity however could achieve higher signal-to-noise ratios.
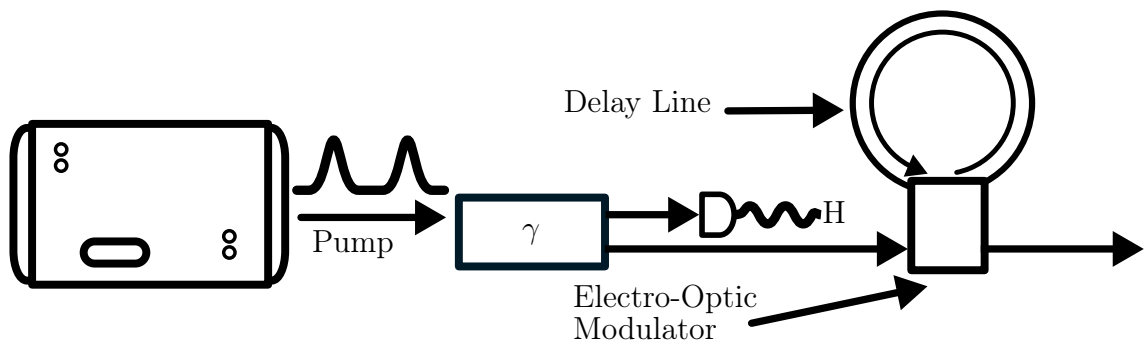
Figure 4.5: **Temporal multiplexing via optical switch and delay loop.** By making use of a heralding signal to open or close an optical switch we can store a photon until we need it, for example when another source sees a heralding signal, then releasing the stored photon so that we can herald more than just a single-photon. This idea can be extended to holding a number of heralded photons from the same source for later use, in doing so we can increase the success rate of our quantum photonics scheme by only releasing the newest photon in the loop when it is needed.

As for temporal schemes we can improve our emission probability by a change of reference frame, instead of considering the emission probability per pulse we move to emission probability per clock cycle. When considering emission probability per

clock cycles two options key cases become apparent, either a number of pulses are grouped together lowering the overall clock rate or a pump pulse is sub-divided into a pulse train of pulses with lower individual power. Both of these methods seek to increase both the emission probability whilst the second allows for an increase in the signal-to-noise ratio too. Should we choose to combine a series of pulses like the methods described by [117, 120–122, 137] where a looped delay line is constructed by connecting an optical switch to either keep the photon travelling along the storage loop or letting it pass to be used elsewhere. This design allows for a single photon to be stored for later use or to combine the emission probabilities from a number of pulses by recirculating each through the storage loop. In these cases the choice to allow a photon into the loop is controlled by either the clock of the experiment or
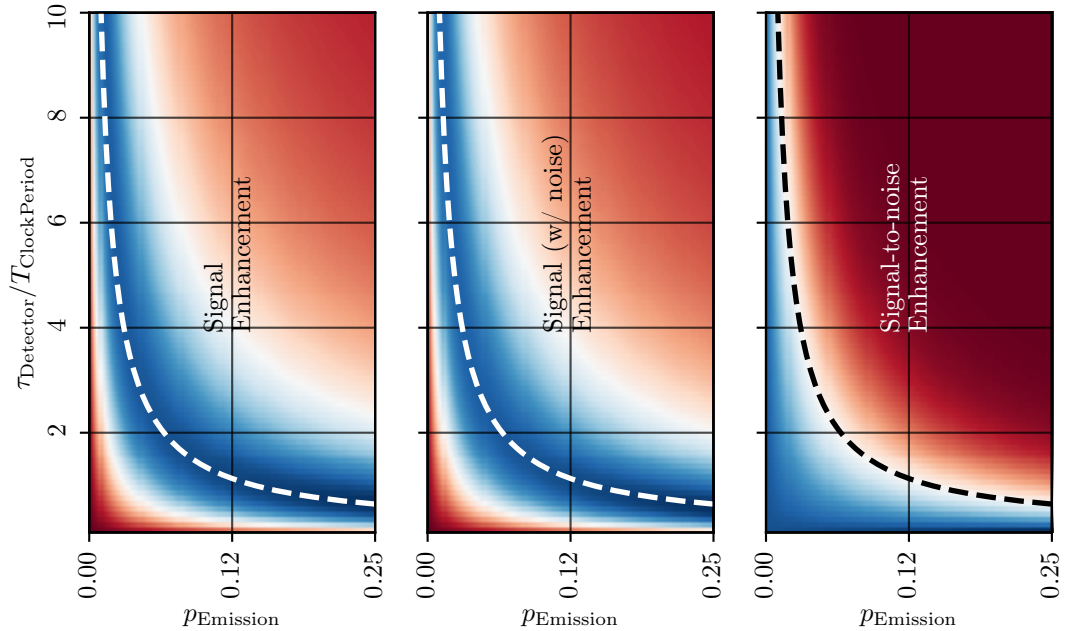
Figure 4.6: **Performance enhancement between a heralded single-photon source and a temporally multiplexed single-photon source using the loop architecture: left — signal, centre — signal with higher order emissions, right — signal-to-noise ratio.** By plotting emission probability against increasing ratio in detector reset and clock period we can see the effects how much benefit there is to operating the trigger channels of each source at higher and higher rates for the same reset time. The dashed line found on each sub-plot represents the point at which the signal-to-noise ratio enhancement is one, i.e. where they are the same. From the signal-to-noise plot we can then infer from the other sub-plots the ranges at which we see benefit from increases in either parameter. The bound between lower blue edge and dashed line represents where the benefit in both maximum detectable rates and signal-to-noise performance.

by the heralding signal of the source, with a second heralding signal from a separate source supplying a trigger signal to signify it being time to release the held photon. In both cases it becomes possible to increase both the emission probability of single source as well as the multi-photon rates needed to build larger states. From fig. 4.6 we can see how beneficial these temporal multiplexing schemes can be in terms of single source performance. The region in the "Signal (w/ noise) Enhancement" sub plot bounded by the lower blue edge and the dashed line shows us that under the right conditions the loop architecture will outperform both the detected rates and signal-to-noise of a standard heralded source. Given that we want to operate PDC based sources in the lower $p_{Emission}$ regime, as this means fewer higher-order emissions, there is a significant performance gain to be had in increasing the clock rate with respect to that of the detector reset time.
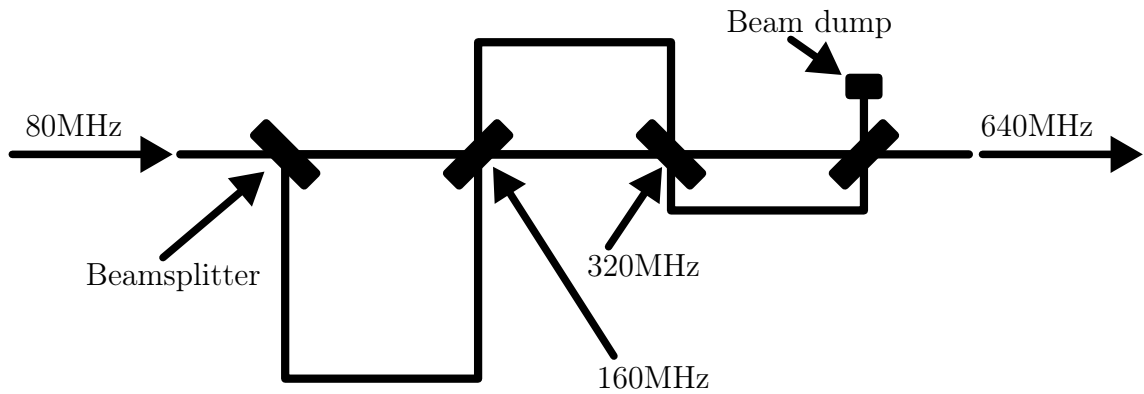
Figure 4.7: **Temporal pump pulse multiplexing.** In the temporal pump pulse multiplexing case a pump pulse is divided amongst a number of time bins resulting in a number of lower power pulses at equal distances apart over the initial pump pulse period. In dividing the pump pulse into a series of lower power pulses the signal-to-noise ratio can be increased for PDC sources as the input power per pulse is reduced leading to a lower probability of emitting more than a single-photon pair, combined with the increase in repetition rate experienced by the source the overall emission rates should remain constant.Increasing the signal-to-noise ratio in our measurements allows us to quicker constrain the statistical behaviour of our sources and reducing the power applied to PDC sources is an obvious method to realise that however this comes at the cost of lower emission probability. The increase in repetition rate from temporal pump multiplexing allows us to circumvent this issue and in the case of very bright sources it could allow us to combine high speed operation with high signal-to-noise.

Alternatively splitting a pump pulse into a series of lower power pulses spanning the peak-to-peak time of the pump's clock period under the guise of temporal pump

pulse mutliplexing [65, 116, 117, 120, 138, 139] provides an increased effective clock rate and a number of time bins per clock cycle of the pump laser. Under this regime it becomes possible to increase the emission probability per clock period by gaining the opportunity to generate photons multiple times per clock pulse. As previously stated in chapter 3 this allows for both an increase in the emission probability and the signal-to-noise ratio as the higher-order terms present in eq. (4.1) can be suppressed by the lower pulse power of each generation event however the first-order term is affected less and the increase in repetition rate should make up for the reduction in emission probability at lower pulse power. By including active switching this can be further extended to the synchronisation of multiple single-photon sources [139, 140]. The schemes described there target multi-photon event generation across multiple sources rather than increasing the emission probability of a single source.
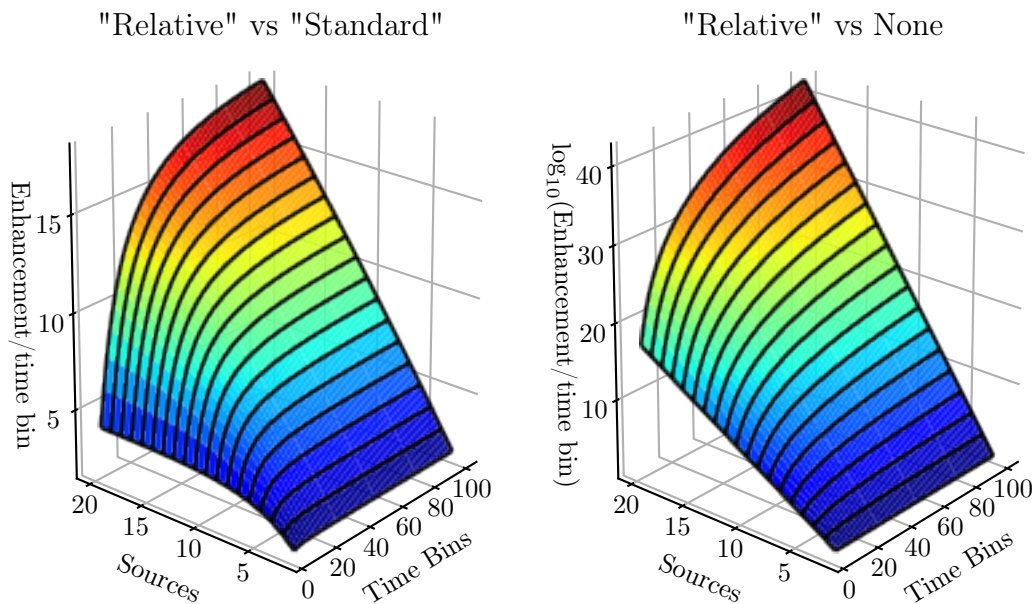
Figure 4.8: **Performance of: left — relative temporal multiplexing versus standard temporal multiplexing and right — relative temporal multiplexing versus no multiplexing.** Whilst the enhancement in detection rates between the 2 types of temporal multiplexing schemes is significant showing how multiplexing can see further improvement by synchronising sources together for better multi-photon detection rates, the improvement seen when comparing the relative scheme to no multiplexing at all is even more significant with an exponential increase in performance as the number of time bins per clock cycle and number of sources increase.

Moving now to the pair of "Relative Temporal Multiplexing" (RTM) schemes

from Zhang *et-al.* [139, 140] of which are designed to synchronise the output of a number of heralded single-photon sources. The first method presented in [140] operates by delaying the outputs of each source to bring them into the same time bin as the last recorded heralded signal, with the second [139] method extending this idea to synchronise and place all heralded photons in the first time bin of the next clock cycle. Focusing on the second of these, we plot the behaviour for increased emission probability and increased clock speed with respect to a fixed reset time we see markedly different performance than that of source based on loop architectures. Whilst both are temporal multiplexing schemes making use of the combined probabilities of a series of pulses, these relative schemes lend themselves directly to increasing multi-photon detection events and suppression of the higher-order terms that degrade the signal integrity associated with them. Comparing fig. 4.9 and fig. 4.3, the effect of clock speed has a much greater effect on the total detectable rates than previously when applying temporal multiplexing compared to operating an array of sources with no co-ordination between them. The emission probability naturally plays a key role however we see that saturation of the detectors now begins to happen before it is maximised meaning that we the maximum detection rate occurs before the signal-to-noise ratio becomes too small.

From the results in this section it seems clear that pushing the clock speed of an experiment beyond the maximum rate the detectors are capable according to their reset times leads us to greatly improved performance of either single or multiple sources when combined with spatial multiplexing along side operating the clock at a faster rate.

Multiplexing is not limited to just single-photon sources, we can extend these ideas to the detectors as well [37, 116, 123, 124]. Given that our detectors need to reset in order to detect again one might use either passive multiplexing using a series of beamsplitters and detectors per photon, to reduce the probability of one photon arriving at an individual detector. Active routing involves multiple detectors behind an 1:N switch-yard. Upon triggering one detector, photons can be rerouted to the next available detector while the original detector resets. Both methods lower the effective reset time, a necessity once emission rates reach the maximum peak detection rate. As with multiplexing of sources, active methods applied to detectors
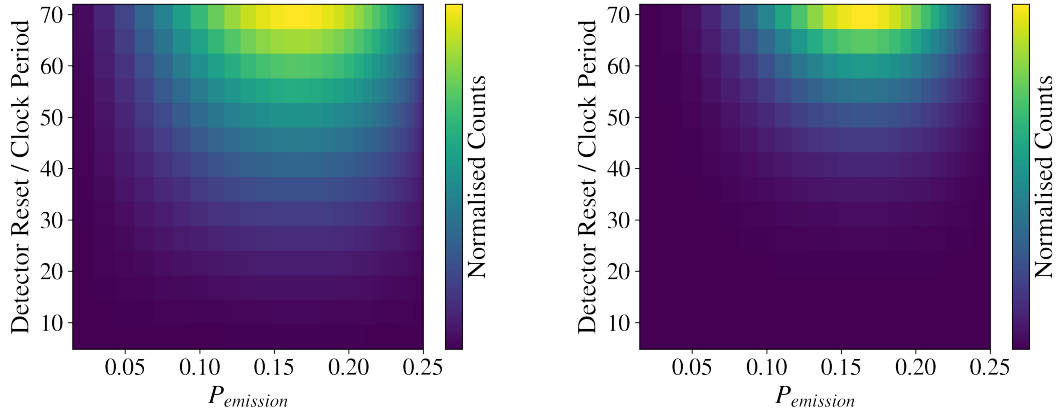
Figure 4.9: **Detector saturation for a relative temporal multiplexing scheme.** Left — two pair sources, right — four pair sources. Using relative temporal multiplexing to synchronise a number of sources can provide a means to increase the probability of detecting and so the detected rates of multiphoton events. We see that in the case of the case of relative temporal multiplexing we saturate the detectors before we reach maximum emission probability of our PDC sources. This means that faster operation at higher signal-to-noise is within reach by introducing active synchronisation between a collection of PDC sources.

introduce further loss and speed limits by adding switching reset times. Our model can incorporate these methods, however this was not used in our laboratory since we don't typically have lots of excess detectors available.

4.5   Global Sensitivity Analysis

In the previous section we studied the impact of individual parameters on the performance of typical multi-photon experiments. Here we go one step further and perform a so-called global sensitivity analysis (GSA) which will provide a ranking of individual parameters in terms of their overall impact on the system. This knowledge can then be translated to an experimental setting and tell us in a general sense which element(s) of the experiment should be improved to gain the largest increase in the detected rate of single (pairs of) photons and the signal-to-noise ratio of the multi-photon event we want to construct.

A typical approach when investigating a systems response is to vary one of the parameters and monitor the change in the output. To this end a GSA framework provides a method to investigate the interactions present between each parameter

of a model and the model's output. More specifically GSA determines both the amount and the kind of change of a model's output in response to change in the model's input. The sensitivity analysis results in a sensitivity index for each model parameter detailing the correlation of changes in the input with the output, these indices typically take one of three forms, either;

1. First order: measurement of changes from a single input parameter only.

2. Second-order: measurement of changes from a pair of input parameters, i.e. the contribution from interactions between input parameters.

3. Total-order: measurement of all changes from the first-order effects and all higher-order effects.

We chose to apply the Sobol [141] method to the combinatorial method described in chapter 3, for N sources with and without relative temporal multiplexing. In applying to these cases we can see how best to optimise a number of "off the shelf" heralded sources as well as how optimisation is possible for temporal multiplexing. Most importantly this will identify trends for both, telling us how to optimise for multi-photon experiments in general. The Sobol method is an approach to GSA making use of changes in the *variance* in the model's output produced by the input. The use of variance requires that a random sampling of the parameter space is required, removing localisation to any parameter and emphasising the ability for any of the parameters or interaction between them to provide a result away from their respective mean. This method aims to apportion the variance of the output to each of the input parameters such that the sensitivity indices produced reflect the amount of change seen in the variance. Importantly, GSA doesn't provide the optimum conditions for our model, instead it shows us the impact of each input.

We must ensure that all of the parameters in use are independent, for this we group together γ and P as these parameters are used together in the model to define the strength of the nonlinear interaction. Next we group together the clock period and the detector reset time as a ratio between their lengths as $\tau_{\text{clock}}/\tau_{\text{detector}}$. As the GSA method doesn't define a series of optimal values, we can instead reduce the model to use the difference between the two values. The sensitivity index for the clock ratio then tells us how much faster the clock should operate in comparison to
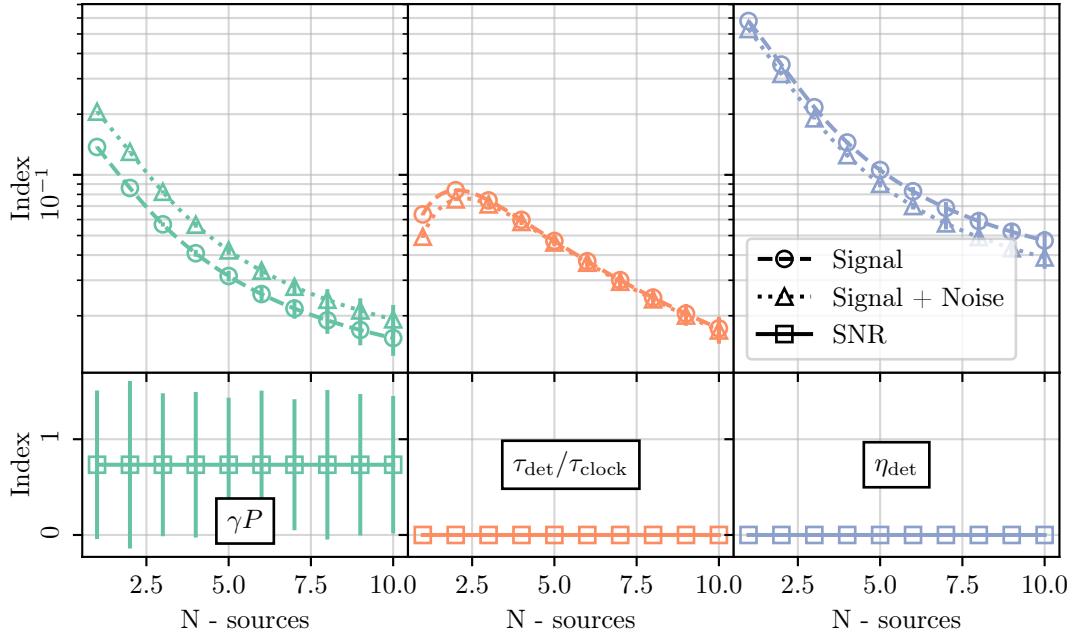
Figure 4.10: **First order Sobol indices with and without the inclusion of higher-order emissions along with signal-to-noise ratio.** The first order sensitivities indicate how changeable the outputs of the model are to corresponding changes in the respective input parameters. We can see that as the number of sources increases the model becomes decreasingly sensitive to changes in single parameters alone. It can also be seen that the signal-to-noise ratio in each instance remains constant, with only parameters relating to the source, "γP", contributing. However it is clear that this is the main contributor for the signal-to-noise behaviour of a number of sources operated in parallel.

the detector speed, giving us insight into whether or not it is beneficial to operate the clock of the laser faster than the detector can reset. The detection efficiency, η is already independent of the other parameters and so can be used directly. Finally, we exclude the number of sources N from the sensitivity analysis instead choosing to apply the entire analysis from a single source up to 10 sources separately so that we can compare how the influence of each of the parameters and their associated interactions vary as we add more sources. We then compute the sensitivity analysis on the signal with and without the effect of higher-order emissions as well as the signal-to-noise ratio. The resulting indices are accompanied with a confidence interval calculated at 95% allowing us to visualise how close the process used to calculate the sensitivities is to the true mean sensitivity for each parameter or interaction.

The first order sensitivity indices for all sources and each of the cases can be seen in fig. 4.10 with figs. 4.11 and 4.12 displaying the second-order and total-
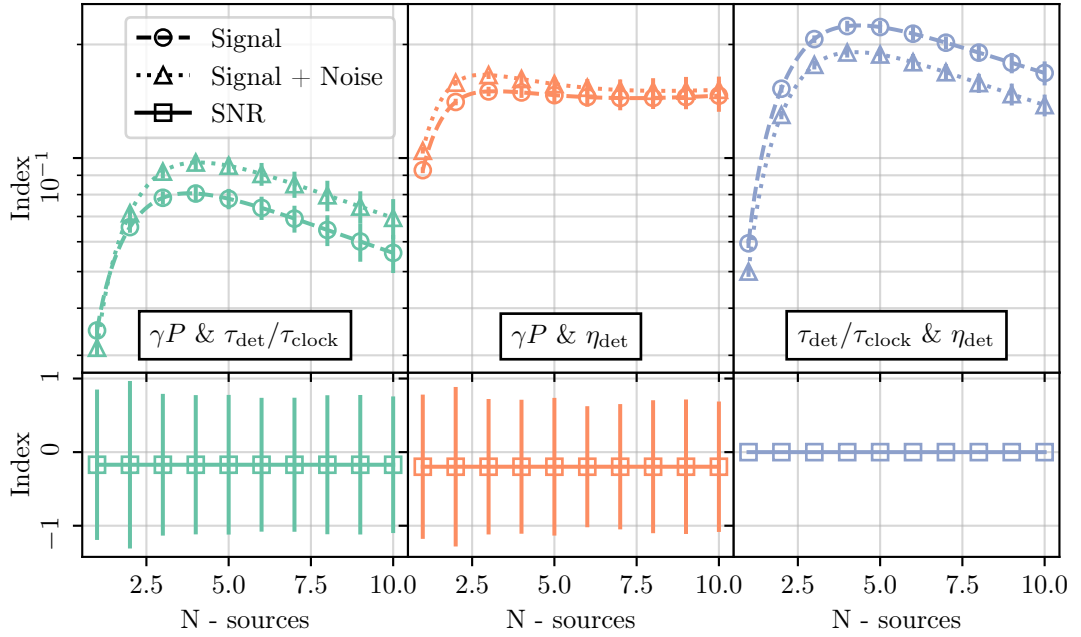
Figure 4.11: **The second-order sensitivities detail the interactions present between each of the parameters.** Detection efficiency, η_{det} interacts strongly with both γP and $\tau_{\mathrm{det}}/\tau_{\mathrm{clock}}$. From these interaction the benefit of increased detection efficiency can be clearly seen, and whilst it this does lead to an increased detection of higher order emissions the signal-to-noise ratio is unaffected. However when considering the ratio between clock period and reset time it begins to become clear that we should prioritise operating our sources with a lower γP to operate at an ideal signal-to-noise ratio and then tuning the detection efficiency, clock period and reset time to operate with as high a detection rate as possible.

order indices respectively. Each column of figs. 4.10 to 4.12 displays the resulting sensitivity indices for each of the parameters, with count rates and signal-to-noise results plotted in the top and bottom panels separately. For ease of comparison, indices for count rates are all plotted with the same y-axis and signal-to-noise results share their own y-axis.

The count rates results (represented by the *Signal* and *Signal + Noise* curves in figs. 4.10 to 4.12) unsurprisingly have correlations with all of the inputs and interactions between inputs and from this we can begin to see trends as to which parameters and interactions benefit the pure signal more so than the noisy signal. From intuition we know that increasing any of the parameters (reducing in the case of τ_{Detector}) should lead to increase in the detection rates up to the point the detectors saturate, i.e when the emission rate is greater than or equal to $1/\tau_{\mathrm{Detector}}$. Further we see that parameters and interactions that include γ and P display a
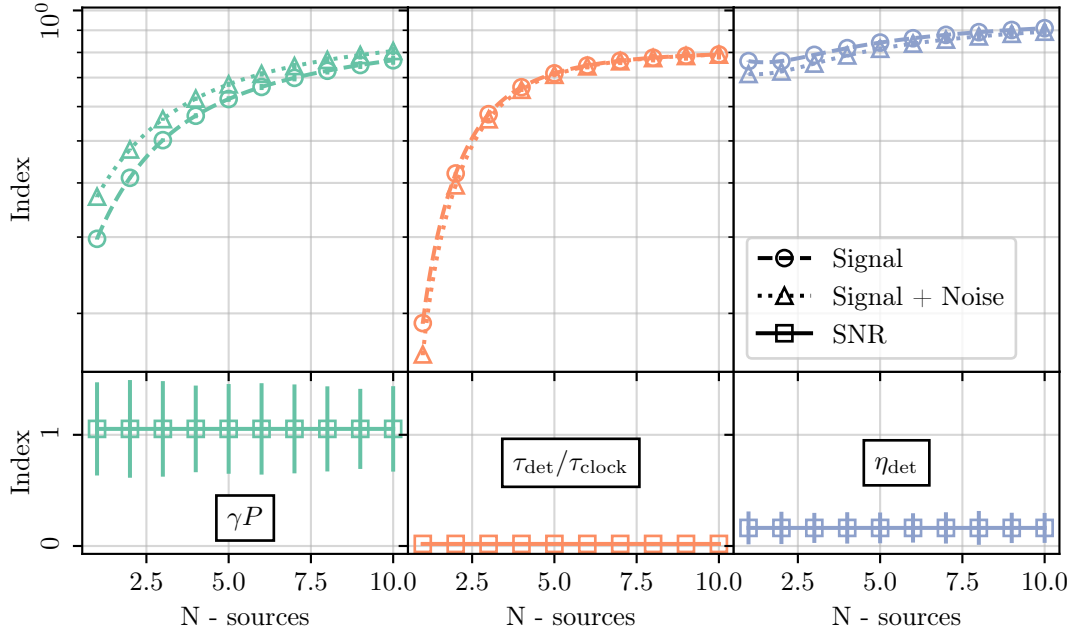
Figure 4.12: **Total-order sensitivities from a single source up to 10 operated in parallel.** Complementing figs. 4.10 and 4.11, the indices here encompass all the contributions from each parameter and their associated interactions with each other. From the curves seen here we see that as the number of sources is increased each of the parameters becomes increasingly sensitive to each of the input parameters.

greater sensitivity for the noisy signal more than the pure signal, when we consider the equation for the PDC state eq. (2.3) where $\lambda^2 = \gamma P$ any increase here will result in more of the higher-order terms being detectable. This reflects the signal-to-noise characteristics we typically observe. This analysis also emphasises the correlation between detection efficiency and detected rates. What is perhaps not immediately obvious when considering the model in isolation is that the pure signal exhibits greater sensitivity to detection efficiency than noisy signal output. If we now consider that the timing ratio between the detectors and the clock speed of the pump laser does not display a strong difference in sensitivity to either the pure or noisy signal we can infer that changes in this ratio do benefit the detected rates, what it does not tell us however is whether this ratio should be maximised or minimised. Fortunately fig. 4.3 tells us that for low values of γP we should seek to maximise this ratio and as its value increases we should instead choose to minimise the ratio.

Turning our attention now to the signal-to-noise ratio results between first, second and total-orders, figs. 4.10 to 4.12, we again have our intuition confirmed in
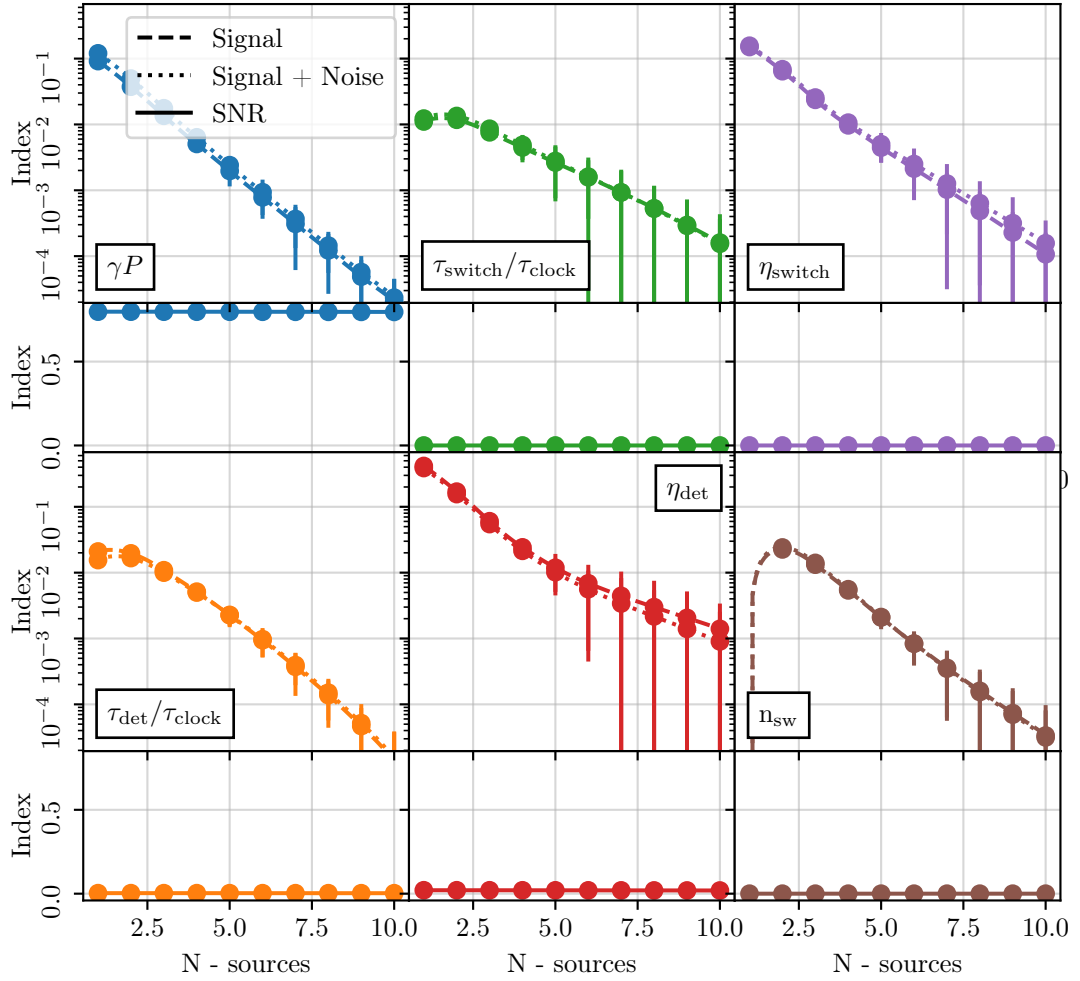
Figure 4.13: **First order sensitivity for relative temporally multiplexed PDC sources.** Similar behaviour as with an array of sources without multiplexing (fig. 4.10) can be seen here. In both cases the γP parameter provides the largest contribution to the signal-to-noise ratio. In contrast to the previous model we also include a parameter to control the number of time bins per clock cycle, whilst this parameter allows us to increase the probability per clock cycle of the experiment when it comes to overall detection rates we see a decreasing correlation with the output of the model.

that the γP term and its related interactions provide the strongest correlations with the model's output, with only a small correlation present in the total-order results for detection efficiency. Whilst it seems obvious that terms related to the strength of the nonlinear interaction in the PDC state should affect the signal-to-noise ratio, the fact that the clock speed and detector reset times have no correlation and that they and the signal-to-noise ratio output from the model are independent of each other furthers our confidence in the model. The sensitivity indices for these results can already be inferred from the pure and noisy signal sensitivities as the noisy

signal sensitivity is always stronger than that of the pure signal. In turn the signal-to-noise sensitivities displayed here show that as the number of sources increases, the γP term has an increasingly stronger effect in both the pure and noisy signals as well as effecting the signal-to-noise ratio sensitivity the most. This means that signal-to-noise ratio performance must be equally sensitive across all cases.
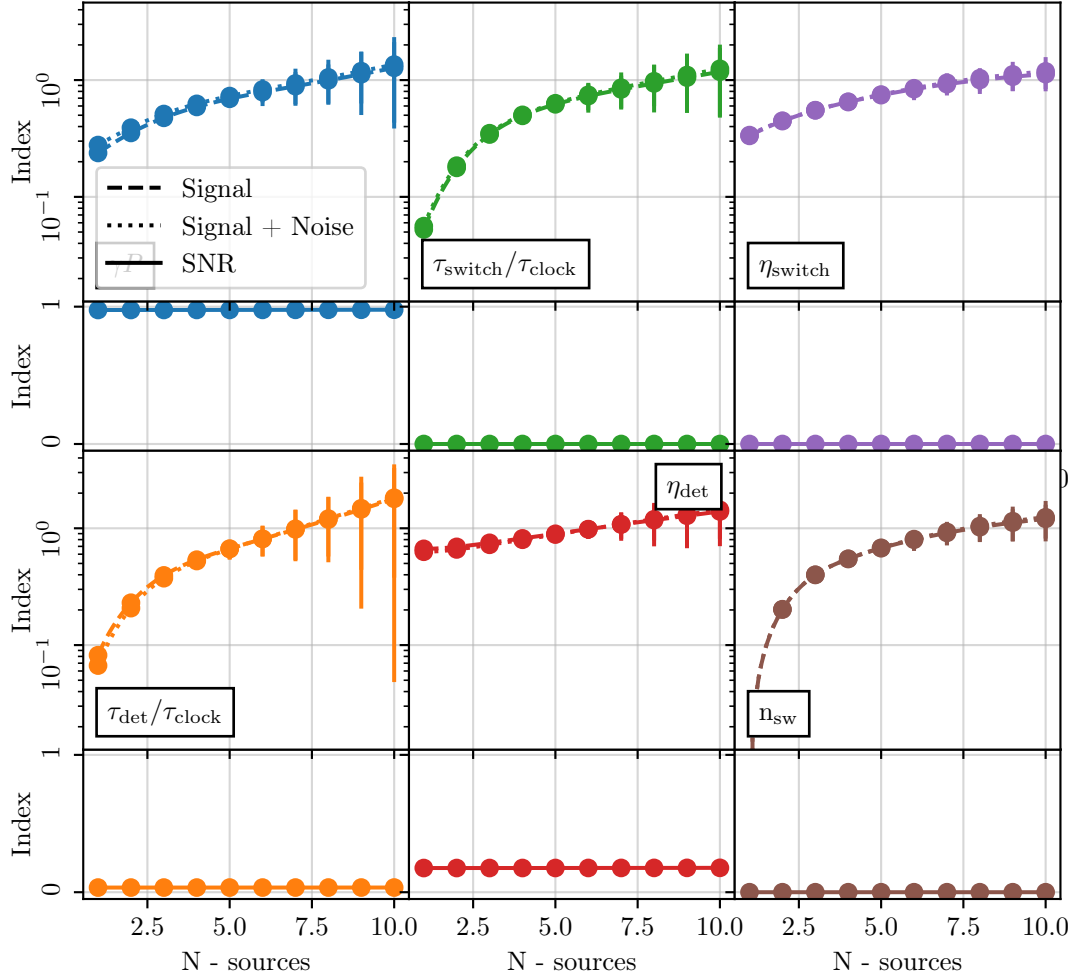
Figure 4.14: **Total-order indices for the relative temporal multiplexed single photon sources.** As with the results shown in figs. 4.10 to 4.12 for an array of sources without multiplexing we see similar behaviour when considering the case with temporal multiplexing. However we see less dependency on power with a greater influence coming from the timing effects between the clock speed and switch or detector reset times. Further, the n_{sw} parameter defining the number of switches used in the scheme, and so the number of time bins per clock cycle, becomes a key factor in determining the effectiveness of implementing the temporal multiplexing scheme. The difference in sensitivity between the efficiencies for the switches or detectors when compared to that of their rest times with respect to the clock speed points towards the importance of increasing the clock rate regardless of reset times to achieve higher detection rates.

These results lead us to the conclusion that in order to maximise the detection rates and signal-to-noise ratio we should set a target γP that corresponds to a suitable signal-to-noise ratio for our application, use as high efficiency detectors as possible and then increase the clock speed in comparison to the detector reset time. Under these conditions we ensure a high enough signal-to-noise ratio and target the fastest detection rates possible for our detectors.

Having completed the analysis for a series a sources operated in parallel as would typically be the case when using PDC sources to build multi-photon states we now move the focus of the analysis to the standard and relative multiplexing schemes presented by Zhang *et-al.* [139]. For this, the analysis must be extended to include the switch efficiency/loss with η_{switch} and a second timing ratio between the clock speed and the switch reset time. The number of time bins per clock cycle is also included. Building again on the combinatorial model in chapter 3 to include the effects of switching, we can calculate estimates for the signal, signal with higher-order emissions as well as the signal-to-noise ratio. Before continuing with the results here, the GSA for only the "RTM2" scheme will be detailed here, this is because the model derived to analyse them differs only by a scaling factor and so each responds to GSA in the same way the result of which is that the sensitivity indices are identical across each multiplexing scheme. The range of sources the Sobol method has been applied to has been reduced to ignore a single source as these temporal multiplexing methods require multiple sources to operate.

We can see from figs. 4.13 to 4.15 the sensitivity indices for these temporal multiplexing schemes exhibit much of the same behaviour as a number of sources operated in parallel. In comparing the results between each of the schemes we have applied the Sobol method to, we see consistent sensitivity between each of the parameters of the respective models. Now considering the effects present it furthers our claim that we should operate at a target γP with a suitable signal-to-noise ratio and proceed to tune the ratio found between the clock and detectors or switches along with choosing to use detectors that, unsurprisingly, operate with high detection efficiency.

4.6   Discussion

Here we have evaluated the multi-photon generation behaviour of an array of single photon sources with and without the addition of temporal multiplexing. Further the multiplexing schemes explored each have their own merits, the requirement of high performance detection and switching proves to be the deciding factor for practical implementations. In order to provide an answer as to whether running an experiment faster or slower than the detectors we can turn to the results presented both locally on specific parameters as well as from our global sensitivity analysis. In global terms we see that we should try to maximise the signal-to-noise ratio by operating at a target γP paired with high efficiency detectors. From our localised analysis we can then see that dependent on whether or not we operate with a large γP term we should then run the detectors and experiment clock at the same speed turning to run the clock faster for smaller γP.

It is still commonly held as true that increasing the clock speed of the experiment is limited by the detector performance [142]. However, we have shown that in the presence of loss, it is beneficial to run the clock much faster than the maximum detection rate. For many laboratories this is already the case, using a pulsed laser clock to ≈ 80MHz, with a corresponding peak-to-peak time of 12.5ns, in conjunction with detectors taking tens of nanoseconds worth of dead time. However, it would be beneficial to increase the clock speed even further as the emission probability is much less than one for each source. The practical limitation is instead the reduction in maximum pulse power, as each doubling in clock speed comes with a halving of pulse power, which must also be shared amongst beam lines for each source. This power limitation is the reason why in our laboratory we increase from 80MHz to 320MHz, doubling the clock speed twice, as beyond this the power deliverable to each source is too low. We should also consider cases with active switching, like those presented in [139], in the same way, the switches don't need to operate as fast as the clock source, but as fast as the heralding signal.

As would be expected detector parameters (η_{det} and τ_{det}) behave in much the same way for both no multiplexing and relative temporal case with active switching, with the reset time providing an upper bound to what the detector is capable of processing and the efficiency defining how close to that upper bound we should

expect to achieve, it is the switch parameter (η_{switch} and τ_{switch}) that provide the differences between the two schemes, whilst both benefit from as high a performance as possible the multiplexing schemes do appear to be more forgiving in terms of resulting count rates and signal-noise ratio. This more forgiving nature is likely due to addition of a heralding signal helping to co-ordinate the process, on this note it would be interesting to apply a demultiplexing scheme to an SPDC single-photon source in order to make use of a heralding signal to better control the switches. In practical terms, we used the combinatorial model outlined in chapter 3, with validation results, to decide the maximum rate to increase our pumps repetition rate as shown in [65]. Given our experimental parameters, and operating up to 6 photons in our test of local observer independence [1], we found that 320 MHz was the optimal tradeoff between a reasonable N-photon rate and thus integration time, and the signal-to-noise ratio. As a consequence, we've been achieving N-photon benchmarks such as state fidelities which are leading in the field given the complexity of in particular the experiment in [1].
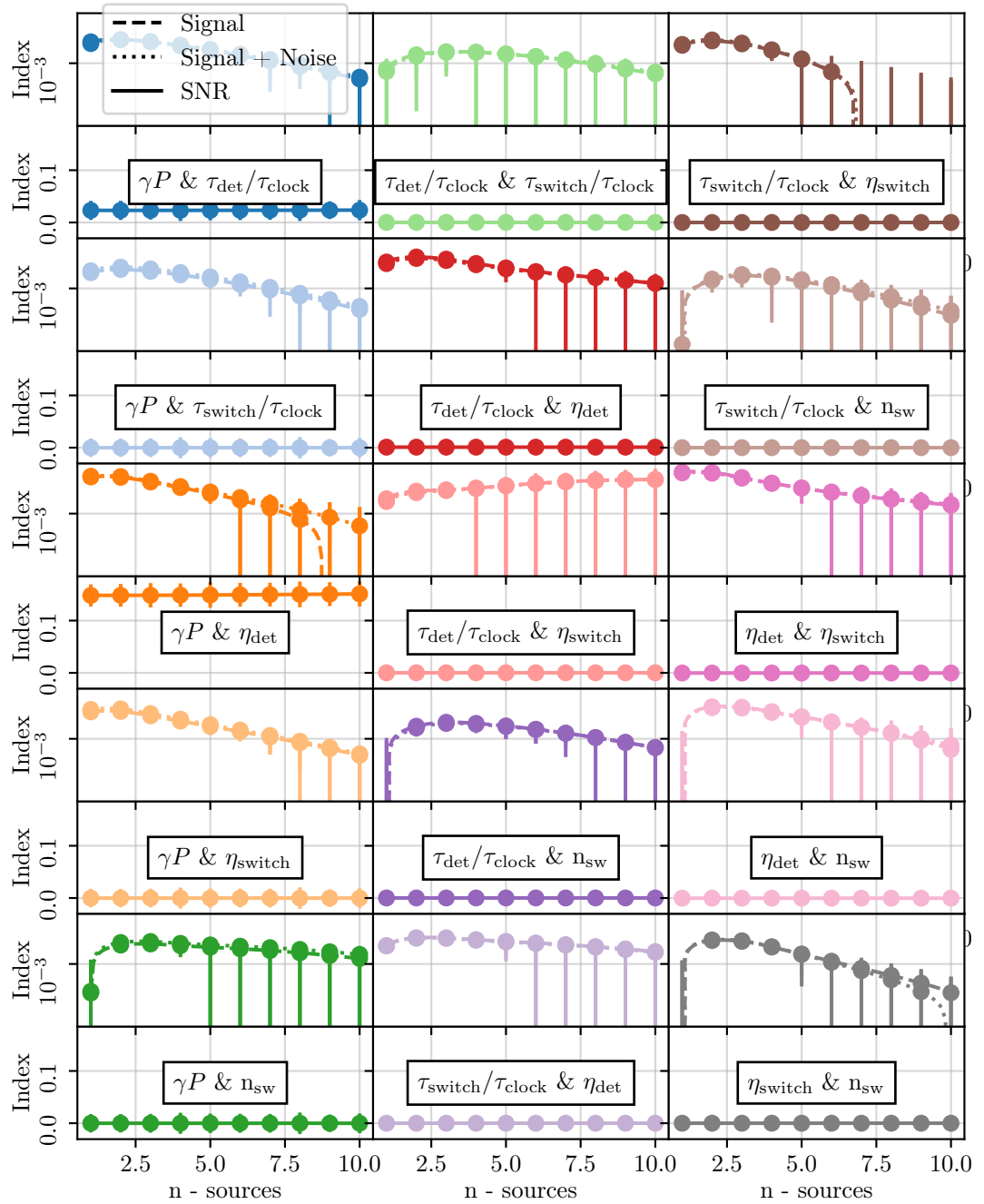
Figure 4.15: **Second-order indices for the relative temporal multiplexed single photon sources.** All of the second-order sensitivities caused by the interactions present between each of the input parameters are displayed here.

Chapter 5

Time-Correlated Single-Photon Counting

In the chapters 3 and 4 we discussed the three building blocks of quantum photonics, sources, interactions, and detection. We then proceeded to model specific source-detection scenarios to help us fine tune the parameters available to us in the lab. We will now move on to the third building block and beyond: the detection of single-photons and the processing of the resulting data patterns. Scaling up multi-photon experiments requires processing increasingly many detector outputs. To discriminate signal from noise, these need to be timed very accurately (on the nanosecond scale or below), to identify detections belonging to the same N-photon emission event. All of this can be achieved either by a series of fast digital circuits, i.e. a series of fast NAND gates, or by use of a fast timer to assign a time tag to each detection event. In both cases (or their combination) the current state-of-the-art is to build a device around field programmable gate arrays (FPGAs)[1] to collect and process the incoming signals from our detectors and implement real-time pattern recognition.

Apart from the need to achieve around nanosecond timing resolution for individual detection channels, pattern recognition requires these channels to be temporally "zeroed" against each other. This used to be achieved with physical delay lines. Modern FPGAs can implement digital delay lines, and time-taggers can be zeroed in software post-processing. For digital logic, the existence of patterns in the stream

---

[1]Use of application specific integrated circuits (ASICs) can provide a further increase in performance as devices capable of only timing or logical tasks however this comes at the cost of flexibility.

of detection events can be found by use of a binary counter between channels signalling the pattern of channels that have been triggered. Further, the application of fixed offsets (of the size of the device's timing resolution) allows for delays present in the experimental setup to be accounted for. For time tags we instead assign the detection event two separate values, the first being which channel has been triggered and the second being the time at which the trigger occurred, these two values are then typically encoded into a single value: the time tag. Depending on the application one may need to process time tags on the fly, or store them for slower data mining later on. For experiments conducted in our lab like that of the "Experimental quantum conference key agreement" [5] we needed to process all data in real-time to determine when the first event in the sample occurred in order to build the conference key. Conversely, for our reconstruction of the JSI for purity estimation in "Direct Generation of Tailored Pulse-Mode Entanglement" (see [7] and chapter 6) we needed to store all of the time tags for later data mining. Next we detail methods to analyse the produced data. These examples have risen out of the work done in section 5.2 allowing for task specific analysis to be developed to help facilitate the groups experiments.
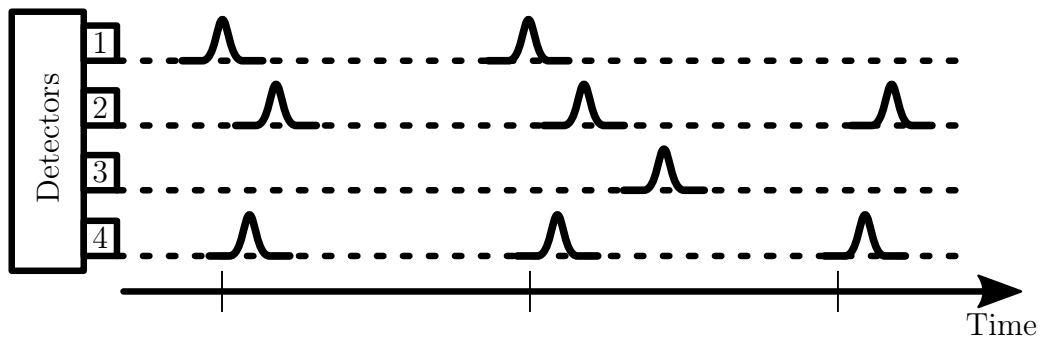

Figure 5.1: **Time-correlated single-photon counting.** In TCSPC we record a time stamp for each single photon detection event. From each of these time stamps we can determine the instances where all of the sources in our experimental scheme emitted photons at the same time.

5.1 Timing Logic

Even the most accurate measurement devices are not without their flaws and limitations. The time tagging and logic devices discussed in this chapter are no exception. The timing element present in both cases is subject to some degree of jitter from both the internal clock as well as the quality of the components used when creating a trigger signal. Whilst different methods exist to discriminate the arrival of a signal none of them are free from jitter. Further the amount of data that can be processed is limited, either because of the bottleneck in the communication from the device to post-processing, or due to internal processing speeds, i.e. internal counters needing to reset.

Here we will outline the behaviour and limitations of the pulse detection method commonly employed in TCSPC devices to provide some detail on an item often taken to be "as is" in a laboratory setting. The main exposure to the operating method of these TCSPC devices is the setting of each channel's threshold levels and retrieving data from them. In this section we will first provide an overview of how the pulse is detected and in a later section provide details on how to find useful information within the retrieved data.

5.1.1 Constant-Fraction Discrimination

To determine whether or not a pulse has arrived at our timing logic naively we may decide on a simple rule: if the voltage on this channel is greater than my threshold I will mark that as the arrival time of a new event. This however is much too simple, under this ruling we are too much at the mercy of incoming signals jitter along its rising edge. The jitter here is a feature of the slight random variations present in the amplitude of the output pulse of the detector. The effect of these variations in the signal amplitude can be seen in fig. 5.2, the use of a fixed threshold value to trigger the arrival of the detector signal leads to a range of times the signal might have arrived, reduction of this time range allows for higher precision measurements to be accessed. In order to compensate for the increased jitter present in edge-only triggering we instead make use of constant-fraction discrimination (CFD). This process can be broken down into the following steps (the result of each step can be
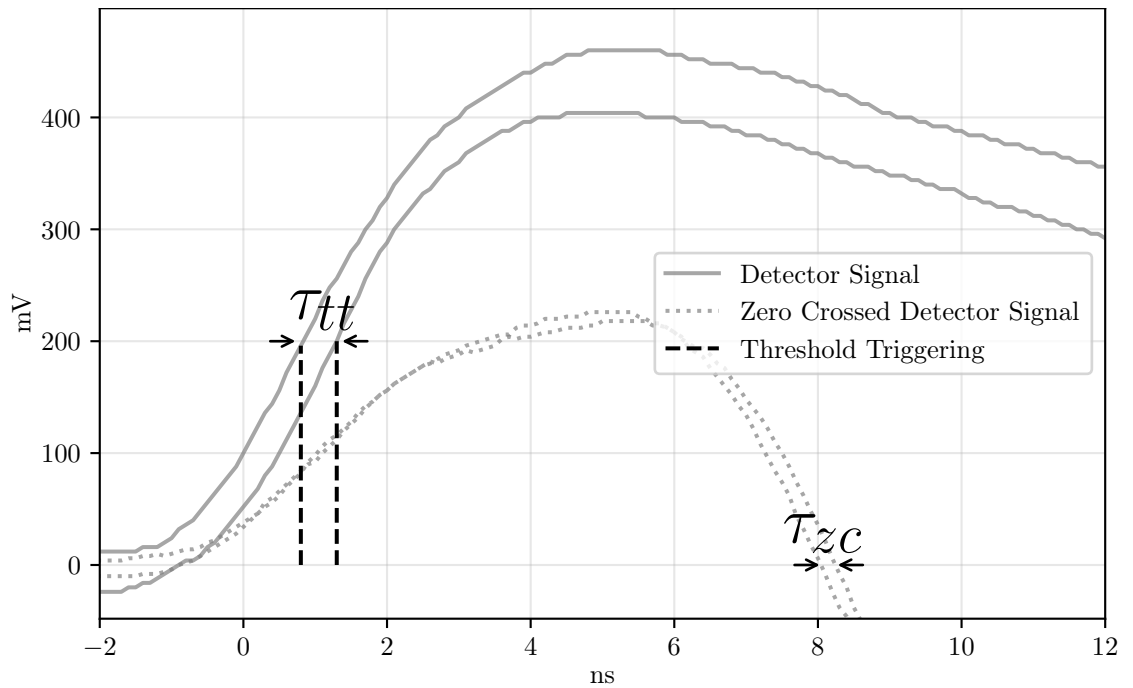
Figure 5.2: **Induced timing jitter between different triggering methods.** Using a pulse from our detectors (Quantum Opus SNSPD) as an example, fig. 3.2, we can see the effects of jitter when using just threshold triggering or zero-cross triggering, from this it is clear to see that the jitter involved when using zero-crossing is less than for thresholding ($\tau_{tt} > \tau_{zc}$). Whilst zero-crossing is in theory capable of introducing no jitter to the measurement is primary goal is to negate the effects of different signal amplitudes. There is also a need to contend with the variation in the signal pulses rise time.

seen in figs. 5.3 and 5.4);

1. The pulse arrives at our timing logic as our input (fig. 5.3 (1))

2. We produce two copies, the first is attenuated, the second is delayed and inverted (fig. 5.3 (2 & 3))

3. The attenuated and delayed copies are summed (fig. 5.3 (4))

4. A voltage comparator is then used to identify the zero-crossing point of the summed signal to provide us with just one rising and falling edge (fig. 5.3 (5))

5. In parallel to this the input signal is compared against a threshold voltage (fig. 5.3 (6)), we still require edge triggering here as otherwise the zero-crossed signal could produce a timing event for small fluctuations in the noise floor.
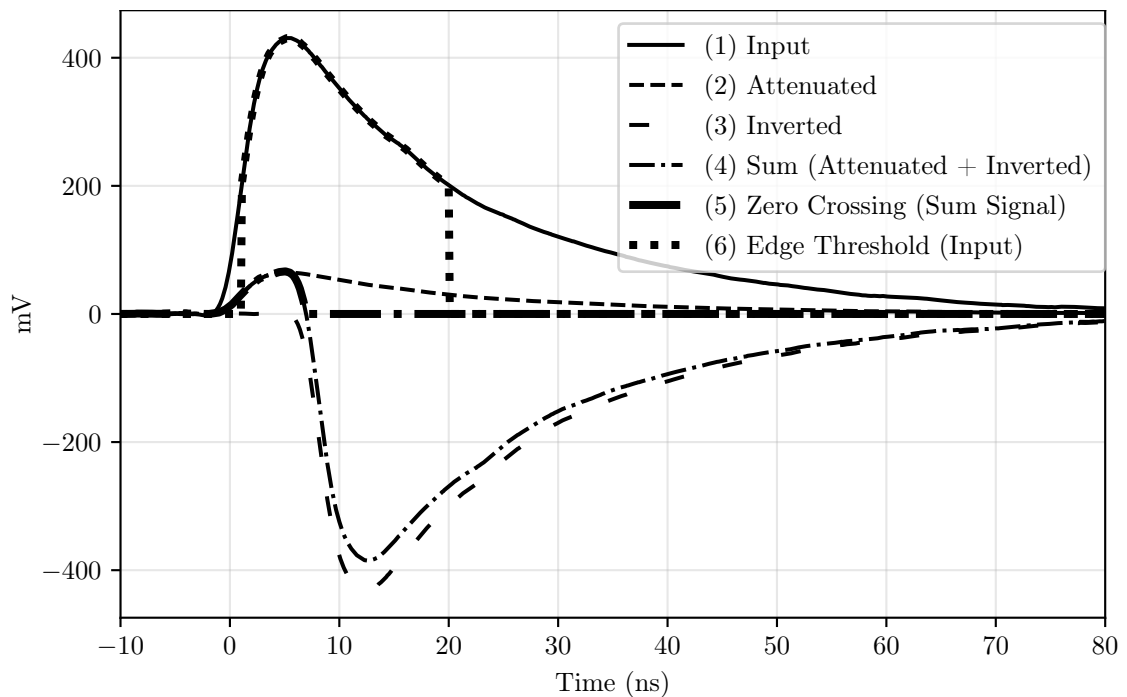
Figure 5.3: **Constant-fraction discrimination process.** The trace shown here is from a Quantum Opus SNSPD (see fig. 3.2 for performance). Moving through steps $1 \to 6$ we see how creation of the zero-crossing signal and edge thresholding combine to provide us with square rising and falling edges in (6).

6. Finally, the zero-crossing signal and edge-triggered signal are fed into the clock and reset input of a D-flip-flop[2] respectively, with D's input set to high. The result of which can be seen in fig. 5.4.

The rising edge of the zero-crossing signal activates the flip-flop and if the edge triggering signal is also set to high we proceed to sample from the D input, this results in the square pulse seen in the lower panel of fig. 5.4 (noting that the falling edge of the zero-crossing signal deactivates the flip-flop).

5.1.2 Arrival Times of Detector Pulses

Once it has been determined whether or not a pulse has arrived and produced a signal more suitable for further processing by our logic we must now find a method to determine when that signal arrived. Two key methods have been developed in order to do this, the first being the use of a time-to-analogue converter paired with an analogue-to-digital converter, such a device takes an input and produces an

---

[2]The D-flip-flop differs from the standard flip-flop in that the single bit of data it stores is captured from the D input of the device rather than the state of the gate.
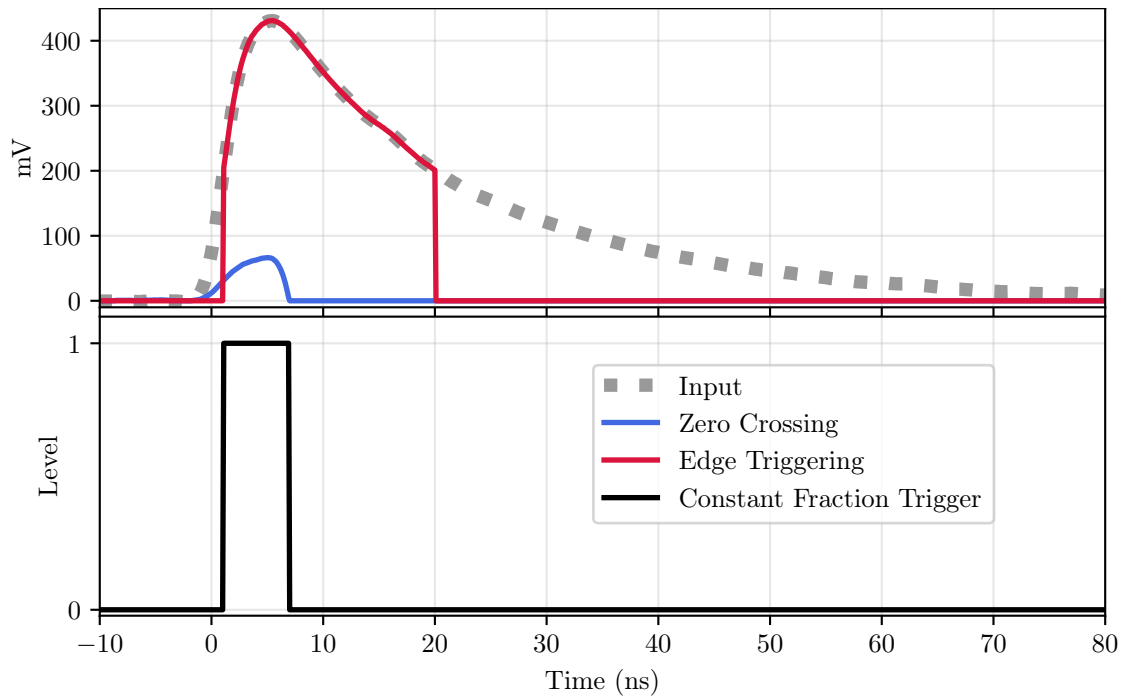
Figure 5.4: **Comparison between output of edge triggering and constant fraction-discrimination based triggering.** Extending from fig. 5.3 the two waveforms produced by the two discrimination processes shows how zero-crossing allows us to create a short control signal and the use of an additional level thresholding provides a convenient means to distance ourselves from the noise floor.

analogue signal before digitising it for use by a host computer whereas the second method, developed as a successor, takes the initial signal and immediately produces a digitised representation. On the surface these methods appear the same however being able to convert an analogue signal immediately into timing information reduces jitters as we have removed a processing step.

Time-to-Analogue Converters + Analogue-to-Digital Conversion (TAC/ADC)

The first component required for the TAC/ADC method is the TAC, this is a conceptually simple device however its complexity is revealed upon implementation. Its purpose is to linearly increase a voltage over a predefined range between the arrival of a start signal and a subsequent stop signal. The general operating principle is as follows;

1. The control signal arrives from the discriminators

2. Begin charging the capacitor bank

3. The stop signal arrives (either a clock signal or secondary signal to the discriminators)

4. Stop charging the capacitor bank

5. The voltage across the capacitor bank is read out

6. The capacitors are discharged so that they are ready for the next control signal.

This architecture has some key limitations, the first being the use of capacitors to measure the length of time present between two signals, due to their charging (discharging) behaviour not being completely linear they introduce some jitter into the timing measurement. The second limitation is the need for a wait phase such that we can reset the capacitor bank, in the case of very high speed signals this will limit how quickly we can process incoming signals as we must concede that any signal that arrives during the charging and reset phases have to be discarded. The read-out phase of the process is completed by the ADC to produce a binary representation of the ramped up voltage. In order to gain a full representation of the photon arrival time we may wish for the read-out phase to consist of both coarse and fine timing values, for example having the coarse value being the total number of internal clock ticks since the timing device was started with the fine timing value being reserved for the amount of time the incoming signal is away from its proceeding clock tick. Further we may also want to include a signal as to whether or not the maximum coarse time has been reached, at which point we will reset back to zero (this helps with maintaining constant timing on a host computer). It should be noted here that whilst this method is no longer considered to be the state-of-the-art it is has been a successful method for a considerable amount of time. However with the advent of high bit-depth digital components and the advent of FPGAs and application specific integrated circuits (ASICs) the development of entirely digital solutions has progressed significantly.

Time-to-Digital Converters (TDC)

This brings us conveniently to TDC based implementations, here we make further use of the idea of separate coarse and fine grained timings however both follow
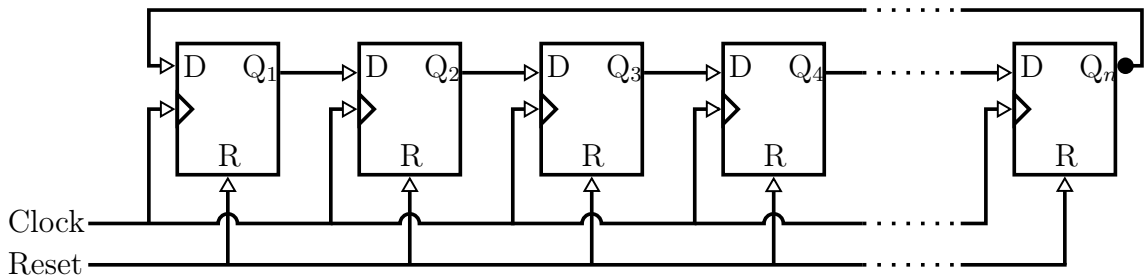
Figure 5.5: **The Johnson counter.** Constructed from a series of D-flip-flops all using the same clock input with each output chained to the successive "Data" input. By constructing as a ring by connecting an inverted copy of the output of the final gate into the data input of the first gate a constant stream of zeros followed by ones is produced. Sampling the stream of ones and zeros determines the value of the counter.

similar architectures unlike that of the TAC/ADC approach. First we will consider the requirements and implementation for the coarse timing, which may be enough for slower signals (where the distance from signal to signal could be as close as 1 ns). In the world of quantum photonics, gigahertz clock rates would be considered fast (except for some limited quantum key distribution applications). The timing accuracy would therefore have to be around the order of nanoseconds, which can be considered slow for state-of-the-art timing devices. Applications like fluorescence lifetime imaging, but also remote sensing applications like LIDAR and depth imaging require much faster speeds for high resolution measurements, down to picoseconds. Up to incoming signal rates of 1 GHz (1 ns resolution) it can be sufficient to measure time with a counter alone.

Essentially, a pair of counters can be used together, one coarse, one fine, allowing for accurate timing of events with small or large timing differences. Conventional oscillators and integrated circuit electronics can be used for coarse-grained timing, e.g. standard 10 MHz oscillators are used typically used to define a stable system clock for the device. The clock ticks they provide are spaced at 100 ns, and the Johnson counter can be used in combination to allow for timing resolution down to 1 ns. Going beyond that into the picosecond regime is more complicated, now fine-grained counters are added that rely on principles like the tapped delay lines. Here a start and stop signal are needed, provided by the detection signal and the fast effective clock signal respectively, the point in the tapped delay line where the stop signal catches up with the start signal sets the state of the circuit, which is
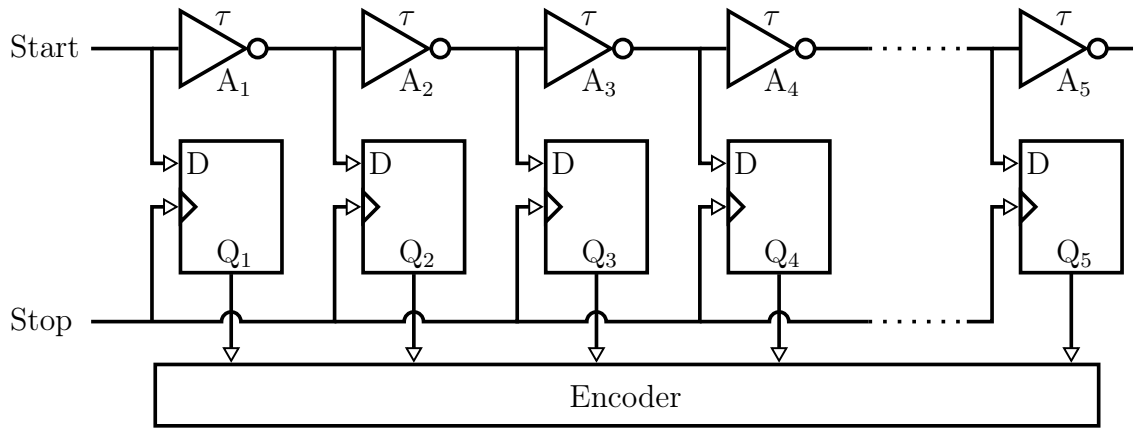
Figure 5.6: **The schematic for a tapped delay.** For fine grained timing a series of D-flip-flops are again used. Here each of the outputs are connected to an encoder, along with the value produced from the coarse timing circuity. The data inputs are connected to the start signal input and delays are placed in between each flip-flop, as a result the start signal is incrementally slowed down until the stop signal catches up with it.

then read out.

For the tapped delay line the read-out is a one-hot code[3] where the value is set by the gate in the delay line where the stop pulse caught up with the start pulse so we know that the fine timing must be related to the number of gates crossed and the length of the delay, i.e. $T_{\text{fine}} = N_{\text{gates}} \times \tau_{delay}$

The Vernier principle can be applied to the tapped delay line to increase timing resolution by having a pair of different delays (one each for the start and stop signals). The additional delay line means that now the time recorded is $T_{\text{fine}} = N_{\text{gates}} \times \left(\tau_{delay_{\text{start}}} - \tau_{delay_{\text{stop}}} \right)$

Combing both coarse and fine timing methods as discussed here lends itself naturally an encoding scheme as follows for 32-bit timing information[4];

1. Bit 0 to signify resetting of the internal clock so that we know to add a multiple (dependent on how many times we see a 1 here) of a fixed value to make all time tags continuous

---

[3]These codes compared to counting in binary can only count up to the total number of elements they are constructed from rather than exponential growth seen in binary codes. As a result these codes gain simplicity in how to correct errors present in them due to the limitation of only allowing a single high bit at a time, for example the encoder on the output could be made to ensure that the value of each gate progresses in a linear order allowing us to know that if two bits are high which one is correct.

[4] This is the same encoding used by Picoquant for their HydraHarp (firmware >2).PTU files
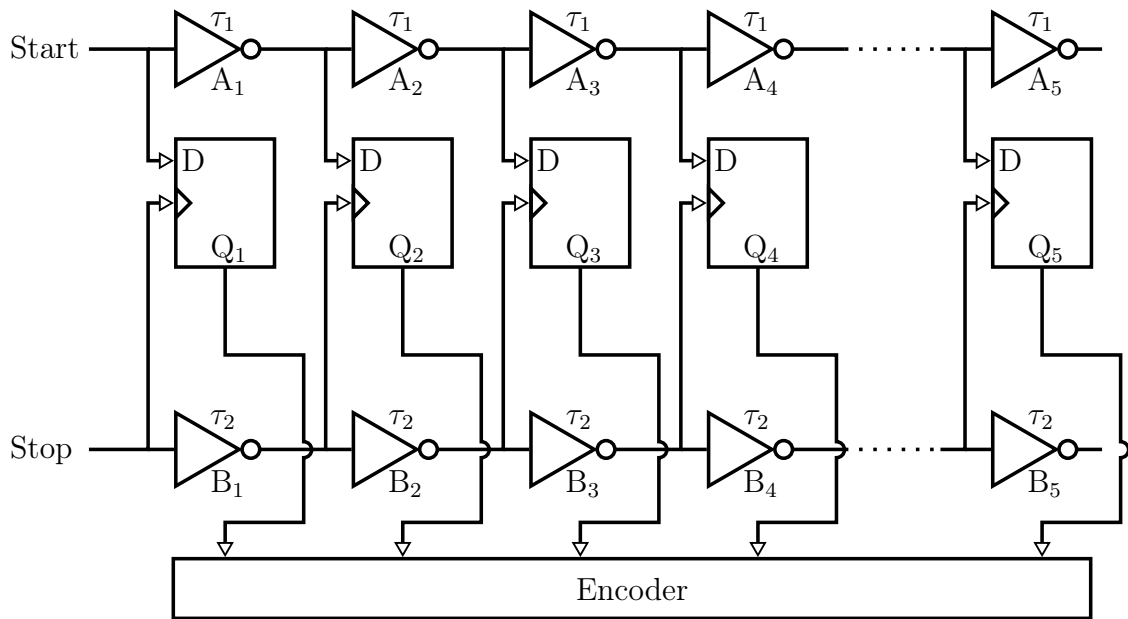
Figure 5.7: **Vernier method timing for a tapped delay line.** By extending the structure in fig. 5.6 with a second array of delays for the stop signals the timing resolution can be increased further. The delays must obey $\tau_1 > \tau_2$ so that the stop pulse will still catch up with the start pulse.

2. Bit 1 $\rightarrow$ bit 6 to represent the channel of the device

3. Bit 7 $\rightarrow$ bit 31 to store the timing information.

Fine timing is defined by a series of delayed logic gates acting like a register, defining how many bits the fine timing must occupy, we can choose (should we have a method to signify resetting of the clock) to use a relatively small number of bits for the coarse timing compared to the fine timing. In doing so the required bandwidth per time tag can be reduced whilst maintaining as much timing resolution as possible.

Whilst this fully digital approach may allow for higher resolution timing measurements to be made it is still susceptible to errors and drifts. The most prominent cause of these in the coarse timing have been identified as the resistance and capacitances present in the circuits, these problems manifest themselves through a slightly different method in fine timing however. Here the causes of errors are due to slight variations in the temperature of the components and circuitry as well as slight changes in their supply voltage, when considering the degree of accuracy targeted these small fluctuations are not to be taken lightly, especially in applications

of the Vernier method. A method to stabilise the circuit is required such that any change in the characteristics of the circuit affects both delay lines by equal proportions so that timing can be maintained, for this a Delay Locked Loop (DLL) is implemented to ensure that both delays result in pulses exiting the circuit simultaneously. Conversely, for the simpler tapped delay line to counter these problems we would instead use a PLL to stabilise for temperature and voltage fluctuations.

With an overview of how the timing logic works in a general sense and more specifically for use in time tagging, we can now explore how we should go about analysing the data produced.

5.2   Counting Methods

Moving on, we now consider the software we need to complement the hardware. The software aspect of TCSPC needs to find patterns within the stream of data read-out from the timing logic, these patterns are the coincidence events of the multi-photon events of our experiment. We state that 2 detector channels are in coincidence with each other if they arrive at the detectors at the same time within a user defined window. In a laboratory environment we often find that our photons arrive at our detectors at different times due to mismatches in the lengths of fibres used to couple our photons into them, as a result we extend this definition to those channels being in coincidence after applying a delay numerically to the time tags produced. As a result we arrive in a position where in order to determine whether or not a coincidence event has been found we must look at (often distant) points in time along our stream of time tags. Further we define a multi-coincidence event as a coincidence pattern across more than 2 detector channels.

The software developed here is an extension of the TTag project developed by the Kwiat Quantum Information Group [143]. Our extension is written in Cython (a Python like compiled language) providing fast execution speeds and fast integration of new features tailored to experiments. These features include finding the first instances of a coincidence pattern needed for a quantum key distribution protocol as well as the ability to reconstruct spectra. Further we implemented these methods for both an AIT Time Tagging module and a Picoquant Hydraharp as well as our

extensions to the methods for a UQDevices Logic-16 (the primary tcspc module used with our laboratory).
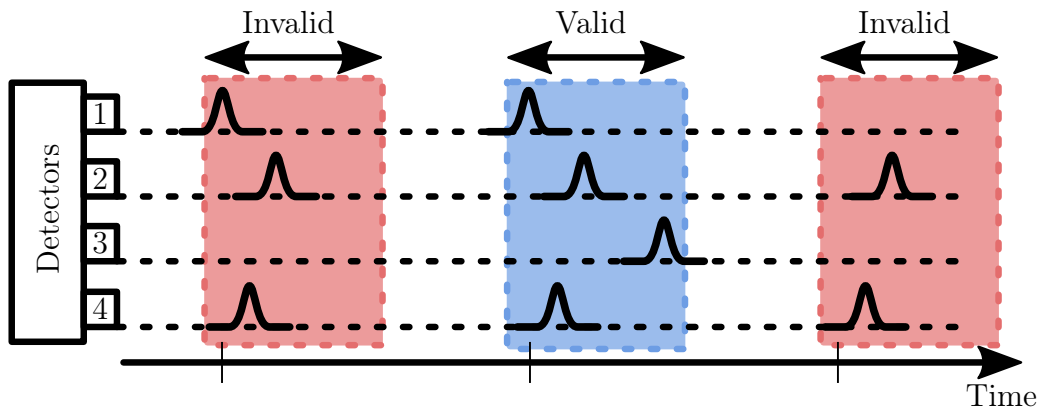
Figure 5.8: **Schematic view of coincidence events.** When looking for coincidence events in the recorded stream of photon arrival times we look for instances in the event stream where all channels appear within the coincidence window, the bound area. In each of the time intervals here only the central interval describes a successful coincidence, neither of the outer two events have all events for all of the channels needed.

5.2.1 Basic Functions

For the software needed to begin analysing the stream of time tags produced by the timing hardware we will outline a series of basic functions that can be used to build up other functionality we need such as finding coincidence patterns that have been recorded. These methods and the full multicoincidence described later in this section have been implemented for and tested on an AIT TTM-8000 (unfortunately now discontinued), a UQDevices Logic-16, and a Picoquant Hydraharp. We assume here that the produced time tag stream is being held within a first-in-first-out (FIFO) buffer and so if we want to gain insight into what happened over the last second (or however long a time period we want to measure) in our experiment we will have to determine how far back through the buffer to search.

Time Conversion

Each time tag consists of at least 2 components, the detector channel and the timing information. We know that the value of the timing information must also be an

integer number of the resolution the timing hardware is configured to operate with. For convenience we should be able to convert between this and real time.

Converting from Time Bins to Buffer Positions

We can assume that it would be likely that not all time tags follow the last by exactly one time bin and depending on timing resolution, emission (detection) probability and the clock rate of the experiment the distance between neighbouring time tags is not constant, however we need to operate as fast as possible to ensure that we can differentiate between neighbouring time bins (acknowledging that in high loss applications this distance might be as low as $1/R_{\text{Dark Counts}}$). This leads us to needing to be able to convert an amount of time to a corresponding position along the buffer. This is a key function in determining the point along the buffer we should start counting from as we want to find the oldest time tag in the buffer for the channel we wish to analyse. Using that as the point to start counting from up to the time tag at the start of the buffer where we started our analysis.

Next Buffer Position for Current Channel

Once we have our starting point and have visited a buffer location to perform some analysis we then need to find the next position along the buffer with a newer time tag for the current channel we are investigating.

The Oldest Channel

Finally for these basic building block functions we also need to store the identity of the channel with the oldest time tag. This is especially necessary when it comes to searching for coincidence patterns as we can use this to determine which channel index to increment next so that we can progress through the buffer and complete the calculation for a given time frame.

5.2.2 Singles Photon Counting

If we have a number of detector channels one of the simplest measurements we can perform on the buffer is to determine how many times a specific detector channel has produced a time tag either since the start of the experiment or over a set time

frame. This tells us the detection rate at the detector and with that we can make an estimate as to the dark count rate if we record a sample of noise from the detectors with no signal entering them. The term "Single (s)" here is a short hand to refer to the rate produced by only 1 detector. In order to calculate the singles rate we need to;

1. Determine how far back in the buffer we need to position ourselves and set that as our start point.

2. Validate whether the time tag at that point in the buffer is for the channel we have targeted.

3. Begin to move along the buffer up to the most recent tag, stopping at the first position we find our target channel.

5.2.3 Multicoincidence Event Counting

This conveniently brings us to finding patterns of channels within the buffer. We refer to these patterns as coincidence events and we must acknowledge that there are differences in the arrival times of each the photons for each detector channel, meaning that the pattern of detection events we are looking for might not happen simultaneously but accounting for the offsets present we can analyse photons produced by the same generation process. The method for finding these events is more involved than those for single detector events and so we must be careful when initialising where to count from as relative delays between each channel must be accounted for. Further it is possible for the buffer to contain the same timing information multiple times in adjacent positions for different channels, as a result we must ensure the timing value we are inspecting is for the channel we expect. Here we detail a generalised prescription for finding coincidence events between a set of detector channels we define as our measurement. From the following details it should be possible to define a method/function for any chosen programming language. The key steps are detailed in the following flow chart such that the structure is more clear for anyone wishing to implement multicoincidence detection methods into their own analysis library in fig. 5.9.
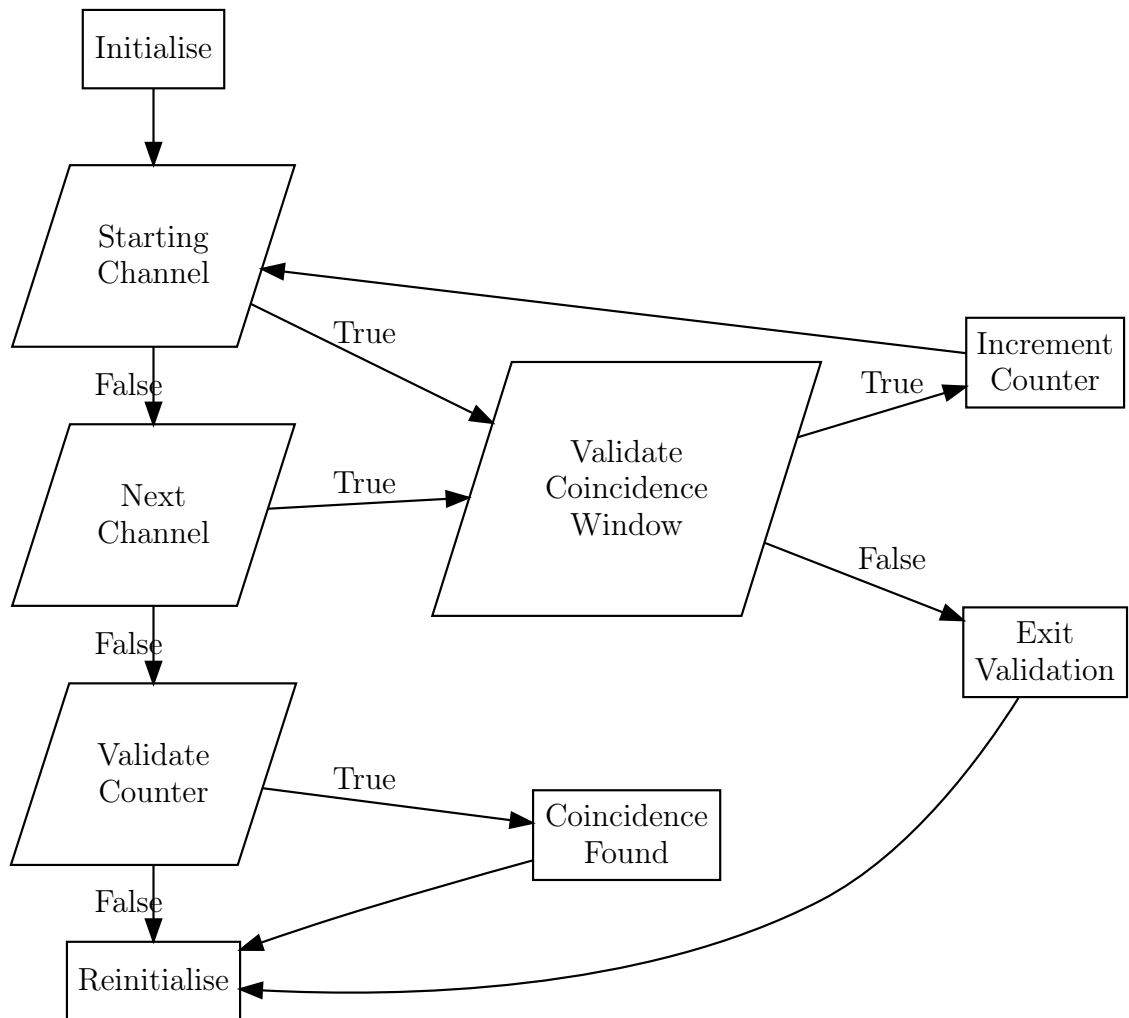
Figure 5.9: **programming flow chart for detecting coincidence events within a stream of time tags.**

Initialise

To initialise the counting process we must

1. First find how far back to start counting from in the buffer according to how large a time period we are measuring over

2. Convert our delays and coincidence window into time bins

3. Find the buffer position for each channel in the pattern closest to the start point defined first but not older than this point

4. Now we ensure that the per channel buffer positions we have just found correspond to the correct channels, this arises due to the possibility for 2 different

channels to have the same timing information.

5. Set individual minimum and maximum positions along the buffer for each channel, where the minimum positions will be close to the start value found first and stop positions will be close to the point in the buffer we started this process from.

The result of this is that we define three arrays;

- Starting indices (buffer positions) for each channel, C_{idx}
- Maximum time values for each channel, T_{Max}
- Minimum time values for each channel, T_{Min}

We should be careful to note here that the buffer on the host machine is constantly being written to, as such we have to have a known reference point for when we start counting, we can achieve this by knowing how long the buffer is and by storing the total number of events that have been written to the buffer. With those values known we can then always know exact positions of the time tags in the buffer as each time tag can have both an absolute position known about it (from when counting started) as well as its exact position in the buffer (since the buffer is of a fixed length and eventually we will have to overwrite the values at the start of it).

Now we define an initial value to enter into our main loop, this is the channel in our coincidence pattern with the lowest time tag (i.e. the oldest time tag for our pattern).

Starting Channel & Next Channel

With the initialisation step made we can now enter the main loop, making sure to initialise a counter so that know whether or not we have found the pattern in the current region of the buffer (once delays are accounted for such that coincidence events would be constructed from neighbouring points in the buffer). Starting with our initial value (the oldest channel in our pattern) we now begin to loop over the other channels (making sure to exclude the initial channel so as to avoid double counting and false positive events) in the pattern and their respective timing values. We will use the short hand i for the channel we entered the loop with and j for the channel we are attempting to validate.

Validate Coincidence Window

$$(T_{\text{Max}}[i] - \text{Buffer}[C_{idx}[i]] + \text{Coincidence Window})$$

$$\geq (T_{\text{Max}}[j] - \text{Buffer}[C_{idx}[j]]) \tag{5.1}$$

Now that we can avoid visiting the channel we start to count from we can proceed to validate those that we do need to visit. To do so, the current time tag for channels i and j must be subtracted from their respective Stop positions (as defined in the initialisation step) such that delays are correctly accounted for, the coincidence window is then defined by eq. (5.1)[5];

For increased clarity it may be beneficial to rewrite this relation in the form of eq. (5.2). Here it becomes more clear that delays are accounted for and as a result we look for time tags within the same coincidence window and subsequently compare against the search diameter. In essence the coincidence window acts as a tolerance for channels to be considered valid for our coincidence count. We define this check as successful ($True$) on the condition the minimum channel, i, and our current, j, channels time tags are at a distance smaller than the coincidence window and go to "Increment Counter" otherwise we go to "Exit Validation".

$$\left(\begin{array}{l} T_{\text{Max}}[j] - \text{Buffer}[C_{idx}[j]] \\ - (T_{\text{Max}}[i] - \text{Buffer}[C_{idx}[i]]) \end{array} \right) \leq \text{Coincidence Window} \tag{5.2}$$

Increment Counter

On the condition that "Validate Coincidence Window" is $True$ we increment our check value by 1 and increment our j counter by 1. The check counter allows for us to determine whether or not the time tags produce a valid coincidence event and incrementing the j counter advances us to the next channel in our pattern.

Exit Validation

If at any point whilst looping though the channels in the coincidence pattern we arrive at a distance between the minimum and the current channel that is greater than the search window we immediately exit this loop and proceed to step "Reinitialise".

---

[5]We make use of square brackets here to denote positions along an array much like the syntax used in languages like C/C++ and Python, etc

The channels at this point have become to distant for them to be in coincidence.

Validate Counter

Here we test the check value we increment on the success of "Validate Coincidence Window" if this value is equal to (Pattern length -1) we know that we have found a valid time tag for each channel in the pattern and therefore have found a coincidence event in the buffer. On the case of this test being *True* we proceed to "Coincidence Found" to increment the coincidence count, otherwise we jump to "Reinitialise".

Coincidence Found

We have we found an event we are searching for and so increase our coincidence count by one and then move to "Reinitialise" to reinitialise the loop.

Reinitialise

Finally we update the current index value for the channel we started counting from (minimum channel) and determine which channel now has the minimum value allowing us to re-enter the loop at "Starting Channel" to move along the buffer to start the search for the next valid event.

The method detailed here provides an efficient means to find patterns in the stream of time tags recorded. This efficiency arises by first finding only the range of times we need to look between. We could increase the efficiency further by holding counters for all of the smaller patterns that make up the target pattern, in doing this the cases where we have to start the count for the pattern again wouldn't be lost and could be used record the rates of each of the sources used in an experiment all at the same time. This is a simple extension that could be added to the method if it is needed. By finding the positions needed to count from each time we have to re-enter the loop, and by making use of a coincidence window for the patterns we are searching for, performance is gained in that we can initiate the search from any point within the pattern. This is also a feature of applying the delays and using that to place an index for each channel that is in our reference frame at position zero, however there may be very large distances between the points in the buffer.

5.2.4   Histogramming

Now that we are able to analyse and manipulate time tag data to find specific events within the data stream we can still extend our analysis further. Even though we may *know* the delays for a specific coincidence pattern we are looking for we also know that there is some amount of jitter present and that all of the timing information recorded will have some amount of error present in it, building up a histogram of the results can allow us to explore this feature. Further we can extend this idea if we are using a pulsed pump source and look into correlations that may occur across different pump pulses. This ability enters into a new level of data exploration when we consider using time tagging as an element to construct a spectrometer, if the timing information is of a high enough resolution and the photons we want to measure have had the frequency domain stretched far enough we become able to reconstruct features of their respective wave functions. In the case of SPDC when we engineer crystals for a specific behaviour, for example to increase the purity of the source or maybe so we could entangle photons along more than just the polarisation degree of freedom, this would provide us a method to inspect the structure of the bi-photon state produced allowing us to further determine if our efforts have been successful. These types of measurement will be the subject of chapter 6.

Chapter 6

Joint Spectral Intensity Reconstruction and Purity Estimation

6.1 Introduction

In this chapter I will describe an experimental and computational spectroscopy method we developed for the high-precision study of joint spectra produced by photon-pair sources based on parametric downconversion. The main purpose of this development was to support the design and creation of pure heralded-photon sources employing PDC crystal domain-engineering resulting in heralded-photons with Gaussian-shaped spectra. We first demonstrated this technique in [6], at which point we had not yet constructed the means to measure joint spectra directly, hence we had to resort to auxiliary two-photon interference measurements to establish benchmarks like purity. The Gaussian domain engineering led to an unexpected but most exciting offspring in the form of direct creation of time-frequency modes in a single pass PDC experiment, see F. Graffitti, P. Barrow *et-al.*, PRL 053603 (2020) [7]. For this experiment, a purpose built time-of flight spectrometer and a computational method to turn the resulting "big data" time-tags into joint spectral information was devised. With that experiment completed, this method was then applied to a second generation of Gaussian crystals for pure photon generation, obtaining unprecedented precision with so far the highest reported unfiltered spectra

A. Pickston *et-al.* (under preparation). Finally, we developed an entirely new image processing method which allows for reconstructing data-heavy plots from very few samples reliably.
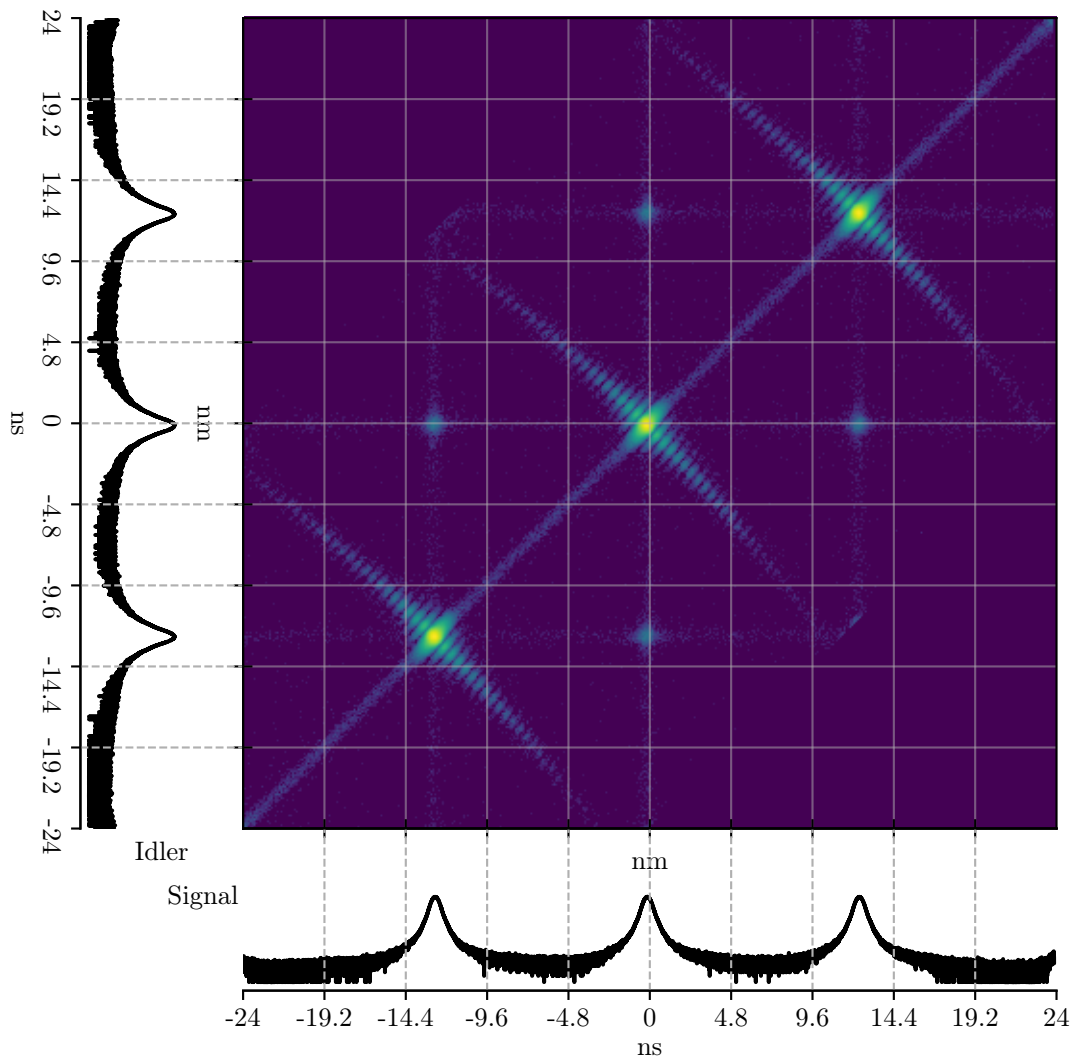
Figure 6.1: **Joint spectral intensity reconstruction (logarithmic pixel intensity.)** From the dispersive time-of-flight spectrometer measurements detailed in this chapter we are able to reconstruct joint spectra of heralded single photons up to a spectral range of 36 nm, $\approx$ 12 times larger than the PDC photons' bandwidth.

6.2 Experimental Setup

Here we detail the experimental configuration applied to measure the output PDC biphoton state and heralded-photon purity of a PDC crystal. Measurement of the biphoton state could be obtained via quantum state tomography in the time fre-

quency mode (TFM) basis [144–146] requiring a cascade of nonlinear processes, or by reconstruction of the joint spectral amplitude, requiring complex interferometric techniques [147–149]. Alternatively we can use spectroscopic methods to reconstruct joint spectral intensity (the absolute square of the JSA) of the heralded single-photons, using grating spectrometers or dispersive spectroscopy [150] or even via stimulated emission tomography [151, 152]. Typically, commercial high-resolution spectrometers lack single-photon sensitivity with those that do being slow to operate and lacking the ability to measure photons in coincidence, a feature crucial for measuring the joint spectra. We make use of dispersive spectroscopic techniques [150, 153] to characterise the JSI of a selection of PDC crystals. In our experimental configuration we make use of long single mode fibre (SMF-28) to provide our dispersion, for this we need to determine a length of fibre that will allow us to resolve the spectra at a high enough spectral resolution.
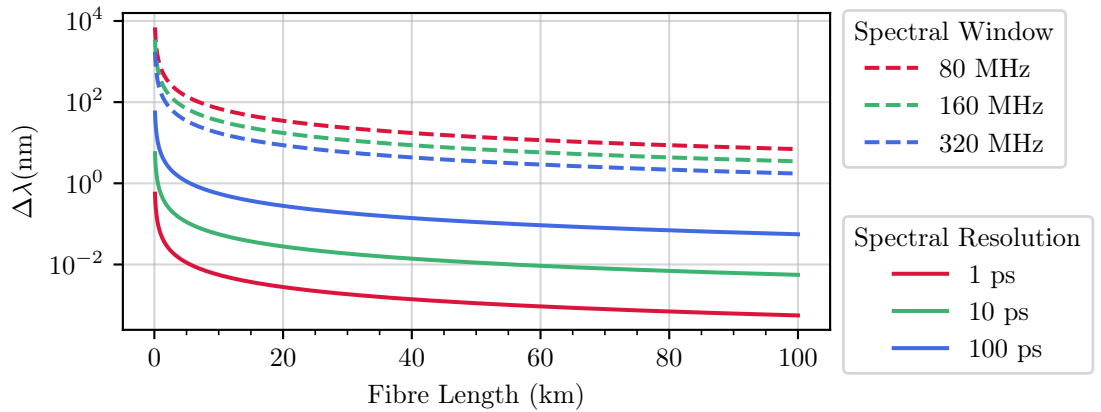
Figure 6.2: **Spectral resolution and spectral window as a function of fi-bre length** Increasing the length of optical fibre used to disperse single photons ($\lambda = 1550$nm) results in a decrease in spectral window and an increase in spectral resolution. These parameters must be balanced according to the repetition rate of the laser and timing resolution of our hardware. The narrowing of the spectral window is worse for faster repetition rates limiting the amount of dispersion that would be usable faster. It is also shown that improving the size of the time bins for our timing hardware from 100 ps to 1 ps, provides very significant improvements in how much dispersion is needed to resolve smaller details. An 80 MHz pump and 1 ps time bin width with 20 km of fibre have been chosen for our experiment.

It is important to not provide so much dispersion that we limit the spectral window, since we will be making use of time-of-flight measurement we need the spectral window in terms of time to be as wide as the peak-to-peak time of our

pump laser. To determine these parameters we use:

$$\Delta t = c_\lambda \cdot L \cdot \Delta\lambda, \tag{6.1}$$

where   is spectral bandwidth, the dispersion coefficient is defined by c_λ and L is the fibre length. We can determine the spectral resolution, $\Delta\lambda$, by specifying a minimum temporal resolution and a length of fibre, this is shown in fig. 6.2 for 1 ps, 10 ps and 100 ps. The delays fibres used are Corning SMF-28 single-mode fibres where $c_\lambda = 18$ ps/km/nm at a centre wavelength of 1550 nm. Using this and the knowledge that we have an 80 MHz repetition rate pump laser, Spectra-Physics Tsunami Ti:Sapphire, and timing electronics with a resolution of 1 ps, Picoquant Hydraharp, we can determine an ideal length of fibre to use.

We have chosen 20 km of fibre for the delay lines to build the dispersive spectrometer, providing a convenient balance between spectral resolution and the size of the spectral window for our measurements, details of which can be seen in fig. 6.2. This combination of parameters will allow us to measure the entire spectral range between neighbouring pump pulses and provide a high resolution without the need to limit the spectral window. We see this trade-off in such measures focusing on the central peak of the JSI in order to increase the spectral resolution [154, 155] which in turn results in the loss of any correlations that may be present away from the centre, these extra correlations are however key in accurate and reliable estimations of single photon purity.

The dispersion from the delay fibre allows us to "stretch" a pulse over a larger temporal range, shown in fig. 6.3. Without the use of the delay fibre we can resolve a FWHM of 72 ps for either of the output modes emitted from our PDC source, by including the delay fibre the dispersion present causes a temporal stretching leading to a 15.25 times increase in the FWHM. This lengthening in the FWHM allows us to resolve the spectra in greater detail when using a time tagging device with a 1 ps binning, with the final timing resolution being limited by detector jitter, resulting in ≈ 72 ps of timing resolution.

The setup detailed in fig. 6.4 is used to reconstruct the JSI from a single PDC source. Each of the two photons emitted is sent through an ≈ 20 km single mode-mode fibre before arriving at our SNSPDs, each with an 80% detection efficiency
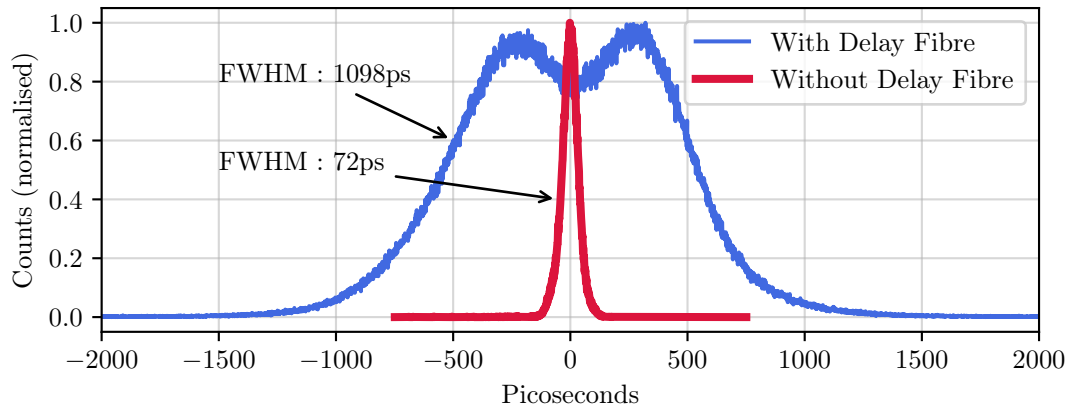
Figure 6.3: **Effect of dispersion on a single heralded-photon.** The effect of dispersion allows for a pulse to be broadened. Both pulse shapes shown here are from the same source however the application of dispersion allows us to see the structure of the pulse in greater detail. The narrower pulse shape outline the need for very high timing resolutions as the level of detail found in the broader pulse requires 20 km of optical fibre with a dispersion coefficient of $\approx$18ps/Km/nm paired with a timing resolution of 1ps. The central dip seen here is caused by the tailoring of the PDC crystals joint spectra, which takes the form of a Hermite-Gauss mode.

and < 50 ps jitter. The photon arrival times are then recorded by a Picoquant Hydraharp for offline processing.

6.3 Calibration

The experimental configurations detailed above for dispersive spectroscopy provide a measurement in units of time, to translate any resulting measurements to wavelengths it requires calibration against a known device. For this we send single photons through our long dispersive fibres and measure each (signal or idler) individually with a single-photon spectrometer. Due to only being able to measure the effects of a single fibre and as a result either the signal or idler at a time we can only extract a result for the marginal spectra of our joint spectrum. The calibration was performed only with crystals engineered to produce time-frequency modes, the details of which do not matter much for calibration purposes and will be explained in a later section. Re-calibration with other crystal types was deemed unnecessary as the rest of the experimental set-up remained unchanged.

6.3.1 Single-Photon Spectrometer

Instead of performing an absolute calibration against a known frequency standard, we chose to calibrate against a commercial grating-based spectrometer. We used a Teledyne Princeton Instruments IsoPlane 320 grating spectrometer with 0.05nm resolution at 1550nm, which was equipped with a single-photon sensitive EM-CCD camera. Results of this can be seen in fig. 6.6, limiting the range to a 20 nm window, well beyond the design bandwidth of our heralded photons.

With single-photon calibration spectra independently recorded we turn our attention back to the fibre spectrometer we have constructed. To complete calibration using the independent spectrometer data, it will have to be compared to arrival
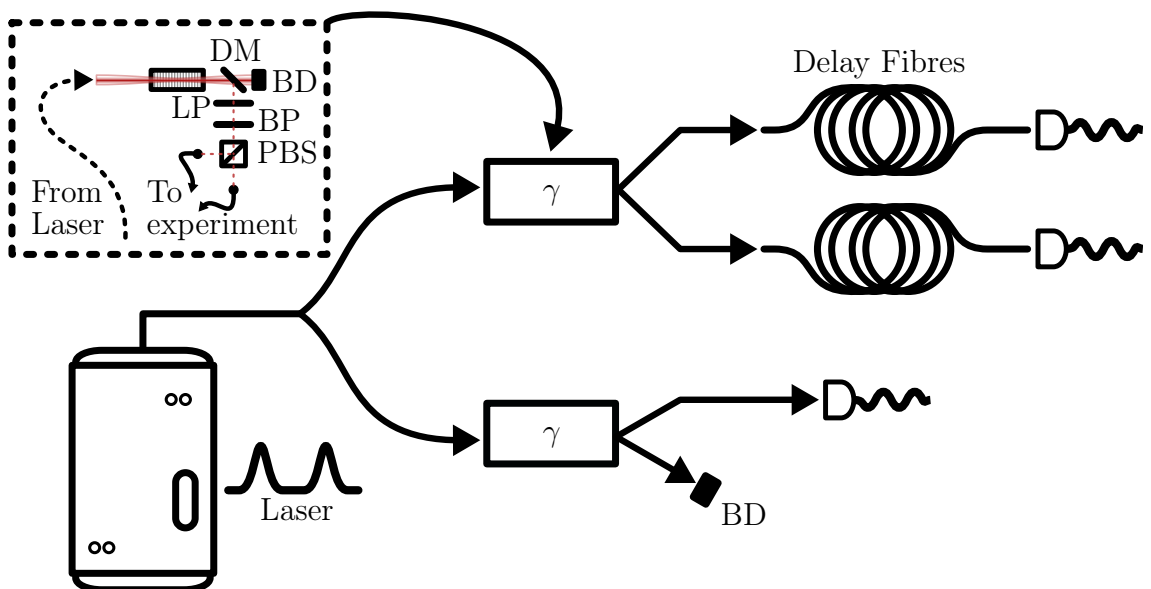
Figure 6.4: **Experimental configuration for dispersive spectroscopy of two-photons.** Entangled pair source (upper right) and biphoton state characterisation. A pulsed Ti:Sapphire laser with 80 MHz repetition rate, 1.3 ps $sech^2$ pulses at 775 nm is focused into the tailored KTP crystal to create 1550 nm photon pairs via collinear, type-II PDC. The orthogonally-polarised down-converted photons are filtered from the pump with a dichroic mirror (DM), a long-pass (LP) and a loose band-pass (BP) filter (with a bandwidth $\approx$ 3 times larger than the PDC photons' bandwidth). The entanglement quality and number of modes of the PDC pair can be benchmarked with joint spectrum reconstruction via dispersive fibre time-of-flight spectroscopy. Here we use a single output from a second source operated at a higher pump power than the source we measure the joint spectrum from as a clock source giving us absolute timing to complete the reconstruction with. Alternatively a photodiode could be used to measure the clock of the pump laser providing in this case a stead 80 MHz absolute timing source. However, here the lower jitter of the single-photon detectors was favoured in order to ensure timing accuracy.
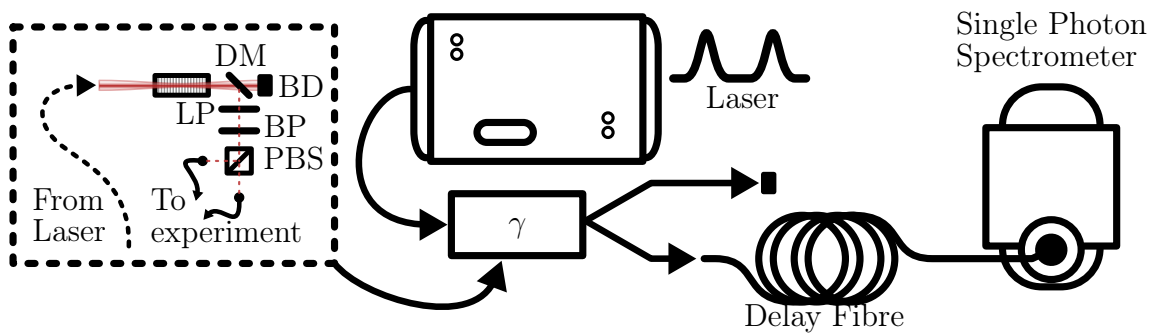
Figure 6.5: **Experimental configuration of single-photon spectra.** Single-photons emitted from our source and then traverse the length of the delay fibre before reaching the single-photon spectrometer. From there the spectra is measured.
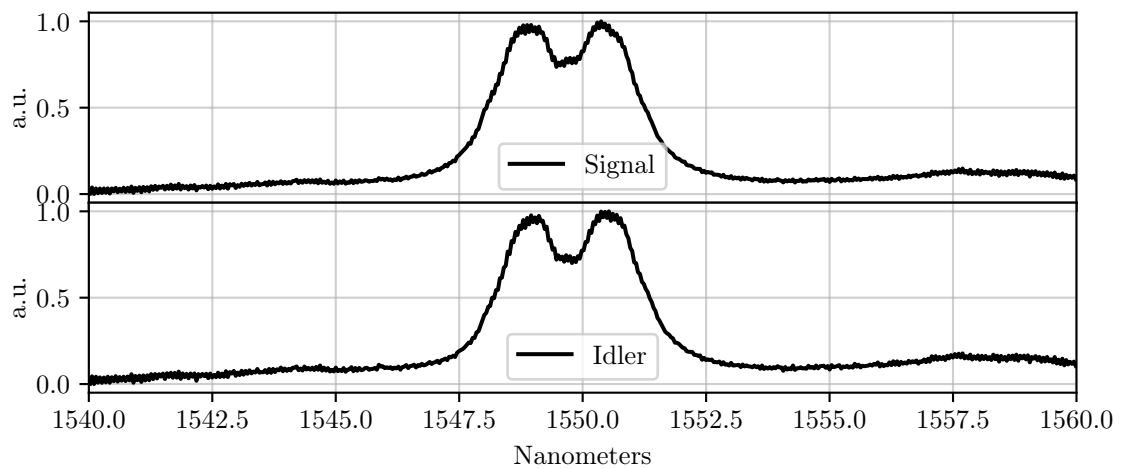
Figure 6.6: **Signal and idler spectra recorded on an EM-CCD based single-photon spectrometer.** The intensity values for each wavelength have been normalised to unity over the region we are interested in most.

time measurements of heralded single-photons. The resulting spectra are shown in fig. 6.7.

Finally we come to the calibration. Combining the spectra displayed in figs. 6.6 and 6.7 we take the FWHM of each spectra in the wavelength and temporal bases, dividing one by the other to determine the number of nanometres per picosecond. We see consistent calibration results for both signal and idler photons output from either port of the beamsplitter, providing a calibration of ≈ 0.003 nm/ps. The central wavelength of each spectra in fig. 6.6 can then be used to set the equivalent central wavelength of fig. 6.7 at zero arrival time after converting time to wavelength. With this complete we will now be able to view the spectra in both the temporal and spectral domain.
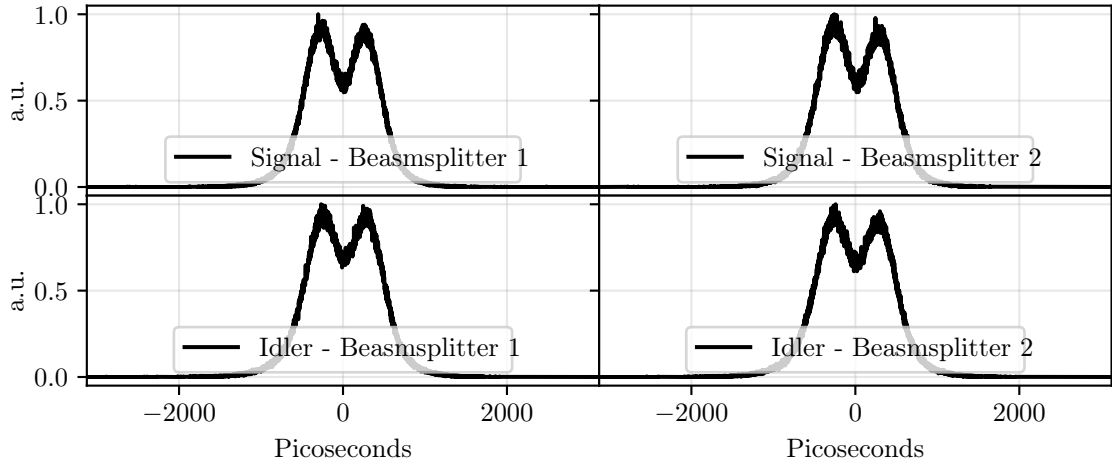
Figure 6.7: **Heralded single-photon arrival time spectra.** Single-photon spectra measured using dispersive spectroscopy and picosecond timing resolution of both signal and idler PDC modes from either output ports of a fibre beamsplitter.
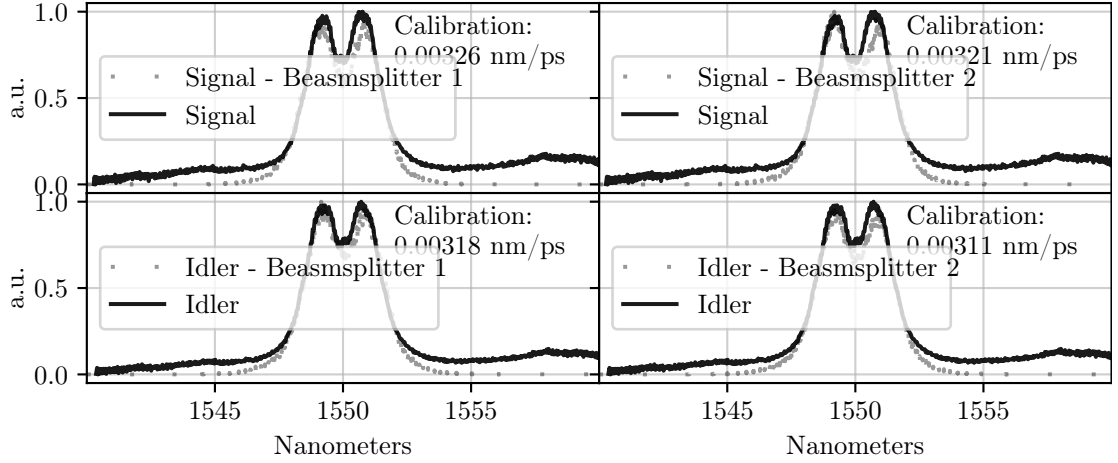
Figure 6.8: **Calibration for both signal and idler with either of the beamsplitter output modes.** In each case we see a calibration of ≈ 0.003nm/ps.

6.4 Result of JSI Reconstruction

Here we display the resulting reconstructed JSI for the following crystals:

- 28 mm ppKTP,

- 30 mm apodised KTP — "Gaussian",

- 30 mm Engineered for time-frequency mode creation — "Antisymmetric".

For the ppKTP and Gaussian cases we include measurements with and without some additional filtering. Filtering for the ppKTP crystals comes from an Alluxa bandpass filter centred at 1550 nm with a 2.8 nm FWHM and a Semrock bandpass filter centred at 1550 nm with a 7.4 nm FWHM. Each crystal and filter combination will use the two-photon spectroscopic method detailed in fig. 6.4 with additional
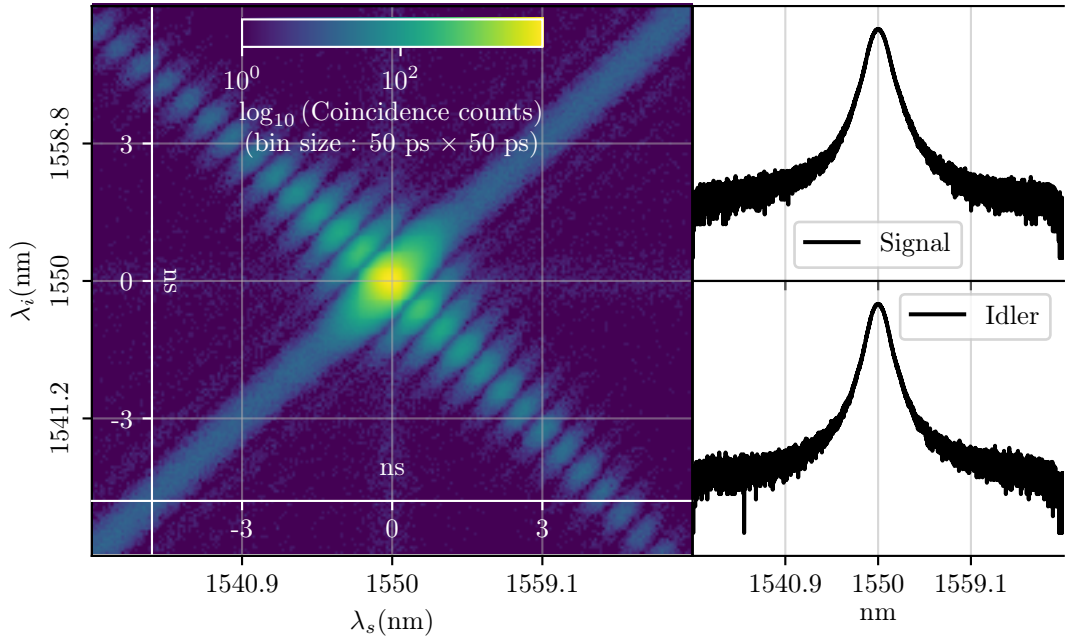
Figure 6.9: **Reconstruction of the joint spectra produced from a ppKTP crystal.** We can see the extent of the side-lobes caused by the "on-off" nature of the nonlinearity present in ppKTP crystals. Marginal spectra for the signal and idler modes are displayed in the right most panels.

measurements made for the antisymmetric crystal where two sources are constructed and entanglement swapping is used, see fig. 6.15. In this section and the following subsections the joint spectra will be displayed and discussed followed by estimations of the spectral purity of the heralded single-photons in the subsequent section.

Seen in fig. 6.9 is the JSI reconstructed for a ppKTP crystal. Designed for use with a Gaussian pump envelope function centred at 791 nm operating in a symmetric GVM regime, we observe an elliptical central lobe instead of a circular one due to our use of a mode-locked sech^2 pump envelope. The use of an incorrectly matched pump with this crystal will influence the purity of the single-photons.

The side lobes are clearly present in fig. 6.9 where they can be seen extending across the entire peak-to-peak time for the pump laser (12.5ns). The figure has been plotted with a logarithmic scale for the pixel intensity. It can also be seen, extending across the diagonal (bottom left to top right) a faint line with the same width of that as the central lobe. This band is caused by a continuous-wave background present in the pump pulse train. As a result of it being continuous it is not possible to extract correct timing information from any of the coincidences produced from
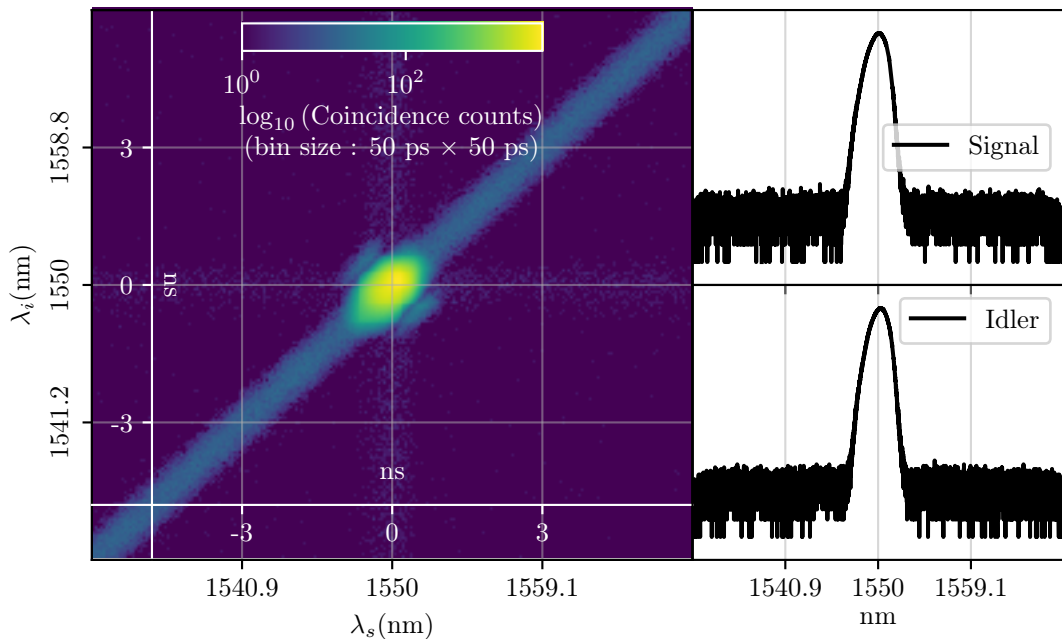
Figure 6.10: **Reconstructed JSI of filtered ppKTP crystal.** In comparison to fig. 6.9 we can see the effects of filtering to isolate the central lobe. We can clearly see that application of filtering allows us to remove much of the unwanted correlations and in combination the removal of these correlations also results in a reduction in the brightness as the photons resulting in the extra lobes are blocked out.

emissions caused by this element and as a result they form a band with zero relative delay between each photon. This is an artefact present in all of our measured joint spectra, when it comes to purity estimation we include these intensities as they are only present as a faint band when displaying the logarithm of the intensities.

The side lobes present in fig. 6.9 we proceed to apply spectral filtering to suppress their presence as shown by fig. 6.10. The difference between unfiltered and filtered cases is clear for the ppKTP crystal, with tight enough filtering it is possible to suppress all of the side lobes that naturally present themselves in the joint spectrum. We can see from fig. 6.10 that the filtering has removed almost all of the side lobes with only a small sliver visible in the first of each side lobe from the centre.

The central peak of the spectra is slightly misshaped, this is due to a slight centre-frequency mismatch in the filter in one arm of the source causing a slight bias in the result[1]. Whilst filtering does allow us to achieve a higher purity for our

---

[1]Slightly tilting the filter with respect to perpendicular of the beam path allows for some degree of tuning of the cut-off wavelength from the filters centre. It can be seen in this case that the tuning was not exact.
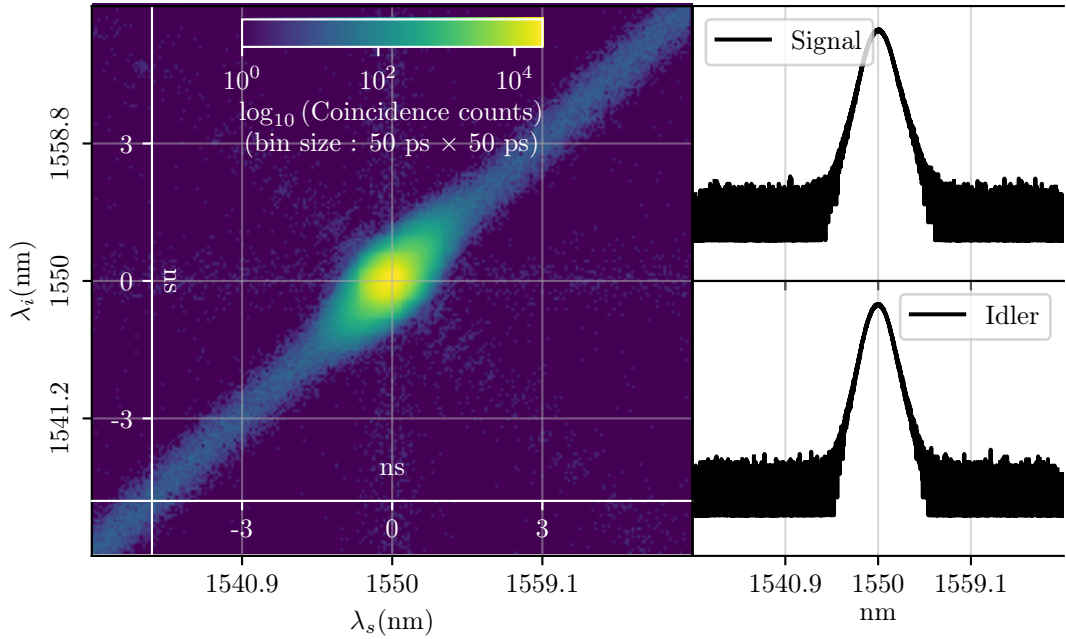
Figure 6.11: **Domain engineering allows for production of the central lobe alone.** With domain engineering we gain the option to avoid filtering the output of the PDC process. Comparing the result here to those in figs. 6.9 and 6.10 the side lobes we would have to remove after emission are non-existent here. We only produce the correlations we need and nothing else. Whilst this increases the purity of the emission it should be noted that the brightness doesn't reach the same level as that of the unfiltered ppKTP crystal.

states it is at the cost of source brightness and as a result reduces the probability of detecting a pair of photons per pulse (clock cycle), meaning that when using heavily filtered sources we will likely enter a regime where the success probability of the quantum protocol we are investigating is too low and as a result the time taken to complete our measurement may become infeasible (fig. 4.3).

An alternative to filtering the emission of a PDC crystal would be to engineer the crystal such that no side lobes are present by design. The heralded single photons would possess a higher spectral purity and have the potential to achieve higher brightness than the filtered ppKTP crystal, both of which are highly desirable quantities for experimental realisations of quantum information protocols.

The result of a crystal designed with these properties in mind can be seen in fig. 6.11, the Gaussian designed domain-engineered crystal presented is our second generation of the crystal designed by our group [6]. The crystal engineering process relies on shaping of the JSA. In particular we know the shape of the pump envelop
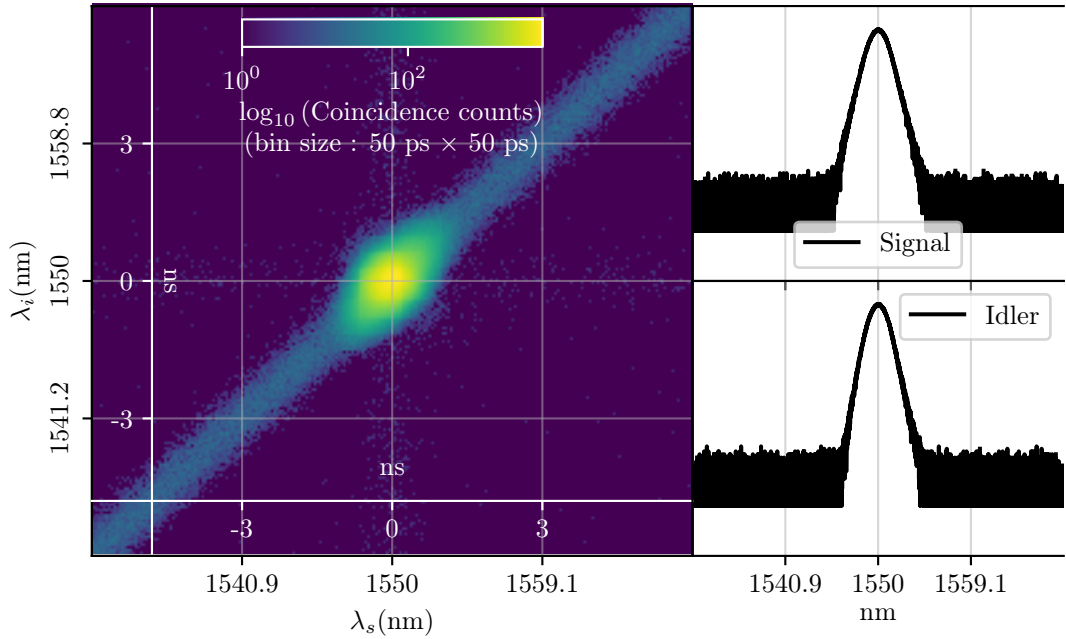
Figure 6.12: **Domain engineering plus additional filtering can isolate the central lobe further.** Whilst fig. 6.11 shows what can be achieved with domain engineering of the crystals here we show how the addition of some *gentle* filtering can improve the purity in the spectrum further.

function eq. (2.10) of our laser, a transform-limited sech^2 pulse centred at 775 nm. Then, operating in a symmetric GVM regime we define a PMF (eq. (2.11)) taking the shape of a Gaussian function, using methods described in [67] the poling structure of the KTP crystal can desined to reflect the Gaussian PMF. With this method it becomes possible to produce joint spectra with a central lobe closer in shape to a Gaussian function lacking the characteristic sinc side lobes and so higher spectral purity in the heralded single-photons when compared to ppKTP. As a step further, we add some filtering to the measurement in fig. 6.11 to eliminate the faint side lobes seen extending from the central lobe, the results of which can be seen in fig. 6.12.

6.4.1 Direct Generation of Time-Frequency Modes

Of the investigation into crystal domain engineering [6] the idea to develop a crystal with novel properties surfaced, possessing time-frequency mode (TFM) entanglement. Encoding quantum information in the time-frequency degree of freedom enables access to a higher-dimensional Hilbert space, which increases quantum information capacity but also robustness to noise [156–161] and robustness against
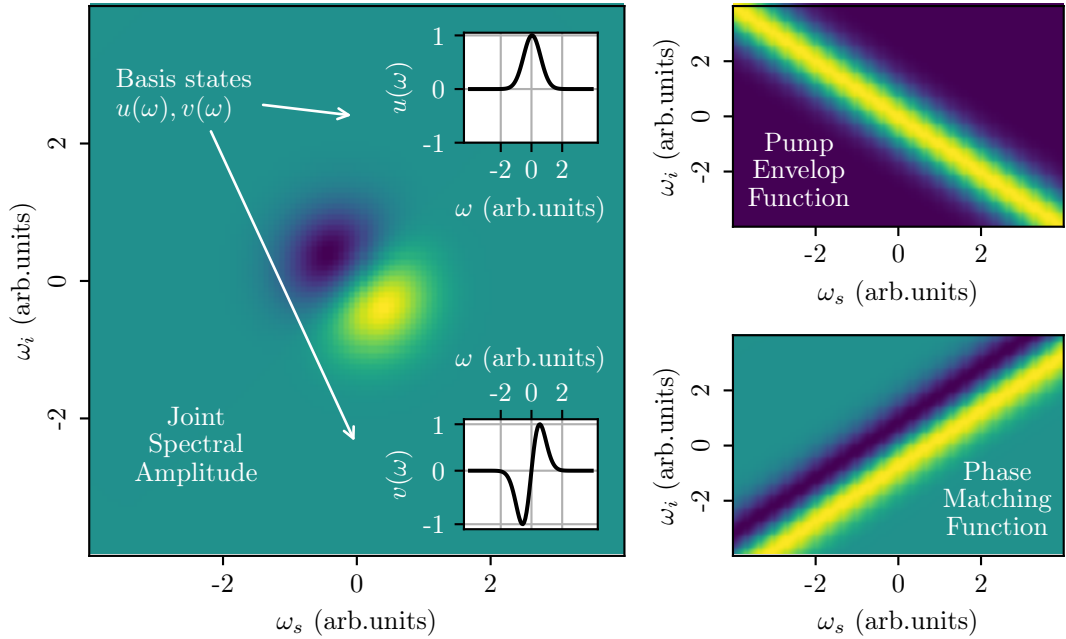
Figure 6.13: **Theoretical joint spectral intensity for direct generation of time-frequency modes.** From a Gaussian pump envelope function and an antisymmetric phase-matching function, shaped as the first-order Hermite-Gaussian function, a joint spectra defining time-frequency modes can be created. The resulting joint spectra provides a maximally entangled joint spectral amplitude, with the corresponding TFM basis states $u(\omega)$ and $v(\omega)$

chromatic dispersion [162] all of which are problems to overcome for use in fibre networks.

Time-frequency modes can be developed by shaping of the joint spectral amplitude (see section 2.1.2). The process to engineer crystals has been stated in the previous section with respect to the Gaussian crystals developed. Reapplying the idea of shaping the JSA, we now consider one taking the form of a Hermite-Gauss function, with the goal of generating the maximally-entangled antisymmetric Bell-state:

$$|\psi^-\rangle_{s,i} = \frac{1}{\sqrt{2}} \left(|\wedge\rangle_s |\vee\vee\rangle_i - |\vee\vee\rangle_s |\wedge\rangle_i \right) \tag{6.2}$$

The state defined in eq. (6.2) corresponds to the joint spectrum encoded in the TFM basis states $\wedge = u(\omega)$ and $\vee\vee = v(\omega)$. Using the nonlinearity engineering algorithm developed in [67] the PMF can be shaped as a first-order Hermite-Gauss function. This has resulted in the creation of a 30 mm KTP crystal designed with
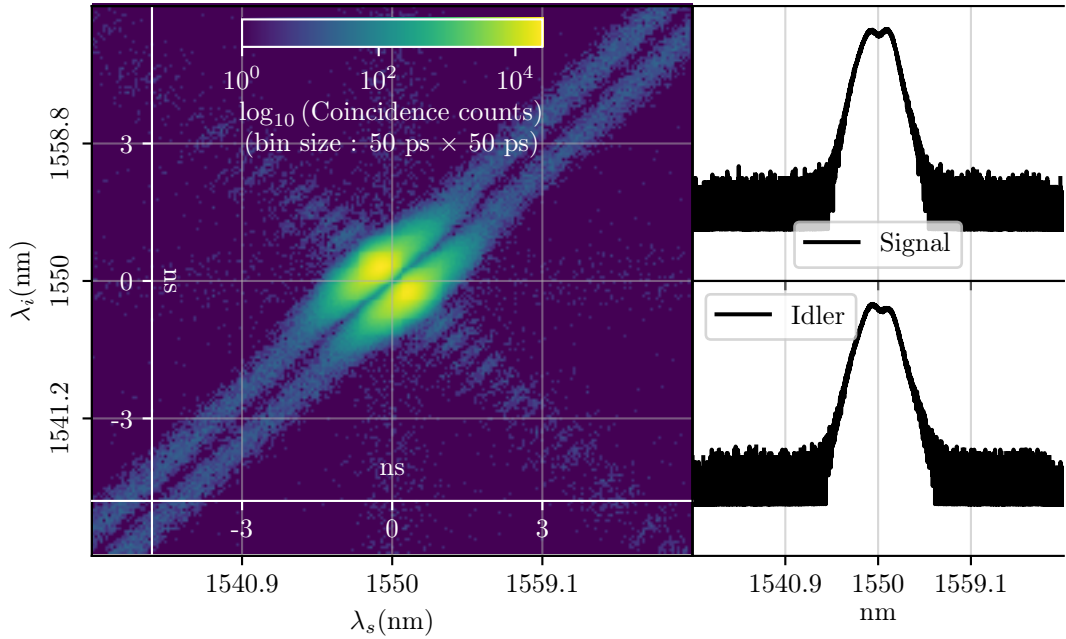
Figure 6.14: **JSI produced by a PDC source designed with frequency encoding.** Unlike any of the spectra shown so far, here we can see the effect of creating a crystal designed to produce an anti-symmetric bi-photon state. We now see a pair of lobes in the centre. The nature of the engineering here can be seen as still "imperfect" due to the side lobes seen extending across the diagonal, in comparison to the ppKTP case however, these are very faint compared to the central lobes.

a symmetric GVM condition for a 1.3 ps laser pulse [68] where each domain is $\approx$ 23.1 μm wide, equal to the coherence length of a 775 nm pump down-converted into a pair of 1550 nm PDC photons. The engineering algorithm tracks the PDC amplitude as it moves along the crystal, checking whether each domain should be oriented up or down while minimising the distance between the resulting amplitude and the ideal target.

The first mode of the Hermite-Gauss function used to define the JSA contains a phase which can't be measured with our dispersive spectroscopic method, the produced JSI then approximates the absolute value of the JSA. Using the single crystal two-photon coincidence measurement detailed in fig. 6.4 to reconstruct the $|\psi^-\rangle$ state eq. (6.2) we successfully reconstruct the JSI in fig. 6.14. The two central lobes of the Hermite-Gauss function are clearly visible, along with some artefacts from the engineering algorithm (noting that like the rest of the JSI reconstruction figures this is plotted as the $\log_{10}$ of the intensities).

In order to use PDC crystals designed to emit TFMs in multiphoton protocols the
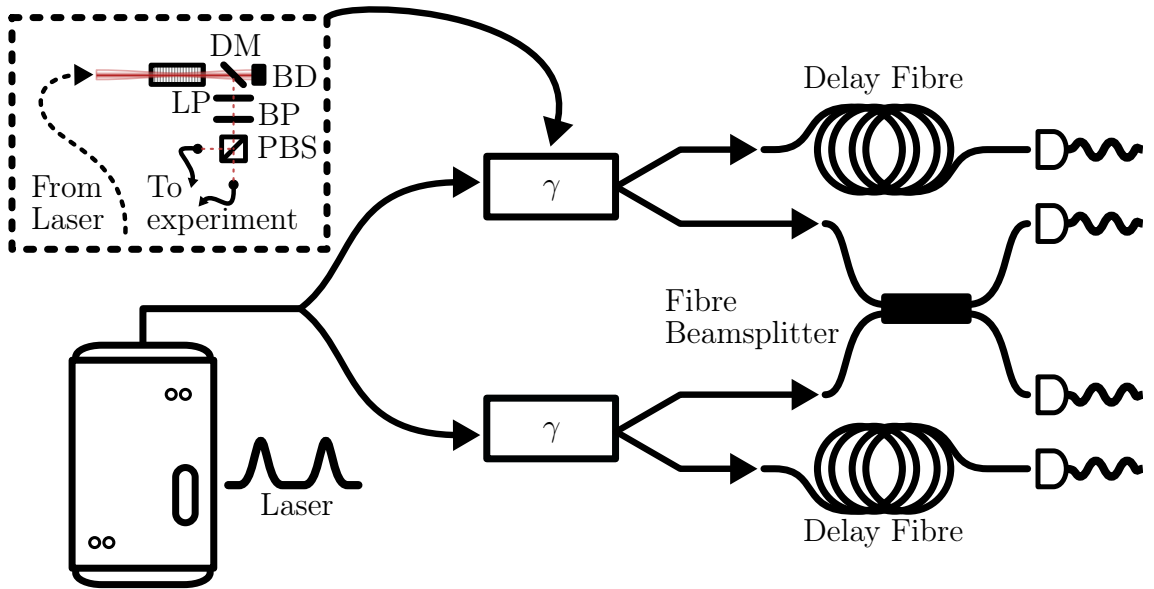
Figure 6.15: **Experimental configuration for dispersive spectroscopy with entanglement swapping.** Entangled pair source (upper right) and biphoton state characterisation. A pulsed Ti:Sapphire laser with 80 MHz repetition rate, 1.3 ps sech 2 pulses at 775 nm is focused into the tailored KTP crystal to create 1550 nm photon pairs via collinear, type-II PDC. The orthogonally-polarised down-converted photons are filtered from the pump with a dichroic mirror (DM), a long-pass (LP) and a loose band-pass (BP) filter (with a bandwidth $\approx$ 3 times larger than the PDC photons' bandwidth). The entanglement quality and number of modes of the PDC pair can be benchmarked with joint spectrum reconstruction via dispersive fibre time-of-flight spectroscopy and two-photon interference in a fibre beamsplitter. The beamsplitter facilitates entanglement swapping, heralded by a coincidence detection of the photons after the fibre beamsplitter. The resulting swapped state is then verified via fibre spectroscopy.

ability to interfere and swap independently generated TFM-encoded photons is key. A generalised entanglement swapping for TFM has been proposed, based upon non-linear processess between two single-photons, it however suffers from very low success probability [163]. Instead, we implement the standard entanglement swapping using a pair of sources built with these antisymmetric crystals. By interfering a single photon from each source on a fibre beamsplitter as shown in fig. 6.15 we can swap entanglement between the two independently generated $|\psi^-\rangle$ states. The resulting four-photon state can be written as $1/2(|\phi^+\rangle|\phi^+\rangle + |\phi^-\rangle|\phi^-\rangle + |\psi^+\rangle|\psi^+\rangle - |\psi^-\rangle|\psi^-\rangle)$, a coherent sum of the four Bell states:

$$
\begin{aligned}
|\psi^\pm\rangle &= \tfrac{1}{\sqrt{2}}\left(|\curvearrowleft\rangle|\curvearrowright\rangle \pm |\curvearrowright\rangle|\curvearrowleft\rangle\right) \\
|\phi^\pm\rangle &= \tfrac{1}{\sqrt{2}}\left(|\curvearrowleft\rangle|\curvearrowleft\rangle \pm |\curvearrowright\rangle|\curvearrowright\rangle\right)
\end{aligned}
. \tag{6.3}
$$
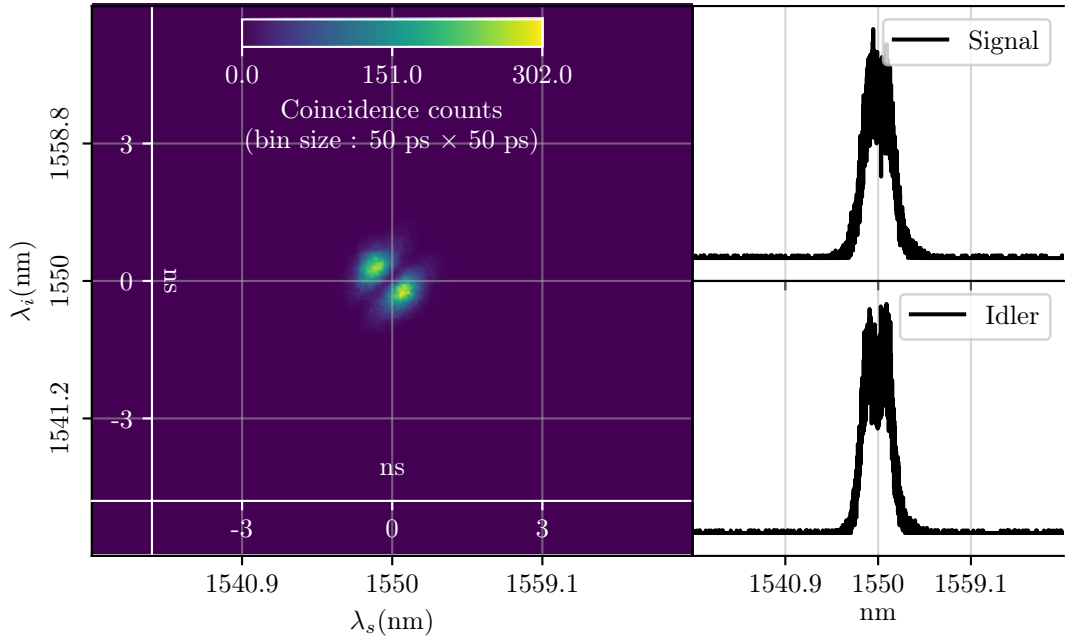
Figure 6.16: **Four-photon JSI reconstruction of antisymmetric $|\psi^-\rangle$ state.** When considering the 4-photon version of the result seen in fig. 6.14 we can immediately see the requirement to record data for a much longer measurement time in order to collect enough 4 photon events.

The antibunching present in the singlet state is a result of its antisymmetry, conversely the triplet states possess symmetry and so bunch. Detecting a two-photon coincidence event at the two output ports of the beamsplitter corresponds to a successful projection onto the singlet state and heralds the swapping of the TFM $|\psi^-\rangle$ from the two photons incident on the beamsplitter to the two non-interacting photons.

To evaluate this entanglement swapping scheme we have chosen to measure both interference between signal and idler photons, one from each source, and interference between signal photons from both sources. Measurement for the "signal — idler" entanglement swapping can be seen in fig. 6.16 with "signal — signal" swapping shown in fig. 6.17. As we expect, post-selecting on a coincidence event on both output ports of the beamsplitter results in reconstruction of the $|\psi^-\rangle$ matching what is seen in the single crystal measurement fig. 6.14, this of course should come as no surprise. Whilst differences between both of these four-photon measurements are subtle, it can be seen that the gap between the two lobes, where the JSA would cross zero, is more defined in the "signal — signal" measurement. This difference is
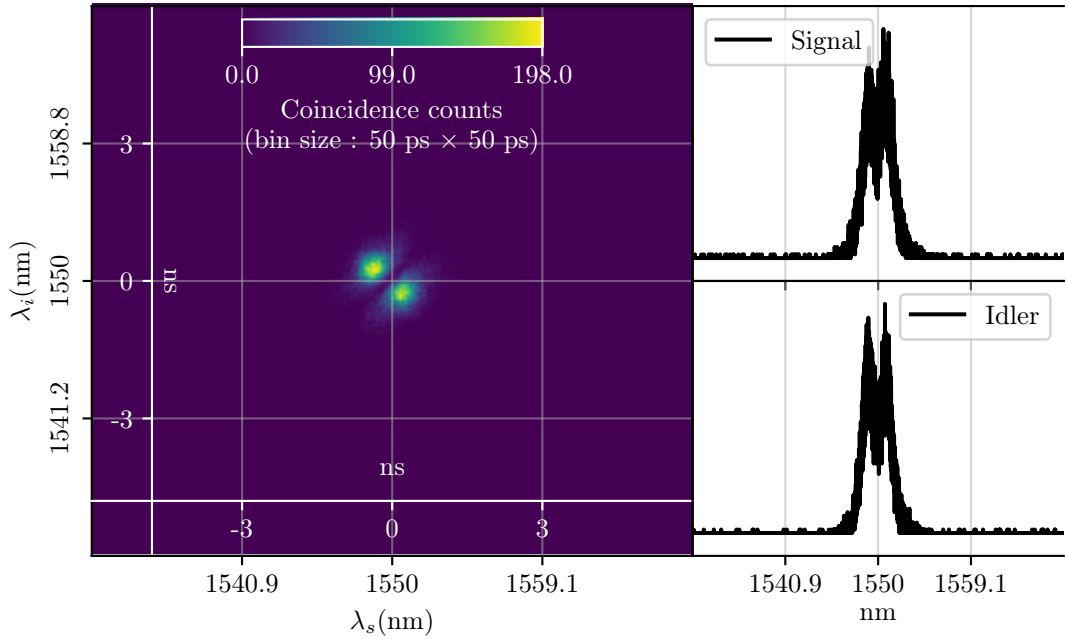
Figure 6.17: **Further four-photon JSI reconstruction of antisymmetric $|\psi^-\rangle$ state.** Whilst the spectrum here may look to be the same as in fig. 6.16 we instead chose to interfere both signal photons produced by the two independent sources versus signal and idler in the previous case. The result of this is a slight change in the purity and most clearly from these plots is the increase in the contrast of the dip in the marginal spectra.

more pronounced in the marginal spectra, where the dip at the centre of the peak is stronger.

The final set of measurements under the entanglement swapping scheme is for the case where we post-select on a photon from either of the beamsplitter outputs. We again choose to measure both the "signal — idler" and "signal — signal" entanglement swapping, configurations producing the JSI reconstructions shown in figs. 6.18 and 6.19. In these measurements we now see four peaks, produced by a mixture of the four equally weighted Bell state JSAs. Much like for the $|\psi^-\rangle$ state JSI we again see more detail in the dip at the centre of both the signal and idler marginals in "signal — signal" swapping. The consistency of this behaviour in both schemes suggest that a higher interference visibility is achievable in the "signal — signal" swapping case, this could be due to slight differences in the signal and idler wavelengths where we have a smaller difference in wavelengths between both of the signal photons.

It is possible to introduce small variations in the widths of the crystals domains
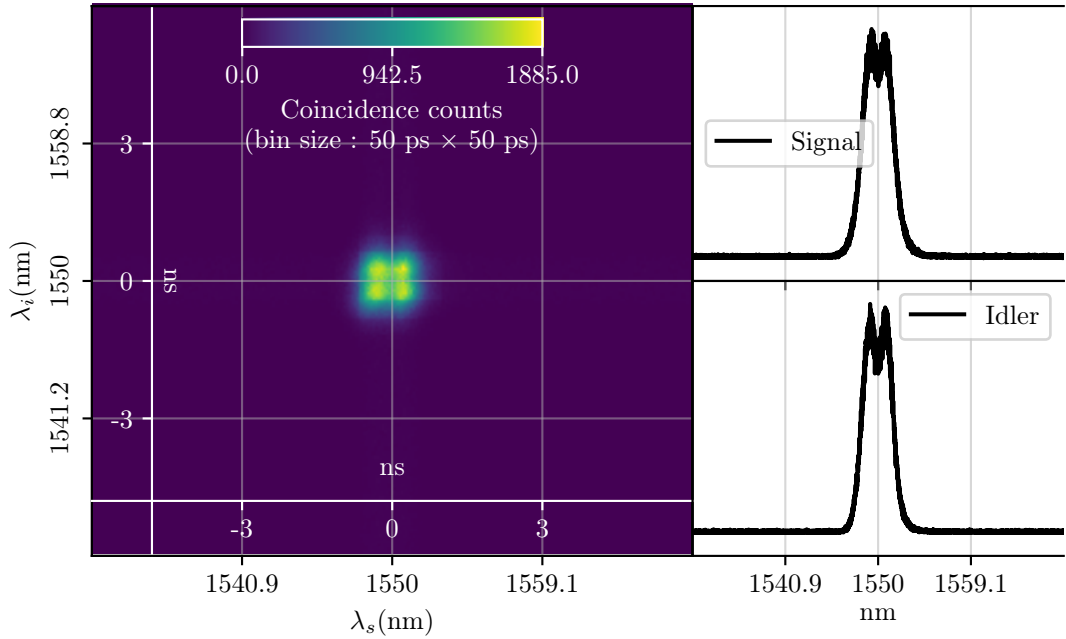
Figure 6.18: **Four-photon JSI reconstruction of mixed Bell state, with signal-idler interference.** Much like in fig. 6.18 we have chose to interfere both the signal and idler photons from each source, here however we turn out attention to the triplet state. The mixing of states is shown by the presence of a single lobe in each quadrant from the centre. Much like in the singlet measurements the marginal spectra displays the same form as we have to trace over the corresponding photon in the state removing much of the information allowing us to see as clear a difference as that shown by the joint spectrum.

by changing the temperature of the crystal. This results in a shift of the PMF in the (ω_s, ω_i) plane, allowing for the production of frequency non-degenerate photons. In the same way the temperature of the crystals can be tuned to get closer to fully frequency degenerate photons and so increase the interference visibility. The behaviour between "signal — idler" and "signal — signal" suggests that some temperature tuning may have been needed to optimise each case.

6.5   Purity Estimation

Whilst the ability to plot the joint spectrum of our produced biphoton states may provide us visual insight into their respective structures the feature of primary interest is that of the state's purity. The data recorded provides a means to calculate the spectral purity of our states, calculation of the number purity is outside of the scope of this experimental method alone as we lack information about the number of pho-
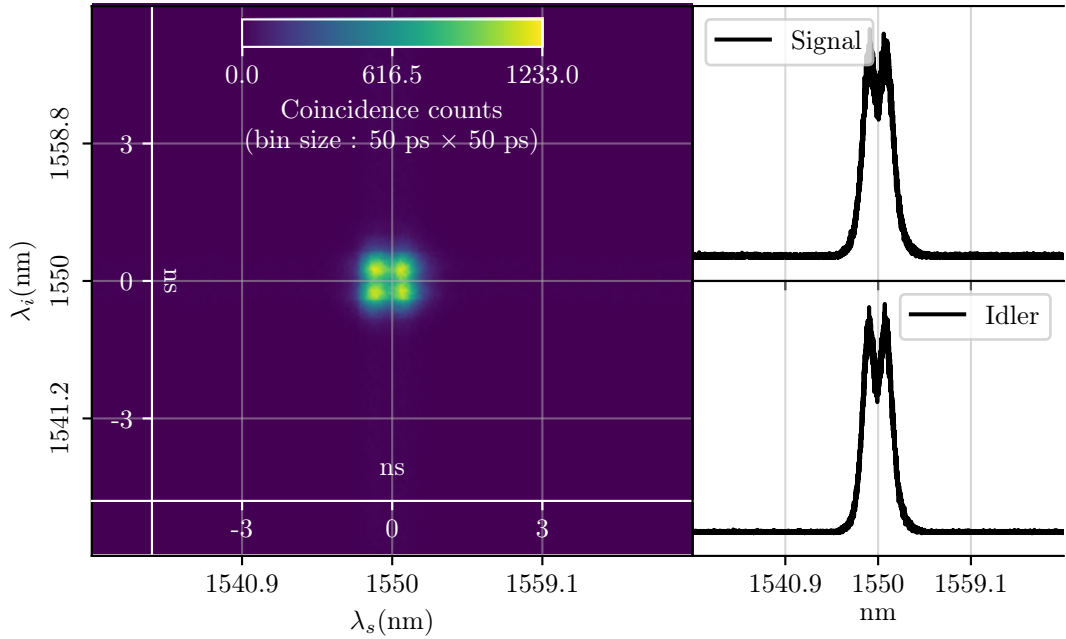
Figure 6.19: **Four-photon JSI reconstruction of mixed Bell state, with signal-signal interference.** Just like the singlet states we have also chosen to produce the triplet state in the case of interfering both of the signal photons. Most notably, the difference between this result and the triplet state produced between the signal and idler in fig. 6.18 is the increase in contrast between the individual lobes along with the contrast of the central dip in the in the marginals. This effect implies a stronger degree of interference between signal-signal than with signal-idler suggesting the detected state is of a higher purity.

tons that arrive at each detector for each detection event. However, we can obtain knowledge into the number purity through the analysis of two-photon interference experiments with the detector model such that we can estimate the signal-to-noise ratio of a single photon source.

The Schmidt decomposition allows for the calculation of spectral purity by factorising the JSI into a linear combination of the orthogonal functions of the signal and idler frequencies with the Schmidt magnitudes,κ_k.

By then taking the reciprocal of K we then arrive at the spectral purity. Since an analytical method is not necessarily derivable for our measurement we must instead use a numerical method to decompose the JSI, into a matrix each for the signal and idler modes as well as a third matrix containing the correlations between the modes. The numerical method needed is that of singular value decomposition, effectively a matrix operation analogue of the Schmidt decomposition, which takes the form of;

Crystal	Filtering	Bin Width (ps)	Theoretical Purity ($\sqrt{JSI}$)	$p\left(|\sqrt{JSI}|\right)$	$\overline{p\left(|\sqrt{JSI}|\right)}$	$\sigma\left(p\left(|\sqrt{JSI}|\right)\right)$
Antisymmetric	None	1		44.130		
Antisymmetric	None	20	50.000	65.279	65.124	0.017
Antisymmetric	None	50		65.844	65.795	0.017
Antisymmetric	None	100		66.978	66.956	0.017
Gaussian	None	1		57.881		
Gaussian	None	20	98.600	84.428	84.303	0.020
Gaussian	None	50		84.753	84.747	0.020
Gaussian	None	100		85.011	85.030	0.020
Gaussian	Semrock	1		59.214		
Gaussian	Semrock	20	98.697	90.945	90.757	0.019
Gaussian	Semrock	50		91.227	91.174	0.019
Gaussian	Semrock	100		91.404	91.378	0.019
ppKTP	None	1		65.880		
ppKTP	None	20	80.701	82.038	83.131	0.016
ppKTP	None	50		82.407	83.591	0.016
ppKTP	None	100		82.880	84.086	0.016
ppKTP	Alluxa	1		45.350		
ppKTP	Alluxa	20	98.397	94.115	93.845	0.031
ppKTP	Alluxa	50		94.490	94.430	0.031
ppKTP	Alluxa	100		94.708	94.685	0.031

Table 6.1: **Resulting spectral purity estimations.** The result of spectral purity estimation of the heralded photons from the JSI for each crystal and filter combination measured. The simulated purity column represents the mean value calculated by Monte-Carlo simulation of the JSI for each case with the standard deviation from the samples providing us a means to quantify the error present in the measurement.

$$M_{\text{JSI}} = \Omega_i \cdot D_\kappa \cdot \Omega_s. \tag{6.4}$$

Where M_{JSI} is our measured JSI, $\Omega_{i,s}$ are our orthogonal matrices for idler and signal frequencies respectively and D_κ is our diagonal matrix of Schmidt magnitudes, from which we can estimate the spectral purity. The columns of $\Omega_{i,s}$ represent the frequency modes for both the signal and idler photons.

The calculated purities from our measured JSIs can be seen in table 6.1. We can see how our measurements compare to the theoretical values for each crystal (and filter combination). For the ppKTP crystal we can see that when filtered both the theory and experiment align very closely in their values however without filtering we see quite a large discrepancy between theory and measurement. The difference seen here is likely due to some degree of spectral filtering present in the configuration of the sources that exists outside of filters placed on the couplers used for the signal and idler modes causing an increase in the measured purity. In the case of the Gaussian crystal, our measurements result in a slightly lower purity estimation however we can see from the difference produced by including some filtering that there must exist some extra correlations that have not been removed entirely from the photon

generation process. Finally, the antisymmetric crystals see very close agreement with the theoretical value presenting the closest estimate when compared to the theory out of all of the measurements.

6.6   Error Analysis in JSI Reconstruction

JSI measurements have been used in the community for more than a decade now [144–149, 153], with dispersive spectroscopy drastically improving the quality of characterisation in recent years. However, one thing that is consistently been passed over in the literature is that of proper error analysis of benchmarks like purity calculated from the observed joint spectra. We will now address this simulating reconstructed JSI through Monte-Carlo sampling, matching the JSI's statistics so that we can perform purity estimations on each simulated reconstruction providing us insight into the error existing within each measurement. The first feature to consider is the amount of data required to obtain reliable statistics. As our group showed in [7] a reliable Schmidt mode estimation, based on Monte-Carlo methods, requires $\approx$ 50k detection events at least (accumulated over the spectral window). Our timing resolution is quite high, therefore we have small time bins and overall a low amount of data per time bin. In addition, the specific way we record two-photon counts (using an auxiliary PDC source for timing) or indeed the 4-photon counts, which are always low, plus the fact that we add significant loss in our 20 km fibres, means we have to integrate over long times.

The volume of the data required can be seen in fig. 6.20, due to the 1 ps binning resolution and the existence of the spectra over a relatively small span of wavelengths the distance between data points is quite large. This presents the need to operate most (all) of the analysis in the sparse regime. The use of sparse matrices makes for a more computational efficient task, however due to the dimensions of the matrices some operations are naturally still time consuming. Sparse matrices allow us to perform the SVD without having to reduce our spectral resolution letting us maintain our 1 ps square time bins. One of the effects of this sparsity is the need to re-bin the data to reduce the resolution in order to display the result of the measurements.
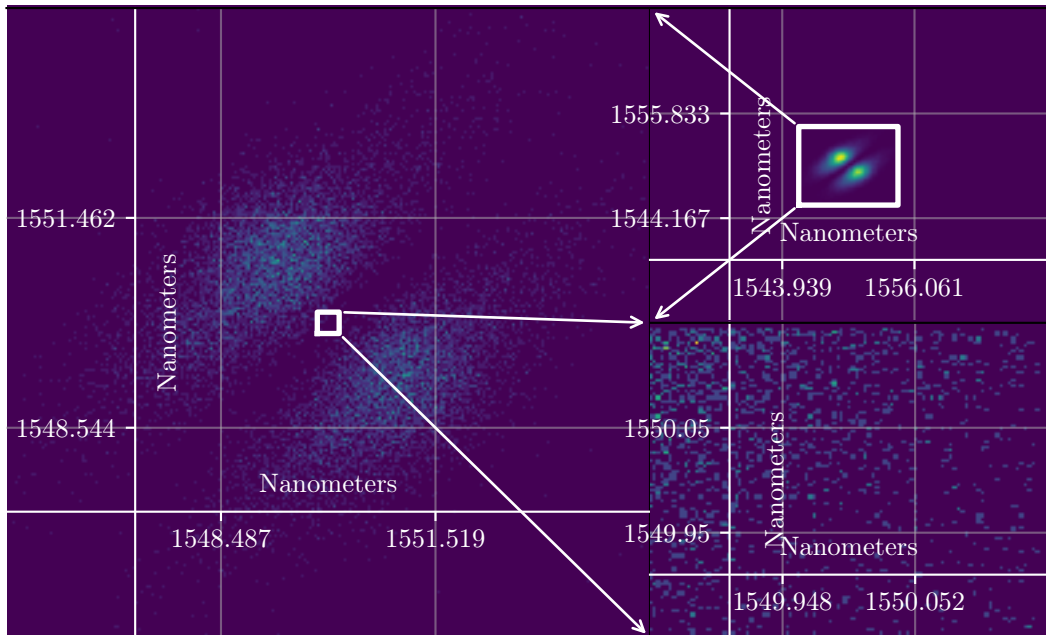
Figure 6.20: **Sparsity of correlations in reconstructed JSI measurements.** To clearly illustrate the sparsity of the measured data we can move from the upper right sub-plot anticlockwise. First we see the typical JSI plot shown so far displaying the result across an entire pulse period of the pump laser. Next we can see the same measurement but zoomed in further (at $\approx \pm 1.5 nm$ from the centre), the granularity and distance between data points begins to become more apparent here. Finally, we can see an even smaller section (at $\approx \pm 0.05 nm$ from the centre), at this depth we can see how much of the data is in fact empty, illustrating our need to view the data with bins larger than the device resolution of 1 ps.

6.6.1   Jitter and the Instrument Response Function

Sources of jitter can be found throughout experiments like this with random variations being produced from the pump laser, the detectors and finally the timing electronics (section 5.1). Whilst some sources will cause larger problems than others, a large amount of jitter from the pump laser could provide issues in the extremes of the JSI where the ppKTP side lobes extend very far out, limiting our maximal range because the peak-to-peak distance between each pulse can become shorter. Fortunately it is common to operate pulsed pump laser with a repetition rate in the order of tens of MHz making this contribution small. However this can be mostly dealt with given that we are only looking for correlations produced from single-photon emissions from a single pulse. The random variation induced by the output pulses of the detector combined with that of the timing logic is likely to be our main

source of jitter in the experiment, fortunately the use of timing electronics designed to employ constant-fraction discrimination (section 5.1.1) allows us to negate a large amount of variation produced by the detectors themselves.

Regardless of the source of jitter it is important for us to quantify how much of it is present. This is a relatively simple task to complete due to having such a fine timing resolution as this allows us to measure the range over which coincidence events can be found with respect to a single pulse of the pump laser. In taking this measurement we can produce a histogram of the arrival times centred around a clock signal, from here it is a simple matter of measuring the FWHM of the peak and taking the square root. This simple method is ideal for 2 or more of the detector channels allowing us to build up the total amount present however we need to adjust this slightly to work for a single channel. In the single-channel case we can instead look to measuring coincidence events on the same channel but across 2 pulses, we look for coincidence events on one channel but each event must be separated by the repetition rate of the laser. We should note that this doesn't allow us to separate the individual contributions from the laser or the detectors alone instead resulting in a measurement of total system jitter (where the system is inclusive of the number of channels)[2]. It should also be noted that measurements of jitter can be produced from the same dataset as that used to produce the joint spectra as all of the time tags are stored for post processing.

The instrument response function (IRF) provides a way in which to capture the error present in the system. We can measure the IRF simply by making use of the setup detailed in figs. 6.4 and 6.15 with the delay fibres removed. The removal of the dispersive fibres here is key, as we wish to measure the subtle changes provided by the pump laser along with the jitter present in the detectors and timing logic. The IRF for our fibre spectrometer is shown in fig. 6.21. The triangular shape arises from the convolution of the marginal spectra with the equivalent for spectra for the clock signal which in the experimental configurations shown will posses the same shape as either the signal or idler. As discussed in section 6.6.1 we acknowledge that our detection is not perfect and the behaviour of each detector channel will influence the shape of the measured joint spectrum.

---

[2]When referring to the system here we mean the source, detector and timing electronics for the given channel or group of channels in question
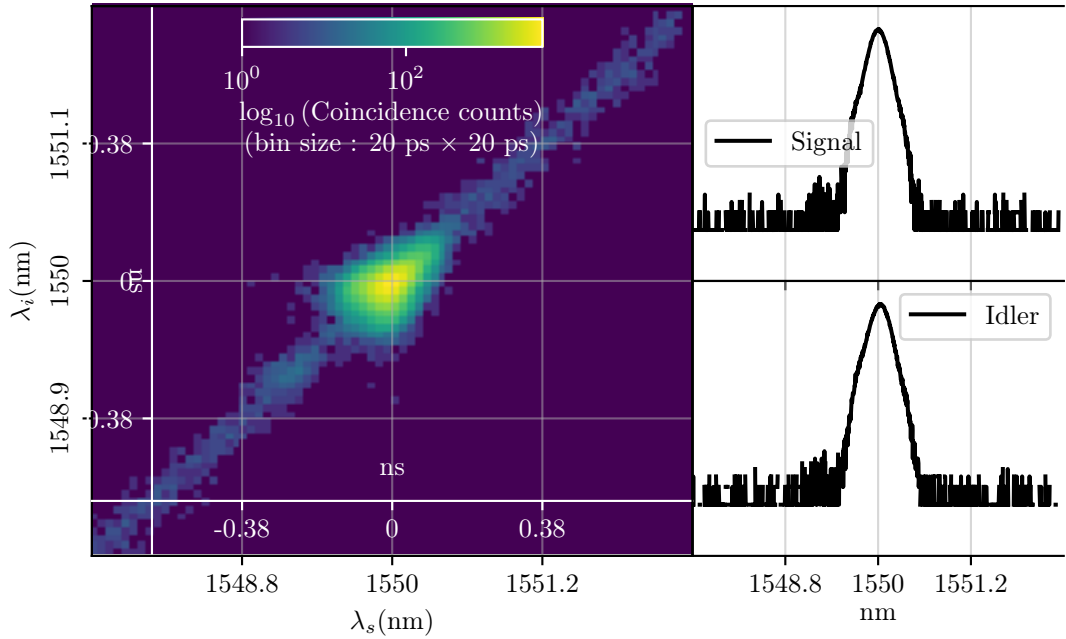
Figure 6.21: **The instrument response function of the dispersive spectrometer.** By measuring the arrival times of photons without the dispersive fibres in place we can measure the timing jitter across all of the detector channels simultaneously, by the combining the arrival times for both channels the instrument response function can be reconstructed.

6.6.2 Simulation of JSI Reconstruction via Monte-Carlo Method

The numerical nature of the SVD process results in analytical error propagation that is non-trivial. We therefore use Monte-Carlo methods similar to those used for quantum state tomography instead. Fortunately, where single photons are concerned, we can make use of the fact that they obey Poissonian statistics. Armed with this knowledge we can develop a method to simulate new measurements and determine how much error is present.

First we must make the assumption that our measurement is suitably close to the true mean of the experiment[3] and that all the data points obey Poissonian statistics[4]. In deciding that each measurement exists by itself as a single repetition and is suitably close to the true mean the experiment would converge onto given enough time we can generate virtual results for the experiment to get an estimation for the error. To generate each virtual result we treat each point of the raw (un-

---

[3]We consider this a valid assumption provided that we have gathered enough data points to encapsulate the full effects of the statistical distribution present in the data.

[4]For single photon sources this assumption is considered valid.

binned) JSI as the mean value of a Poissonian distribution and randomly sample from it. After generating a full joint spectra we can then calculate the resulting purity of the simulation. With this sampling process in place we can generate as many synthetic measurements as we need stopping once the standard deviation across the purity values converges. We choose the standard deviation as a method to determine the stopping point of the estimation process as once it becomes constant it should be safe to assume that enough of the system's probability distribution has been captured to have enough confidence in the result.
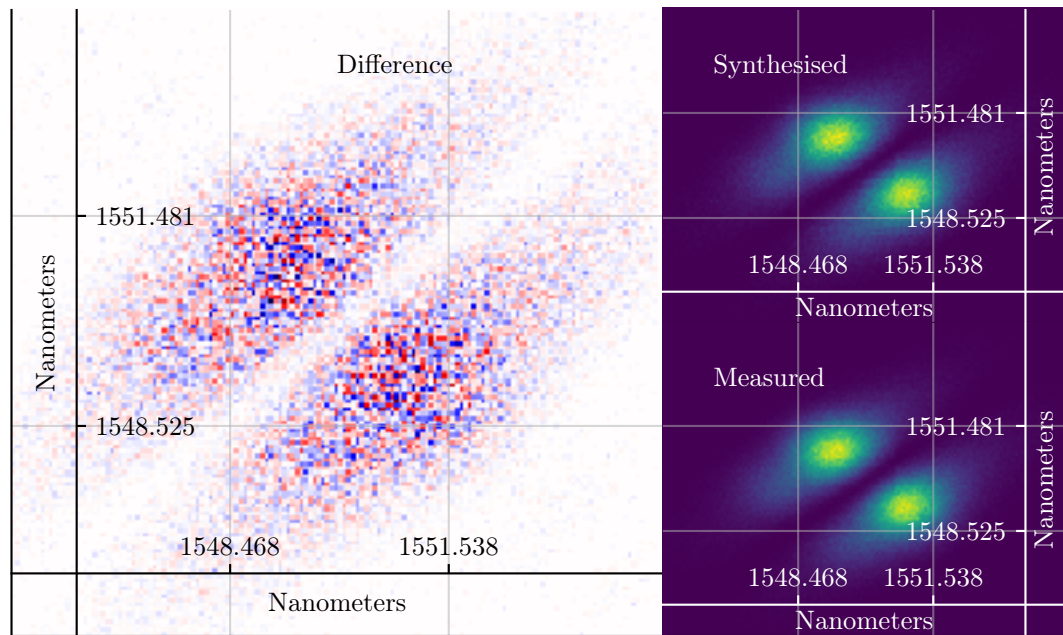
Figure 6.22: **From left to right: measured joint spectrum, simulated joint spectrum, the difference between measured and simulated.** The simulated data generated for the error analysis provides a close match to that of the measured data as can be seen with the similarity between both data sets. This similarity can be seen further in the subtractive plot, the appearance of noise here points towards the simulated data having the structure we wish to obtain. Each plot has here has been clipped to cover ≈-1.5 ps to ≈1.5 ps from the centre of the spectra to fully illustrate the difference present. The red and blue elements represent where the simulated JSI has more or less counts than the measurement.

A general result of our sampling method is detailed in fig. 6.22 making it clear the difference in the "Measured" and "Synthesised" data in the "Difference" panel. Of note, it should be made clear that the "Measured" and "Simulated" panels look almost identical due to the rebinning of the data points needed to make the plot clear. The "noisy" appearance of the difference plot points towards the effects of randomly

sampling Poissonian distribution employed in the simulation process providing a means to deviate from the mean value and with this deviation determine the degree of error present. With evidence that our method is capable of producing new samples based upon our measurement we can now move to applying it to all of the crystals we have tested so far and in the case of the antisymmetric crystals we focus solely on the 2-photon case.
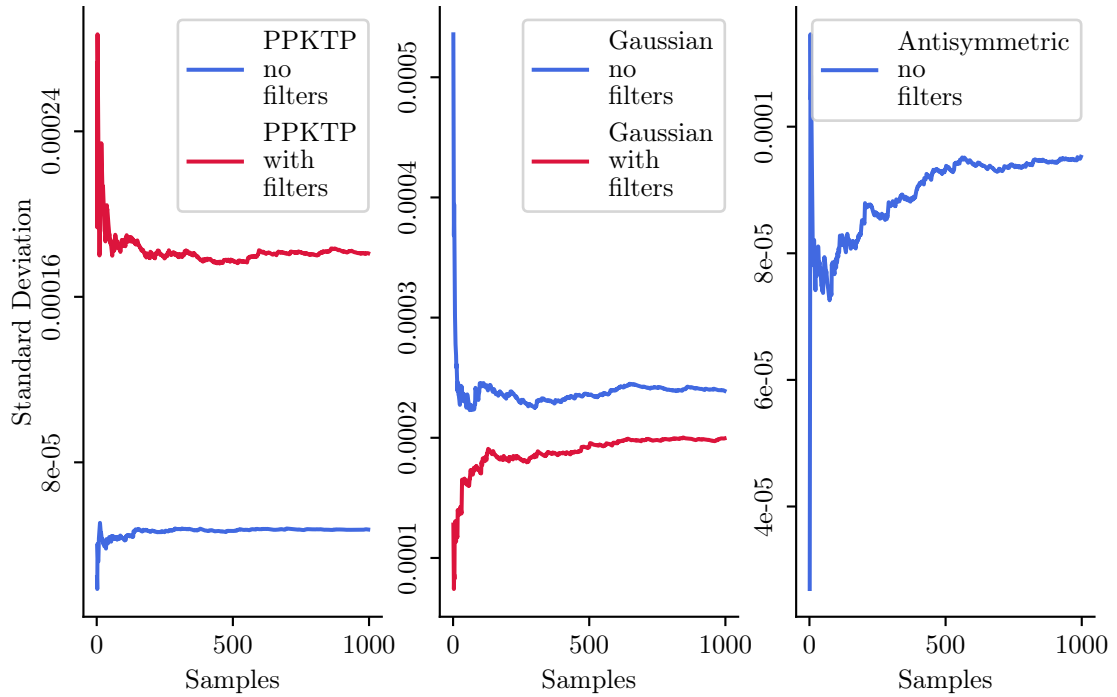
Figure 6.23: **Convergence of standard deviation of purities estimated from simulated JSIs.** To determine whether or not enough of the measurements statistics have been encapsulated in each simulation we need the standard deviation to converge onto a single value. For each measurement we find that 1000 simulations (where each simulation results in a single sample for error calculation) allows for convergence, seen here as the gradient of each plot reaching zero.

For each sample produced with this method we calculate the resulting purity, the standard deviation of which is expected to converge after a large enough number of samples have been generated.

Chapter 7

Improving Purity Estimation

7.1 Introduction
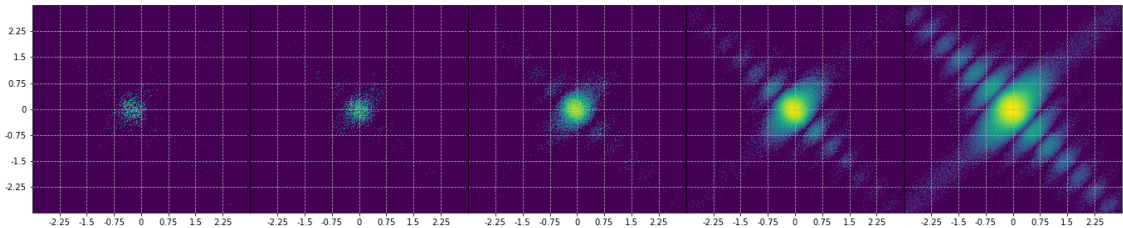
Figure 7.1: **Extent of different measurement acquisition times on the ability to reconstruct the JSI.** Varying the acquisition time used to reconstruct the JSI of an unfiltered ppKTP crystal we can see how much data is required to resolve the details in the joint spectrum. However, do we measure for too long and include measurement drift in our final estimations and since there is the possibility to measure the instrument response function of the spectrometer can we use it in some capacity to improve our estimations at shorter acquisition time?

Having now collected and analysed our measurements to derive an estimation of the purity of each crystals biphoton state along with using a Monte-Carlo based method to calculate values for the errors in each of our measurements we now ask ourselves if it is possible to improve our estimations through image processing. Here we determine whether it possible to achieve better timing resolution or produce equivalent purity estimations for different performing detectors and if we can use less data for the estimations. With each measurement operating for anywhere between a few hours to a few days it may be possible that the components of the experiment have drifted away from their initial positions. This drift could manifest itself in the likes of the fibre couplers moving ever so slightly out of alignment leading to an

overall reduction in the detected rates, an instability in the temperature of the crystal causing a change in the output wavelengths or finally, changes in the temperature of the optical fibre used in the delay lines providing a change in the length and so the amount of dispersion we expect.

In the case of the couplers moving away from their optimal position it would be possible to observe from the stored time tags a reduction in both the single channel and coincidence detection rates. Whilst a reduction here isn't desirable it also doesn't concern us too much, an of equal concern is the polarisation controllers needed before the detectors (our detectors are polarisation dependent) moving away from their set position. Change from either will result in loss of detection events however both cases can be detected in the detection rates observed leaving us the option of monitoring the experiment and making slight adjustments as it proceeds, breaking it up into smaller sections. Given the length of each measurement this was a consideration already made with the condition that if the detection rates at the start of each section were the same then the experimental configuration between each section must be similar enough.

More concerning would be changes caused to the wavelengths of the photons caused either by changes at the crystal, due to the temperature dependence of the emission wavelengths in the down conversion process, or by a change in the length of the delay line fibre again caused by a temperature dependence with the laboratory's ambient temperature. Change in the crystal temperature is a feature we already account by placing each crystal inside a temperature controlled oven ensuring we keep each crystal at its degenerate temperature ensuring the emission is at the desired wavelength for both the signal and idler modes. However, change in the fibre length, and so the amount of dispersion experienced by each photon is harder to compensate for, to do this we would need to place each of the fibres in their own temperature controlled environment or if we know how much change exists we could create calibration curves to account for the change on demand. Isolating the fibres is the more convenient of the two options and should help with ensuring the amount of dispersion remains constant.

Given the length of the measurements we have the ability to scan across the length of the recorded data and determine if there exists a point where we drift away

from the initial conditions far enough that it begins to result in a larger distance between the theoretical and estimated purity values. If this is the case then there could exist a shorter measurement time for each crystal where we see a better purity estimation and provided the errors calculated at this new shorter measurement time and sufficiently small we should use the value calculated here instead.

7.2 Variable Acquisition Time

For each crystal we now reconstruct the JSI and estimate the purity at different measurement times by only using the desired amount of recorded data. Initially, the effects of this can be seen in fig. 7.1, as we would expect the number of data points present in the JSI are much fewer at low measurement times to high measurement times, however at some intermediate measurement time can we calculate an estimation that is closer to the theory.
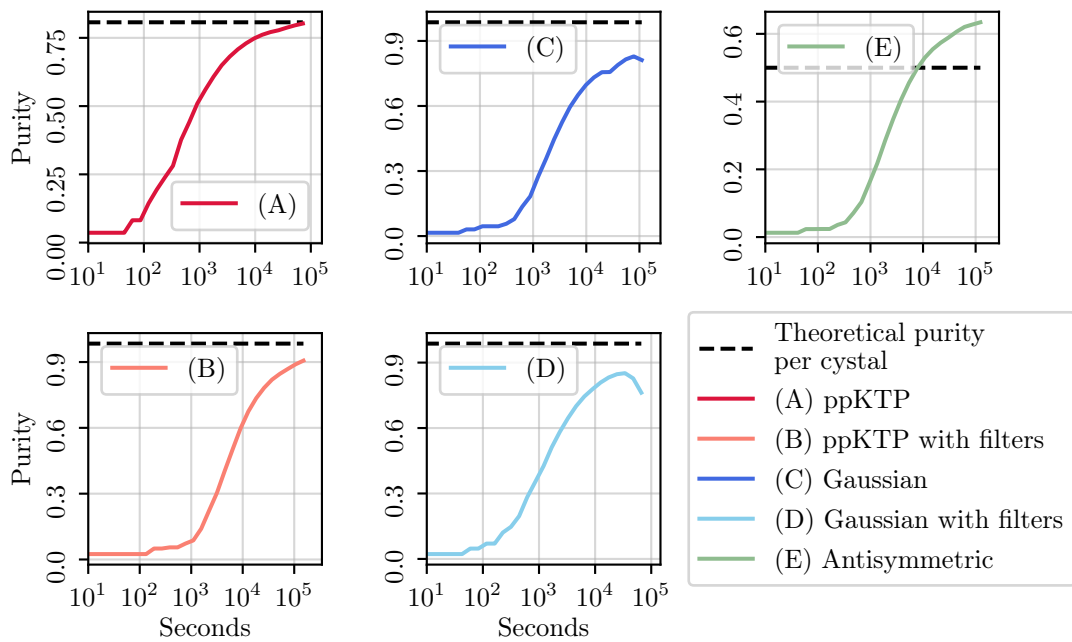
Figure 7.2: **Purity estimations for each crystal with their respective theoretical purity values for different acquisition times.** By changing the length of the acquisition time used to reconstruct the JSI and estimate the purity we can observe the performance of each measurement as a function of time with the goal of determining whether or not we should shorten the acquisition time used to report the measured purity in each case.

Each of the measurements shown in fig. 7.2 show measurement behaviour as

we would expect, that is, as measurement time is increased the estimated purity gets closer to the expected value (the theoretical purity). It can be seen though, for example the filtered Gaussian measurement, that more optimal acquisition times may exist as the purity here can be seen to decrease and diverge from the theoretical value. This suggests that some drift may be present in these measurement and that it is perhaps better to calculate the purity at the point for each line that is closest to its respective theoretical purity. Making the choice to reduce the acquisition time is however dependent on the error present in the measurement at this point. We can also see a similar trend in the Gaussian crystal however in this case both of the lines continue to trend towards the theoretical value although we do see some over estimation.

7.3 Application of Image Deconvolution
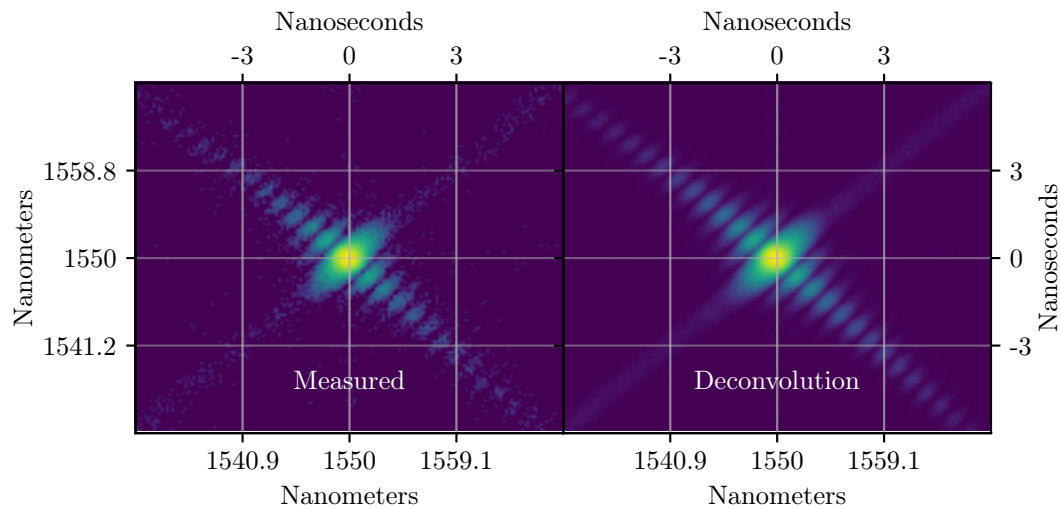
Figure 7.3: **Application of the Richardson-Lucy deconvolution algorithm to JSI reconstruction.** In the case of this ppKTP measurement deconvolution also allows for more of the side lobes to be resolved when displaying the $\log_{10}$ of each value. This visual indication of the enhancement in the reconstruction suggests that it may allow for better purity estimation due to better resolution of the complete structure.

Since we may find a shorter acquisition time that allows for a more accurate purity estimation (assuming the simulated error is small enough) and since we have measured the instrument response function (IRF) of the spectrometer we can explore

Crystal	Filtering	Bin Width (ps)	Theoretical Purity ($\sqrt{JSI}$)	$p\left(|\sqrt{JSI}|\right)$	$p\left(|\sqrt{JSI_{Deconvolved}}|\right)$
hline Antisymmetric	None	1		44.130	57.111
Antisymmetric	None	20	50.000	65.279	59.252
Antisymmetric	None	50		65.844	62.191
Antisymmetric	None	100		66.978	66.638
Gaussian	None	1		57.881	66.280
Gaussian	None	20	98.600	84.428	67.704
Gaussian	None	50		84.753	69.619
Gaussian	None	100		85.011	72.187
Gaussian	Semrock	1		59.214	74.459
Gaussian	Semrock	20	98.697	90.945	76.036
Gaussian	Semrock	50		91.227	78.123
Gaussian	Semrock	100		91.404	80.967
ppKTP	None	1		65.880	61.993
ppKTP	None	20	80.701	82.038	64.153
ppKTP	None	50		82.407	67.287
ppKTP	None	100		82.880	72.706
ppKTP	Alluxa	1		45.350	83.239
ppKTP	Alluxa	20	98.397	94.115	85.693
ppKTP	Alluxa	50		94.490	88.597
ppKTP	Alluxa	100		94.708	92.321

Table 7.1: **Result of deconvolution assisted purity estimation.** The addition of a deconvolution on the reconstructed JSI for each of the crystal and filter combinations measured results in estimations greater than both the theoretical values and those direct from the measurements. However in each case shown here the addition of deconvolution still results in an estimate further away from the theory than we would like.

the possibility of achieving better purity estimation with even shorter measurement time. Deconvolution is the process of enhancing or recovering a signal from data operating under the assumption the data to recover is a pure signal distorted by a filter of some kind. In our case this allows us to treat the reconstructed JSI as an image and use our IRF as a representation of the filter that distorts the underlying pure signal. The deconvolution algorithm used here is that of Richardson-Lucy [164, 165], this method iteratively recovers the pure signal from the JSI using the IRF. This is a method frequently used for recovering photographs due to its rooting in Poissonian statistics making it particularly suitable to our needs thanks to our measurement containing the same governing statistics. For the application of this we do have to work under the assumption that the measured IRF enacts a convolution on the measurement, since the IRF is a feature of the jitter present in the detectors used we consider this a valid assumption.

[p]

Initially our results in table 7.1 show only an increase in the estimated purities for each crystal and filter combination when compared to values measured with at maximum acquisition time, however, as seen previously in fig. 7.2 it may be

beneficial to perform the calculation from a shorter form of the measurement. Next we combine both variable acquisition time and deconvolution in the hope we can achieve a better purity estimation at a shorter acquisition time. From fig. 7.4 we see that with deconvolution it is possible to get closer to the theoretical values for purity in most cases however we also see that it exacerbates the estimations at longer acquisition time that are further away from the theory predictions.
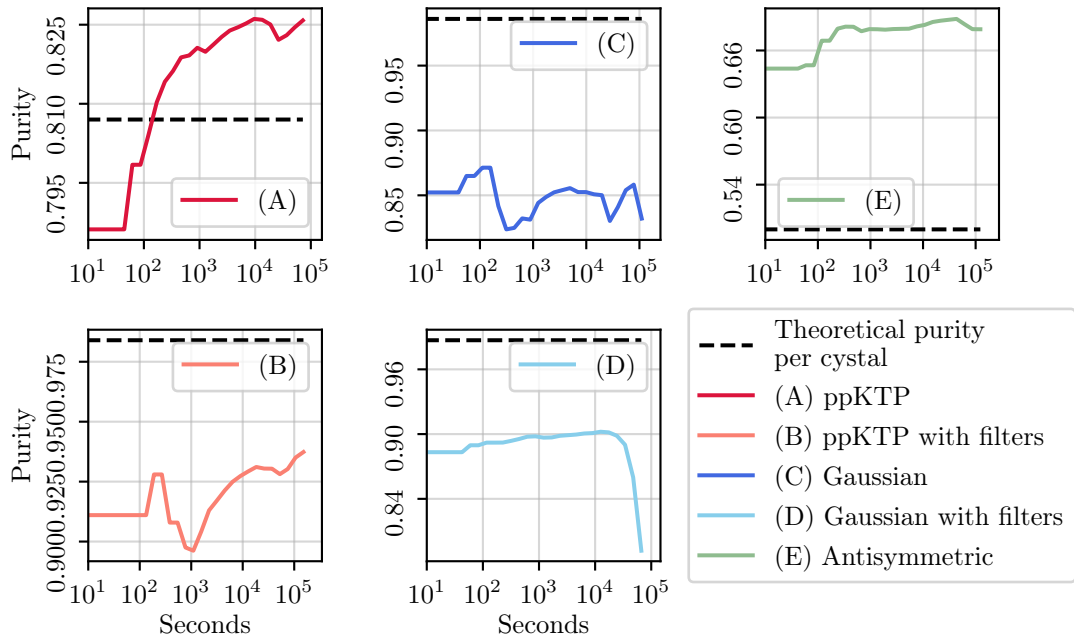
Figure 7.4: **Result of purity estimation on the deconvolution of reconstructed JSI measurements.** Here we see that application of deconvolution of the JSI with the IRF allows in general for quicker estimation of the single-photon purity.

This results bodes well for deconvolution with the IRF of a reconstructed JSI measurement, implying that it should be possible from our measurements to iteratively find an optimal acquisition time where we balance both the precision of the estimation that can be achieved with the accuracy found from the simulated error calculations. The Gaussian crystal is designed with the intent of producing a single central lobe which from the theory should result in a purity close to 1. Again we see for the filtered Gaussian crystal measurement that at long acquisition times the purity degrades and deviates further away from the theoretical value, given that this is present in both fig. 7.2 and fig. 7.4 this is likely to do with some error present in the experimental configuration, for example the width of the pump pulses could

have drifted away from the measurements initial conditions. We can see from fig. 7.4 for both filtered and unfiltered measurements that an increase is possible however we also see degradation in the estimates for both ppKTP measurements suggesting that the deconvolution process is not always ideal as over estimation appears to be increased.
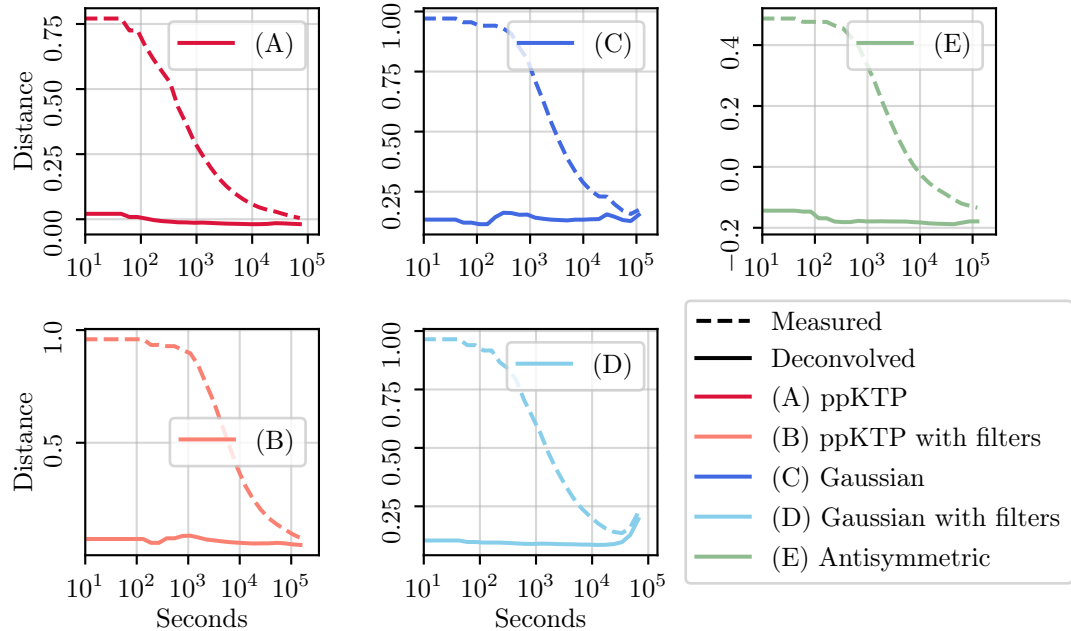
Figure 7.5: **Distance between purity estimations with and without deconvolution and theoretical values.** Comparing the distance of the estimated purity, Distance $= p_{\text{theory}} - p_{\text{estimate}}$, with acquisition time shows the potential that deconvolution of the JSI with the IRF presents for purity estimation allowing for estimates to be made closer to the theoretical values on shorter measurements. This potential to assist in purity measurement should be considered carefully as these shorter measurement lengths are also subject to larger errors.

In fig. 7.5 the purity estimations for both the raw measurement and deconvolved measured are shown on the same set of axes, the degree in improvement in the estimation can be clearly seen when applying deconvolution to the measurement. This is a clear demonstration that the image processing shown here provide significant improvement in purity estimations for shorter measurements. Whilst at long measurement times application of deconvolution may not be strictly necessary, it proves itself as a useful addition for shorter measurements.

7.4 Comparing the Effect of Different Detector Jitter
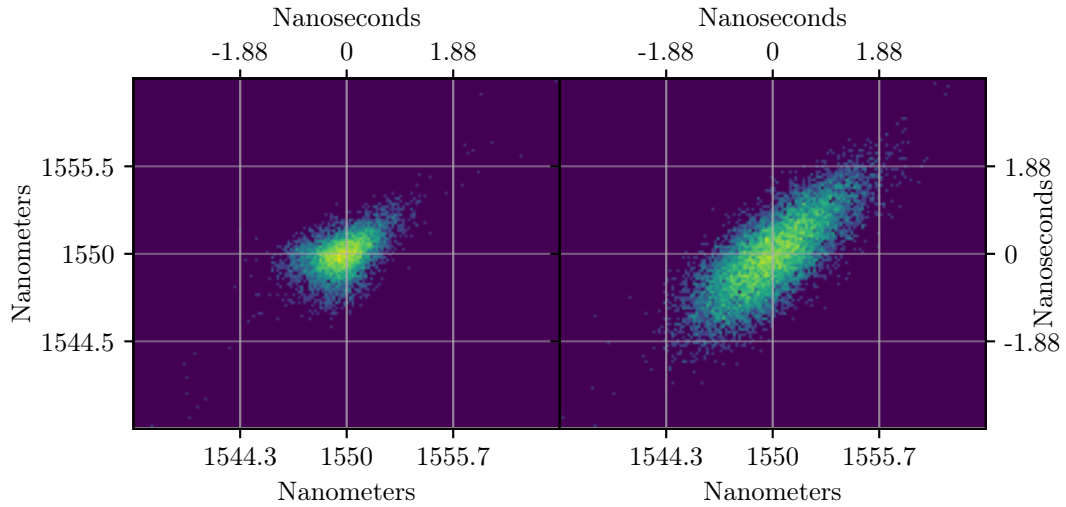
Figure 7.6: **Instrument response functions of two detectors with different timing jitter.** The IRF displayed here are for "low" (left panel) and "high" (right panel) jitter detectors, whilst the jitter for each are ≈ 25 ps and ≈ 50 ps when considering just a single detector, the combination of the multiple channels needed to form our measurements results in these distributions. The "low" jitter detectors exhibit a smaller and more compact distribution whereas the "high" jitter detectors show a broader and more round distribution, the effect these shapes have on the performance of the purity estimation requires further exploration.

Deconvolution allows us to achieve better estimations of purity in general by restoring missing information held within the signal, this is the reason as to why we generally see improved estimation at shorter acquisition times where our measurements contain less data points. The IRF used to deconvolve the measurement encapsulates the error present in the measurement and experimental hardware, in particular the jitter present in the detectors. Given that the IRF describes the error present at each point in the measurement along with how that error is distributed to the surrounding data points are the same improvements available with detectors with an increased jitter compared to those we have used so far. Each measurement presented thus far has been accomplished with a detector jitter of ≈ 25 ps, we now turn to completing purity estimation with a detector jitter of ≈ 50 ps. In fig. 7.6 we see the reconstructed IRF for detectors at both jitters, it is clear that a doubling in jitter on each detector channel has a significant impact on the shape and size of the

response function. If the measured IRF does in fact encapsulate enough of the error present in the measurement and the instrumentation then it should be possible to achieve an improvement in estimation.
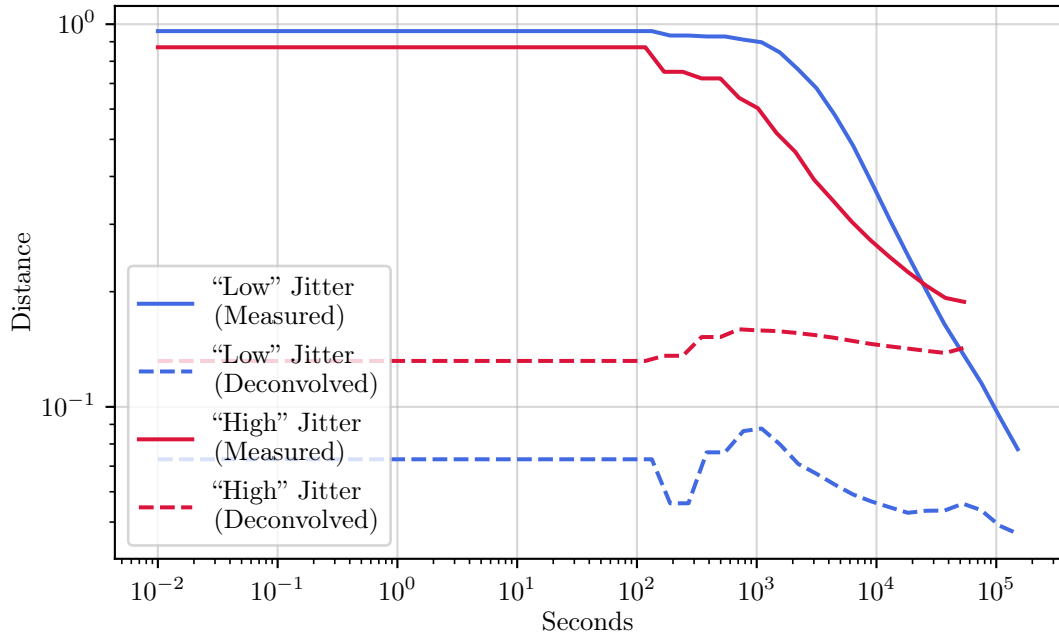
Figure 7.7: **Purity estimation comparison between different detector performance.** Increased detector jitter in general results in purity estimations further away from the theoretical values. We can see that in the case of our detectors with jitters of $\approx 25ps$ and $\approx 50ps$ for "low" and "high" cases respectively that a halving in jitter results in closer purity estimation at low acquisition times. Further it is shown that application of deconvolution in the "high" jitter case allows for purity estimations closer to the theory than the "low" jitter case without deconvolution clearly displaying the potential there is for the application of image processing methods on JSI measurement.

From previous measurements we see the tendency for deconvolution to improve the purity estimation at short acquisition times before the volume of data becomes large enough for the Schmidt decomposition (via SVD) to become effective without prior deconvolution. For photons emitted ppKTP crystal, filtered in order to block the side lobes isolating the central peak, we compare purity estimations across a range of acquisition times for both detectors with and without the addition of deconvolution. As a figure of merit for each case we plot in fig. 7.7 the distance between the estimation and the theoretical value to determine the effectiveness of each case. We see that for both detectors and short acquisition time that employing deconvolution results in estimations of purity close to the theoretical value. What

is clear from fig. 7.7 is that regardless of detector performance, assuming that the jitter is smaller than the width of the central peak in the JSI, deconvolution can successfully improve the estimated purity. This technique could be included during the measurement phase along with the error estimation displayed in section 6.6 to shorten the overall measurement time once a small enough tolerance for the error is achieved with deconvolution providing an increase in the accuracy of the estimation.

Chapter 8

Conclusion

The goal of this thesis was to develop a state-of-the-art multi-photon experiment at telecom wavelengths. In order to support that, advanced modelling and processing techniques needed to be developed. This included a pair of models for the generation and detection of single photons, the methods to analyse produced photons. Further a method to reconstruct the JSI of photons produced from a PDC based single-photon source using the analysis methods developed has been constructed in order to estimate the spectral purity of the heralded single-photons emitted. Finally, image deconvolution techniques have been used to improve purity estimations.

These tools, together with the work done by our group to engineer PDC crystal nonlinearities, provide a set of tools to design and characterise PDC sources. The modelling undertaken allows us a convenient method to assess the signal-to-noise ratio performance of a number of sources along with accounting for loss present for the situation they are used. By applying a global sensitivity analysis method to our combinatorial model we have confirmed the benefit in operating the clock of the pump laser significantly faster than the detector reset time. Further, this model could be extended to include the fidelity of heralded single photons providing us with more insight into source performance.

The TCSPC toolkit developed has proven to be both powerful and flexible as we have been able to reconstruct JSI from time-of-flight measurements as well as its use in our quantum conference key experiment [5] to find the first instance of a measurement. The potential for extensions remains, for example, the inclusion of a method for finding detection patterns between different pieces of time tagging

hardware regardless of their specific model would benefit further quantum key distribution experiments.

Finally, our spectral purity measurements from JSI reconstructions and subsequent use of image processing techniques to explore the improvements to purity estimations. For future measurements of spectral purity via JSI reconstruction the reconstruction and deconvolution steps could be calculate whilst the time-of-flight measurement is being recorded. In doing so we would quickly gain an estimation for the spectral purity and sooner identify whether the measurement is successful. Further, if the error analysis can be included into this step, the entire measurement time could be shortened significantly. This of course hinges on Richardson-Lucy being the most ideal method for deconvolution, further work into deconvolution methods and other image reconstruction methods could yield a means to more accurately estimate spectral purity from short measurement times. Further, other deconvolution methods may prove to be better suited the real-time application of JSI reconstruction via time-of-flight spectroscopy. For example, a method relying more heavily on a fourier transform based process may be able to both, make use of available computational hardware more efficiently or possible provide useful insight into the effects of the measured spectra and the associated instrument response function of the spectrometer.

In short, we have developed the means of evaluating the signal-to-noise performance of single-photon sources considering their performance in the resulting states number space, determining that operating our sources at a desired signal-to-noise ratio with a clock period shorter than the detector reset time is ideal. Followed by developing an experimental configuration to measure the joint spectrum of heralded signal-photon sources such that the purity of the resulting single-photons can be estimated. In using both of these methods the signal-to-noise characteristics and spectrum of the photons can be estimated accurately providing us with further tools to engineer single-photon sources with higher brightness and spectral purity.

Bibliography

[1] M. Proietti, A. Pickston, F. Graffitti, P. Barrow, D. Kundys, C. Branciard, M. Ringbauer, and A. Fedrizzi, *Experimental test of local observer independence,* Science Advances **5** (2019).

[2] M. Proietti, M. Ringbauer, F. Graffitti, P. Barrow, A. Pickston, D. Kundys, D. Cavalcanti, L. Aolita, R. Chaves, and A. Fedrizzi, *Enhanced Multiqubit Phase Estimation in Noisy Environments by Local Encoding,* Physical Review Letters **123** (2019) 180503.

[3] F. Graffitti, A. Pickston, P. Barrow, M. Proietti, D. Kundys, D. Rosset, M. Ringbauer, and A. Fedrizzi, *Measurement-Device-Independent Verification of Quantum Channels,* Physical Review Letters **124** (2020) 010503.

[4] F. Shahandeh, M. Ringbauer, M. Proietti, F. Costa, A. P. Lund, F. Graffitti, P. Barrow, A. Pickston, D. Kundys, T. C. Ralph, and A. Fedrizzi. *Assisted Macroscopic Quantumness,* 2017.

[5] M. Proietti, J. Ho, F. Grasselli, P. Barrow, M. Malik, and A. Fedrizzi. *Experimental quantum conference key agreement,* 2020.

[6] F. Graffitti, P. Barrow, M. Proietti, D. Kundys, and A. Fedrizzi, *Independent high-purity photons created in domain-engineered crystals,* Optica **5** (2018) 514.

[7] F. Graffitti, P. Barrow, A. Pickston, A. M. Bra ńczyk, and A. Fedrizzi, *Direct Generation of Tailored Pulse-Mode Entanglement,* Physical Review Letters **124** (2020) 053603.

[8] E. Knill, R. Laflamme, and G. J. Milburn, *A scheme for efficient quantum computation with linear optics,* Nature **409** (2001) 46.

[9] H. J. Briegel and R. Raussendorf, *Persistent Entanglement in Arrays of Interacting Particles,* Physical Review Letters **86** (2001) 910.

[10] J. F. Clauser, *Experimental distinction between the quantum and classical field-theoretic predictions for the photoelectric effect,* Physcal Review D **9** (1974) 853.

[11] X. Brokmann, E. Giacobino, M. Dahan, and J. P. Hermier, *Highly efficient triggered emission of single photons by colloidal CdSeZnS nanocrystals,* Applied Physics Letters **85** (2004) 712.

[12] A. J. Bennett, D. C. Unitt, P. Atkinson, D. A. Ritchie, and A. J. Shields, *High performance single photon sources from photolithographically defined pillar microcavities,* Opt. Express **13** (2005) 50.

[13] A. Beveratos, R. Brouri, T. Gacoin, A. Villing, J.-P. Poizat, and P. Grangier, *Single Photon Quantum Cryptography,* Physical Review Letters **89** (2002) 187901.

[14] J. McKeever, A. Boca, A. D. Boozer, R. Miller, J. R. Buck, A. Kuzmich, and H. J. Kimble, *Deterministic Generation of Single Photons from One Atom Trapped in a Cavity,* Science **303** (2004) 1992.

[15] M. Hijlkema, B. Weber, H. P. Specht, S. C. Webster, A. Kuhn, and G. Rempe, *A single-photon server with just one atom,* Nature Physics **3** (2007) 253.

[16] M. Keller, B. Lange, K. Hayasaka, W. Lange, and H. Walther, *Continuous generation of single photons with controlled waveform in an ion-trap cavity system,* Nature **431** (2004) 1075.

[17] S. Lukishova, A. Schmid, A. McNamara, R. Boyd, and C. Stroud, *Room temperature single-photon source: single-dye molecule fluorescence in liquid crystal host,* IEEE Journal of Selected Topics in Quantum Electronics **9** (2003) 1512.

[18] R. Alléaume, F. Treussart, J.-M. Courty, and J.-F. Roch, *Photon statistics characterization of a single-photon source,* New Journal of Physics **6** (2004) 85.

[19] H. Wang, Y.-M. He, T.-H. Chung, H. Hu, Y. Yu, S. Chen, X. Ding, M.-C. Chen, J. Qin, X. Yang, R.-Z. Liu, Z.-C. Duan, J.-P. Li, S. Gerhardt, K. Winkler, J. Jurkat, L.-J. Wang, N. Gregersen, Y.-H. Huo, Q. Dai, S. Yu, S. Höfling, C.-Y. Lu, and J.-W. Pan, *Towards optimal single-photon sources from polarized microcavities,* Nature Photonics **13** (2019) 770.

[20] H. Wang, H. Hu, T.-H. Chung, J. Qin, X. Yang, J.-P. Li, R.-Z. Liu, H.-S. Zhong, Y.-M. He, X. Ding, Y.-H. Deng, Q. Dai, Y.-H. Huo, S. Höfling, C.-Y. Lu, and J.-W. Pan, *On-Demand Semiconductor Source of Entangled Photons Which Simultaneously Has High Fidelity, Efficiency, and Indistinguishability,* Physical Review Letters **122** (2019) 113602.

[21] O. Gazzano, S. Michaelis de Vasconcellos, C. Arnold, A. Nowak, E. Galopin, I. Sagnes, L. Lanco, A. Lemaître, and P. Senellart, *Bright solid-state sources of indistinguishable single photons,* Nature Communications **4** (2013) 1425.

[22] L. Schweickert, K. D. Jöns, K. D. Zeuner, S. F. Covre da Silva, H. Huang, T. Lettner, M. Reindl, J. Zichi, R. Trotta, A. Rastelli, and V. Zwiller, *On-demand generation of background-free single photons from a solid-state source,* Applied Physics Letters **112** (2018) 093106.

[23] N. Somaschi, V. Giesz, L. De Santis, J. C. Loredo, M. P. Almeida, G. Hornecker, S. L. Portalupi, T. Grange, C. Antón, J. Demory, C. Gómez, I. Sagnes, N. D. Lanzillotti-Kimura, A. Lemaítre, A. Auffeves, A. G. White, L. Lanco, and P. Senellart, *Near-optimal single-photon sources in the solid state,* Nature Photonics **10** (2016) 340.

[24] H. Wang, J. Qin, X. Ding, M.-C. Chen, S. Chen, X. You, Y.-M. He, X. Jiang, L. You, Z. Wang, C. Schneider, J. J. Renema, S. Höfling, C.-Y. Lu, and J.-W. Pan, *Boson Sampling with 20 Input Photons and a 60-Mode Interferometer in a 10^{14}-Dimensional Hilbert Space,* Physical Review Letters **123** (2019) 250503.

[25] F. Lenzini, B. Haylock, J. C. Loredo, R. A. Abrahño, N. A. Zakaria, S. Kasture, I. Sagnes, A. Lemaitre, H.-P. Phan, D. V. Dao, P. Senellart, M. P. Almeida, A. G. White, and M. Lobino, *Active demultiplexing of single photons from a solid-state source,* Laser & Photonics Reviews **11** (2017) 1770034.

[26] A. Aspect, P. Grangier, and G. Roger, *Experimental Tests of Realistic Local Theories via Bell's Theorem,* Physical Review Letters **47** (1981) 460.

[27] A. Aspect, P. Grangier, and G. Roger, *Experimental Realization of Einstein-Podolsky-Rosen-Bohm Gedankenexperiment: A New Violation of Bell's Inequalities,* Physical Review Letters **49** (1982) 91.

[28] D. N. Klyshko, A. N. Penin, and B. F. Polkovnikov, *Parametric Luminescence and Light Scattering by Polaritons,* Soviet Journal of Experimental and Theoretical Physics Letters **11** (1970) 5.

[29] D. C. Burnham and D. L. Weinberg, *Observation of Simultaneity in Parametric Production of Optical Photon Pairs,* Physical Review Letters **25** (1970) 84.

[30] D. Boschi, S. Branca, F. De Martini, L. Hardy, and S. Popescu, *Experimental Realization of Teleporting an Unknown Pure Quantum State via Dual Classical and Einstein-Podolsky-Rosen Channels,* Physical Review Letters **80** (1998) 1121.

[31] J.-W. Pan, D. Bouwmeester, M. Daniell, H. Weinfurter, and A. Zeilinger, *Experimental test of quantum nonlocality in three-photon Greenberger-Horne-Zeilinger entanglement,* Nature **403** (2000) 515.

[32] H.-S. Zhong, Y. Li, W. Li, L.-C. Peng, Z.-E. Su, Y. Hu, Y.-M. He, X. Ding, W. Zhang, H. Li, L. Zhang, Z. Wang, L. You, X.-L. Wang, X. Jiang, L. Li, Y.-A. Chen, N.-L. Liu, C.-Y. Lu, and J.-W. Pan, *12-Photon Entanglement and Scalable Scattershot Boson Sampling with Optimal Entangled-Photon Pairs from Parametric Down-Conversion,* Physical Review Letters **121** (2018) 250505.

[33] C. K. Hong, Z. Y. Ou, and L. Mandel, *Measurement of subpicosecond time intervals between two photons by interference,* Phys. Rev. Lett. **59** (1987) 2044.

[34] G. N. Gol'tsman, O. Okunev, G. Chulkova, A. Lipatov, A. Semenov, K. Smirnov, B. Voronov, A. Dzardanov, C. Williams, and R. Sobolewski, *Picosecond superconducting single-photon optical detector,* Applied Physics Letters **79** (2001) 705.

[35] A. D. Semenov, G. N. Gol'tsman, and A. A. Korneev, *Quantum detection by current carrying superconducting film,* Physica C: Superconductivity **351** (2001) 349 .

[36] C. M. Natarajan, M. G. Tanner, and R. H. Hadfield, *Superconducting nanowire single-photon detectors: physics and applications,* Superconductor Science and Technology **25** (2012) 063001.

[37] W. Zhang, J. Huang, C. Zhang, L. You, C. Lv, L. Zhang, H. Li, Z. Wang, and X. Xie, *A 16-Pixel Interleaved Superconducting Nanowire Single-Photon Detector Array With A Maximum Count Rate Exceeding 1.5 GHz,* IEEE Transactions on Applied Superconductivity **29** (2019) 1.

[38] D. Gottesman and I. L. Chuang, *Demonstrating the viability of universal quantum computation using teleportation and single-qubit operations,* Nature **402** (1999) 390.

[39] M. A. Nielsen, *Quantum computation by measurement and quantum memory,* Physics Letters A **308** (2003) 96 .

[40] D. W. Leung, *Quantum Computation By Measurements,* International Journal of Quantum Information **02** (2004) 33.

[41] D. W. Leung. *Two-qubit Projective Measurements are Universal for Quantum Computation,* 2001.

[42] R. Raussendorf and H. J. Briegel. *Quantum computing via measurements only,* 2000.

[43] R. Raussendorf, D. E. Browne, and H. J. Briegel, *Measurement-based quantum computation on cluster states,* Physcal Review A **68** (2003) 022312.

[44] P. G. Kwiat and R. Y. Chiao, *Observation of a nonclassical Berry's phase for the photon,* Physical Review Letters **66** (1991) 588.

[45] S. Fasel, O. Alibart, S. Tanzilli, P. Baldi, A. Beveratos, N. Gisin, and H. Zbinden, *High-quality asynchronous heralded single-photon source at telecom wavelength,* New Journal of Physics **6** (2004) 163.

[46] Q. Wang, W. Chen, G. Xavier, M. Swillo, T. Zhang, S. Sauge, M. Tengner, Z.-F. Han, G.-C. Guo, and A. Karlsson, *Experimental Decoy-State Quantum Key Distribution with a Sub-Poissionian Heralded Single-Photon Source,* Physical Review Letters **100** (2008).

[47] T. Zhong, X. Hu, F. N. C. Wong, K. K. Berggren, T. D. Roberts, and P. Battle, *High-quality fiber-optic polarization entanglement distribution at 1.3âĂĽμm telecom wavelength,* Opt. Lett. **35** (2010) 1392.

[48] S. Takeuchi, R. Okamoto, and K. Sasaki, *High-yield single-photon source using gated spontaneous parametric downconversion,* Applied Optics **43** (2004) 5708.

[49] G. Brida, I. P. Degiovanni, M. Genovese, A. Migdall, F. Piacentini, S. V. Polyakov, and I. R. Berchera, *Experimental realization of a low-noise heralded single-photon source,* Optics Express **19** (2011) 1484.

[50] J. Rarity, P. Tapster, and E. Jakeman, *Observation of sub-Poissonian light in parametric downconversion,* Optics Communications **62** (1987) 201.

[51] X.-s. Ma, S. Zotter, J. Kofler, T. Jennewein, and A. Zeilinger, *Experimental generation of single photons via active multiplexing,* Physcal Review A **83** (2011) 043814.

[52] B. J. Smith, P. Mahou, O. Cohen, J. S. Lundeen, and I. A. Walmsley, *Photon pair generation in birefringent optical fibers,* Opt. Express **17** (2009) 23589.

[53] A. Ling, J. Chen, J. Fan, and A. Migdall, *Mode expansion and Bragg filtering for a high-fidelity fiber-based photon-pair source,* Opt. Express **17** (2009) 21302.

[54] P. Senellart, G. Solomon, and A. White, *High-performance semiconductor quantum-dot single-photon sources,* Nature Nanotechnology **12** (2017) 1026.

[55] S. Unsleber, Y.-M. He, S. Gerhardt, S. Maier, C.-Y. Lu, J.-W. Pan, N. Gregersen, M. Kamp, C. Schneider, and S. HÃűfling, *Highly indistinguishable on-demand resonance fluorescence photons from a deterministic quantum dot micropillar device with 74Optics Express* **24** *(2016) 8539.*

[56] X. Ding, Y. He, Z.-C. Duan, N. Gregersen, M.-C. Chen, S. Unsleber, S. Maier, C. Schneider, M. Kamp, S. Höfling, C.-Y. Lu, and J.-W. Pan, On-Demand Single Photons with High Extraction Efficiency and Near-Unity Indistinguishability from a Resonantly Driven Quantum Dot in a Micropillar, *Phys. Rev. Lett.* **116** *(2016) 020401.*

[57] Y.-M. He, J. Liu, S. Maier, M. Emmerling, S. Gerhardt, M. Davanço, K. Srinivasan, C. Schneider, and S. Höfling, Deterministic implementation of a bright, on-demand single-photon source with near-unity indistinguishability via quantum dot imaging, *Optica* **4** *(2017) 802.*

[58] H. Wang, Z.-C. Duan, Y.-H. Li, S. Chen, J.-P. Li, Y.-M. He, M.-C. Chen, Y. He, X. Ding, C.-Z. Peng, C. Schneider, M. Kamp, S. Höfling, C.-Y. Lu, and J.-W. Pan, Near-Transform-Limited Single Photons from an Efficient Solid-State Quantum Emitter, *Phys. Rev. Lett.* **116** *(2016) 213601.*

[59] J. C. Loredo, N. A. Zakaria, N. Somaschi, C. Anton, L. de Santis, V. Giesz, T. Grange, M. A. Broome, O. Gazzano, G. Coppola, I. Sagnes, A. Lemaitre, A. Auffeves, P. Senellart, M. P. Almeida, and A. G. White, Scalable performance in solid-state single-photon sources, *Optica* **3** *(2016) 433.*

[60] J. Iles-Smith, D. P. S. McCutcheon, A. Nazir, and J. Mørk, Phonon scattering inhibits simultaneous near-unity efficiency and indistinguishability in semiconductor single-photon sources, *Nature Photonics* **11** *(2017) 521.*

[61] J. C. Loredo, M. A. Broome, P. Hilaire, O. Gazzano, I. Sagnes, A. Lemaitre, M. P. Almeida, P. Senellart, and A. G. White, Boson Sampling with Single-Photon Fock States from a Bright Solid-State Source, *Phys. Rev. Lett.* **118** *(2017) 130503.*

[62] H. Wang, Y. He, Y.-H. Li, Z.-E. Su, B. Li, H.-L. Huang, X. Ding, M.-C. Chen, C. Liu, J. Qin, J.-P. Li, Y.-M. He, C. Schneider, M. Kamp, C.-

Z. Peng, S. Höfling, C.-Y. Lu, and J.-W. Pan, High-efficiency multiphoton boson sampling, *Nature Photonics* **11** *(2017) 361.*

[63] *H. Wang, J. Qin, X. Ding, M.-C. Chen, S. Chen, X. You, Y.-M. He, X. Jiang, L. You, Z. Wang, C. Schneider, J. J. Renema, S. Höfling, C.-Y. Lu, and J.-W. Pan,* Boson Sampling with 20 Input Photons and a 60-Mode Interferometer in a 10^{14}-Dimensional Hilbert Space, *Phys. Rev. Lett.* **123** *(2019) 250503.*

[64] *A. Christ and C. Silberhorn,* Limits on the deterministic creation of pure single-photon states using parametric down-conversion, *Physical Review A* **85** *(2012) 023829.*

[65] *M. A. Broome, M. P. Almeida, A. Fedrizzi, and A. G. White,* Reducing multi-photon rates in pulsed down-conversion by temporal multiplexing, *Opt. Express* **19** *(2011) 22698.*

[66] *P. J. Mosley, J. S. Lundeen, B. J. Smith, P. Wasylczyk, A. B. U'Ren, C. Silberhorn, and I. A. Walmsley,* Heralded Generation of Ultrafast Single Photons in Pure Quantum States, *Physical Review Letters* **100** *(2008) 133601.*

[67] *F. Graffitti, D. Kundys, D. T. Reid, A. M. Brańczyk, and A. Fedrizzi,* Pure down-conversion photons through sub-coherence-length domain engineering, *Quantum Science and Technology* **2** *(2017) 035001.*

[68] *F. Graffitti, J. Kelly-Massicotte, A. Fedrizzi, and A. M. Bra ńczyk,* Design considerations for high-purity heralded single-photon sources, *Physical Review A* **98** *(2018) 053811.*

[69] *H. Xu, L. Pancheri, G.-F. D. Betta, and D. Stoppa,* Design and characterization of a p+/n-well SPAD array in 150nm CMOS process, *Opt. Express* **25** *(2017) 12765.*

[70] *D. H. Andrews, W. F. Brucksch, W. T. Ziegler, and E. R. Blanchard,* Attenuated Superconductors I. For Measuring Infra-Red Radiation, *Review of Scientific Instruments* **13** *(1942) 281.*

[71] *Example of commercially available visible to near infrared PMT for photon counting from Hamamatsu.*

[72] *Example of commercially available infrared PMT for photon counting from Hamamatsu.*

[73] *Example of commercially available thick junction SPAD from excelitas.*

[74] *Example of commercially available shallow junction SPAD from Micro Photon Devices.*

[75] *O. Thomas, Z. L. Yuan, J. F. Dynes, A. W. Sharpe, and A. J. Shields,* Efficient photon number detection with silicon avalanche photodiodes, *Applied Physics Letters* **97** *(2010) 031102.*

[76] *M. Akiba, K. Tsujino, and M. Sasaki,* Ultrahigh-sensitivity single-photon detection with linear-mode silicon avalanche photodiode, *Optics Letters* **35** *(2010) 2621.*

[77] *M. Ghioni, G. Armellini, P. Maccagnani, I. Rech, M. K. Emsley, and M. S. Ünlü,* Resonant-cavity-enhanced single photon avalanche diodes on double silicon-on-insulator substrates, *Journal of Modern Optics* **56** *(2009) 309.*

[78] *D. A. Kalashnikov, S. H. Tan, M. V. Chekhova, and L. A. Krivitsky,* Accessing photon bunching with a photon number resolving multi-pixel detector, *Optics Express* **19** *(2011) 9352.*

[79] *R. L. Rue, G. Davis, D. Pudvay, K. Costello, and V. Aebi,* Photon counting 1060-nm hybrid photomultiplier with high quantum efficiency, *IEEE Electron Device Letters* **20** *(1999) 126.*

[80] *M. J. Fitch, B. C. Jacobs, T. B. Pittman, and J. D. Franson,* Photon-number resolution using time-multiplexed single-photon detectors, *Physical Review A* **68** *(2003).*

[81] *M. Mičuda, O. Haderka, and M. Ježek,* High-efficiency photon-number-resolving multichannel detector, *Physical Review A* **78** *(2008).*

[82] *L. A. Jiang, E. A. Dauler, and J. T. Chang,* Photon-number-resolving detector with10bitsof resolution, *Physical Review A* **75** *(2007).*

[83] *G. Brida, I. P. Degiovanni, F. Piacentini, V. Schettini, S. V. Polyakov, and A. Migdall,* Scalable multiplexed detector system for high-rate telecom-band single-photon detection, *Review of Scientific Instruments* **80** *(2009) 116103.*

[84] *C. Gobby, Z. L. Yuan, and A. J. Shields,* Quantum key distribution over 122 km of standard telecom fiber, *Applied Physics Letters* **84** *(2004) 3762.*

[85] *A. R. Dixon, Z. L. Yuan, J. F. Dynes, A. W. Sharpe, and A. J. Shields,* Gigahertz decoy quantum key distribution with 1 Mbit/s secure key rate, *Optics Express* **16** *(2008) 18790.*

[86] *B. E. Kardynał, Z. L. Yuan, and A. J. Shields,* An avalanche-photodiode-based photon-number-resolving detector, *Nature Photonics* **2** *(2008) 425.*

[87] *A. Yoshizawa, R. Kaji, and H. Tsuchida,* Gated-mode single-photon detection at 1550 nm by discharge pulse counting, *Applied Physics Letters* **84** *(2004) 3606.*

[88] *X. Jiang, M. A. Itzler, B. Nyman, and K. Slomkowski.* Negative feedback avalanche diodes for near-infrared single-photon detection, *. In M. A. Itzler and J. C. Campbell, editors,* Advanced Photon Counting Techniques III. *SPIEMay 2009.*

[89] *K. Zhao, A. Zhang, Y. hwa Lo, and W. Farr,* InGaAs single photon avalanche detector with ultralow excess noise, *Applied Physics Letters* **91** *(2007) 081107.*

[90] *M. Fujiwara and M. Sasaki,* Direct measurement of photon number statistics at telecom wavelengths using a charge integration photon detector, *Applied Optics* **46** *(2007) 3069.*

[91] *H. Takesue, E. Diamanti, T. Honjo, C. Langrock, M. M. Fejer, K. Inoue, and Y. Yamamoto,* Differential phase shift quantum key distribution experiment over 105 km fibre, *New Journal of Physics* **7** *(2005) 232.*

[92] *M. A. Albota and F. N. C. Wong,* Efficient single-photon counting at 155 μ m by means of frequency upconversion, *Optics Letters* **29** *(2004) 1449.*

[93] *A. P. VanDevender and P. G. Kwiat,* Quantum transduction via frequency upconversion (Invited), *Journal of the Optical Society of America B* **24** *(2007) 295.*

[94] *H. Xu, L. Ma, A. Mink, B. Hershman, and X. Tang,* 1310-nm quantum key distribution system with up-conversion pump wavelength at 1550 nm, *Optics Express* **15** *(2007) 7247.*

[95] *S. Takeuchi, J. Kim, Y. Yamamoto, and H. H. Hogue,* Development of a high-quantum-efficiency single-photon counting system, *Applied Physics Letters* **74** *(1999) 1063.*

[96] *B. Baek, K. McKay, M. Stevens, J. Kim, H. Hogue, and S. W. Nam,* Single-Photon Detection Timing Jitter in a Visible Light Photon Counter, *IEEE Journal of Quantum Electronics* **46** *(2010) 991.*

[97] *P. G. Kwiat, A. M. Steinberg, R. Y. Chiao, P. H. Eberhard, and M. D. Petroff,* Absolute efficiency and time-response measurement of single-photon detectors, *Applied Optics* **33** *(1994) 1844.*

[98] *D. Rosenberg, J. W. Harrington, P. R. Rice, P. A. Hiskett, C. G. Peterson, R. J. Hughes, A. E. Lita, S. W. Nam, and J. E. Nordholt,* Long-Distance Decoy-State Quantum Key Distribution in Optical Fiber, *Physical Review Letters* **98** *(2007).*

[99] *A. E. Lita, A. J. Miller, and S. W. Nam,* Counting near-infrared single-photons with 95% efficiency, *Optics Express* **16** *(2008) 3032.*

[100] *A. E. Lita, B. Calkins, L. A. Pellochoud, A. J. Miller, S. Nam, B. Young, B. Cabrera, and A. Miller.* High-Efficiency Photon-Number-Resolving Detectors based on Hafnium Transition-Edge Sensors, *. AIP2009.*

[101] *D. Fukuda, G. Fujii, T. Numata, A. Yoshizawa, H. Tsuchida, H. Fujino, H. Ishii, T. Itatani, S. Inoue, and T. Zama,* Photon number resolving detection with high speed and high quantum efficiency, *Metrologia* **46** *(2009) S288.*

[102] *D. Fukuda, G. Fujii, T. Numata, K. Amemiya, A. Yoshizawa, H. Tsuchida, H. Fujino, H. Ishii, T. Itatani, S. Inoue, and T. Zama,* Titanium-based transition-edge photon number resolving detector with 98% detection efficiency with index-matched small-gap fiber coupling, *Optics Express* **19** *(2011) 870.*

[103] *H. Takesue, S. W. Nam, Q. Zhang, R. H. Hadfield, T. Honjo, K. Tamaki, and Y. Yamamoto,* Quantum key distribution over a 40-dB channel loss using superconducting single-photon detectors, *Nature Photonics* **1** *(2007) 343.*

[104] *K. M. Rosfjord, J. K. W. Yang, E. A. Dauler, A. J. Kerman, V. Anant, B. M. Voronov, G. N. Gol'tsman, and K. K. Berggren,* Nanowire single-photon detector with an integrated optical cavity and anti-reflection coating, *Optics Express* **14** *(2006) 527.*

[105] *A. Divochiy, F. Marsili, D. Bitauld, A. Gaggero, R. Leoni, F. Mattioli, A. Korneev, V. Seleznev, N. Kaurova, O. Minaeva, G. Gol'tsman, K. G. Lagoudakis, M. Benkhaoul, F. Lévy, and A. Fiore,* Superconducting nanowire photon-number-resolving detector at telecommunication wavelengths, *Nature Photonics* **2** *(2008) 302.*

[106] *A. Peacock, P. Verhoeve, N. Rando, A. van Dordrecht, B. G. Taylor, C. Erd, M. A. C. Perryman, R. Venn, J. Howlett, D. J. Goldie, J. Lumley, and M. Wallis,* Single optical photon detection with a superconducting tunnel junction, *Nature* **381** *(1996) 135.*

[107] *A. Peacock, P. Verhoeve, N. Rando, A. van Dordrecht, B. G. Taylor, C. Erd, M. A. C. Perryman, R. Venn, J. Howlett, D. J. Goldie, J. Lumley, and M. Wallis,* On the detection of single optical photons with superconducting tunnel junction, *Journal of Applied Physics* **81** *(1997) 7641.*

[108] *T. Peacock, P. Verhoeve, N. Rando, C. Erd, M. Bavdaz, B. G. Taylor, and D. Perez,* Recent developments in superconducting tunnel junctions for ultraviolet, optical & near infrared astronomy, *Astronomy and Astrophysics Supplement Series* **127** *(1998) 497.*

[109] *J. C. Blakesley, P. See, A. J. Shields, B. E. Kardynał, P. Atkinson, I. Farrer, and D. A. Ritchie,* Efficient Single Photon Detection by Quantum Dot Resonant Tunneling Diodes, *Physical Review Letters* **94** *(2005).*

[110] *E. J. Gansen, M. A. Rowe, M. B. Greene, D. Rosenberg, T. E. Harvey, M. Y. Su, R. H. Hadfield, S. W. Nam, and R. P. Mirin,* Photon-number-discriminating detection using a quantum-dot, optically gated, field-effect transistor, *Nature Photonics* **1** *(2007) 585.*

[111] *M. A. Rowe, E. J. Gansen, M. Greene, R. H. Hadfield, T. E. Harvey, M. Y. Su, S. W. Nam, R. P. Mirin, and D. Rosenberg,* Single-photon detection using a quantum dot optically gated field-effect transistor with high internal quantum efficiency, *Applied Physics Letters* **89** *(2006) 253505.*

[112] *M. A. Rowe, G. M. Salley, E. J. Gansen, S. M. Etzel, S. W. Nam, and R. P. Mirin,* Analysis of photoconductive gain as it applies to single-photon detection, *Journal of Applied Physics* **107** *(2010) 063110.*

[113] *M. D. Eisaman, J. Fan, A. Migdall, and S. V. Polyakov,* Invited Review Article: Single-photon sources and detectors, *Review of Scientific Instruments* **82** *(2011) 071101.*

[114] *M. Barbieri, T. Weinhold, B. Lanyon, A. Gilchrist, K. Resch, M. Almeida, and A. White,* Parametric downconversion and optical quantum gates: two's company, four's a crowd, *Journal of Modern Optics* **56** *(2009) 209.*

[115] *M. Collins, C. Xiong, I. Rey, T. Vo, J. He, S. Shahnia, C. Reardon, T. Krauss, M. Steel, A. Clark, and B. Eggleton,* Integrated spatial multiplexing of heralded single-photon sources, *Nature Communications* **4** *(2013).*

[116] *X. Zhang, I. Jizan, J. He, A. S. Clark, D.-Y. Choi, C. J. Chae, B. J. Eggleton, and C. Xiong,* Enhancing the heralded single-photon rate from a silicon nanowire by time and wavelength division multiplexing pump pulses, *Opt. Lett.* **40** *(2015) 2489.*

[117] *F. Kaneda, B. G. Christensen, J. J. Wong, H. S. Park, K. T. McCusker,*

and P. G. Kwiat, Time-multiplexed heralded single-photon source, *Optica* **2** (2015) 1010.

[118] R.-B. Jin, R. Shimizu, I. Morohashi, K. Wakui, M. Takeoka, S. Izumi, T. Sakamoto, M. Fujiwara, T. Yamashita, S. Miki, H. Terai, Z. Wang, and M. Sasaki, Efficient generation of twin photons at telecom wavelengths with 2.5 GHz repetition-rate-tunable comb laser, *Scientific Reports* **4** *(2014)*.

[119] E. Pomarico, B. Sanguinetti, T. Guerreiro, R. Thew, and H. Zbinden, MHz rate and efficient synchronous heralding of single photons at telecom wavelengths, *Opt. Express* **20** *(2012) 23846.*

[120] G. J. Mendoza, R. Santagati, J. Munns, E. Hemsley, M. Piekarek, E. Martín-López, G. D. Marshall, D. Bonneau, M. G. Thompson, and J. L. O'Brien, Active temporal and spatial multiplexing of photons, *Optica* **3** *(2016) 127.*

[121] P. P. Rohde, L. G. Helt, M. J. Steel, and A. Gilchrist, Multiplexed single-photon-state preparation using a fiber-loop architecture, *Physical Review A* **92** *(2015) 053829.*

[122] R. A. Hoggarth, R. J. A. Francis-Jones, and P. J. Mosley, Resource-efficient fibre-integrated temporal multiplexing of heralded single photons, *Journal of Optics* **19** *(2017) 125503.*

[123] S. A. Castelletto, I. P. Degiovanni, V. Schettini, and A. L. Migdall, Reduced deadtime and higher rate photon-counting detection using a multiplexed detector array, *Journal of Modern Optics* **54** *(2007) 337.*

[124] M. T. Liu and H. C. Lim, Efficient heralding of O-band passively spatial-multiplexed photons for noise-tolerant quantum key distribution, *Opt. Express* **22** *(2014) 23261.*

[125] A. M. Smith, D. B. Uskov, L. H. Ying, and L. Kaplan, Imperfect linear-optical photonic gates with number-resolving photodetection, *Physical Review A* **84** *(2011) 032341.*

[126] D. Bonneau, G. J. Mendoza, J. L. O'Brien, and M. G. Thompson, Effect of loss on multiplexed single-photon sources, *New Journal of Physics* **17** *(2015) 043057.*

[127] M. Takeoka, R.-B. Jin, and M. Sasaki, Full analysis of multi-photon pair effects in spontaneous parametric down conversion based photonic quantum information processing, *New Journal of Physics* **17** *(2015) 043030.*

[128] R. J. A. Francis-Jones and P. J. Mosley. Temporal Loop Multiplexing: A resource efficient scheme for multiplexed photon-pair sources, *2015.*

[129] T. Jennewein, M. Barbieri, and A. G. White, Single-photon device requirements for operating linear optics quantum computing outside the post-selection basis, *Journal of Modern Optics* **58** *(2011) 276.*

[130] M. Avenhaus, H. B. Coldenstrodt-Ronge, K. Laiho, W. Mauerer, I. A. Walmsley, and C. Silberhorn, Photon Number Statistics of Multimode Parametric Down-Conversion, *Physical Review Letters* **101** *(2008) 053601.*

[131] P. Kok, W. J. Munro, K. Nemoto, T. C. Ralph, J. P. Dowling, and G. J. Milburn, Linear optical quantum computing with photonic qubits, *Review of Modern Physics* **79** *(2007) 135.*

[132] A. L. Migdall, D. Branning, and S. Castelletto, Tailoring single-photon and multiphoton probabilities of a single-photon on-demand source, *Physical Review A* **66** *(2002) 053805.*

[133] A. L. Migdall, D. A. Branning, S. Castelletto, and M. Ware. Single photon source with individualized single photon certifications, . *In J. C. Ricklin and D. G. Voelz, editors,* Free-Space Laser Communication and Laser Imaging II*volume 4821 455 . International Society for Optics and PhotonicsSPIE2002.*

[134] P. Adam, M. Mechler, I. Santa, and M. Koniorczyk, Optimization of periodic single-photon sources, *Physical Review A* **90** *(2014) 053834.*

[135] X.-s. Ma, S. Zotter, J. Kofler, T. Jennewein, and A. Zeilinger, Experimental generation of single photons via active multiplexing, *Physical Review A* **83** *)* *043814.*

[136] *R. J. A. Francis-Jones and P. J. Mosley.* Exploring the limits of multiplexed photon-pair sources for the preparation of pure single-photon states, *2014.*

[137] *F. Kaneda, F. Xu, J. Chapman, and P. G. Kwiat,* Quantum-memory-assisted multi-photon generation for efficient quantum information processing, *Optica* **4** *(2017) 1034.*

[138] *L. A. Ngah, O. Alibart, L. Labonté, V. D'Auria, and S. Tanzilli,* Ultra-fast heralded single photon source based on telecom technology, *Laser & Photonics Reviews* **9** *(2015) L1.*

[139] *X. Zhang, Y. H. Lee, B. A. Bell, P. H. W. Leong, T. Rudolph, B. J. Eggleton, and C. Xiong,* Indistinguishable heralded single photon generation via relative temporal multiplexing of two sources, *Opt. Express* **25** *(2017) 26067.*

[140] *M. Gimeno-Segovia, H. Cable, G. J. Mendoza, P. Shadbolt, J. W. Silverstone, J. Carolan, M. G. Thompson, J. L. O'Brien, and T. Rudolph,* Relative multiplexing for minimising switching in linear-optical quantum computing, *New Journal of Physics* **19** *(2017) 063013.*

[141] *I. Sobol,* Global sensitivity indices for nonlinear mathematical models and their Monte Carlo estimates, *Mathematics and Computers in Simulation* **55** *(2001) 271 .*

[142] *C. Greganti, P. Schiansky, I. A. Calafell, L. M. Procopio, L. A. Rozema, and P. Walther,* Tuning single-photon sources for telecom multi-photon experiments, *Opt. Express* **26** *(2018) 3286.*

[143] *D. Kumoor.* TTag, .

[144] *Y.-P. Huang and P. Kumar,* Mode-resolved photon counting via cascaded quantum frequency conversion, *Opt. Lett.* **38** *(2013) 468.*

[145] *V. Ansari, J. M. Donohue, M. Allgaier, L. Sansoni, B. Brecht, J. Roslund, N. Treps, G. Harder, and C. Silberhorn,* Tomography and Purification of the Temporal-Mode Structure of Quantum Light, *Physical Review Letters* **120** *(2018) 213601.*

[146] *D. V. Reddy and M. G. Raymer,* High-selectivity quantum pulse gating of photonic temporal modes using all-optical Ramsey interferometry, *Optica* **5** *(2018) 423.*

[147] *I. Jizan, B. Bell, L. G. Helt, A. C. Bedoya, C. Xiong, and B. J. Eggleton,* Phase-sensitive tomography of the joint spectral amplitude of photon pair sources, *Opt. Lett.* **41** *(2016) 4803.*

[148] *A. O. C. Davis, V. Thiel, and B. J. Smith.* Measuring the quantum state of a photon pair entangled in frequency and time, *2018.*

[149] *I. Gianani,* Robust spectral phase reconstruction of time-frequency entangled bi-photon states, *Physical Review Research* **1** *(2019) 033165.*

[150] *C. Chen, C. Bo, M. Y. Niu, F. Xu, Z. Zhang, J. H. Shapiro, and F. N. C. Wong,* Efficient generation and characterization of spectrally factorable biphotons, *Opt. Express* **25** *(2017) 7300.*

[151] *M. Liscidini and J. E. Sipe,* Stimulated Emission Tomography, *Physical Review Letters* **111** *(2013) 193602.*

[152] *A. Eckstein, G. Boucher, A. Lemaître, P. Filloux, I. Favero, G. Leo, J. E. Sipe, M. Liscidini, and S. Ducci,* High-resolution spectral characterization of two photon states via classical measurements, *Laser & Photonics Reviews* **8** *(2014) L76.*

[153] *M. Avenhaus, A. Eckstein, P. J. Mosley, and C. Silberhorn,* Fiber-assisted single-photon spectrograph, *Opt. Lett.* **34** *(2009) 2873.*

[154] *R.-B. Jin, R. Shimizu, K. Wakui, H. Benichi, and M. Sasaki,* Widely tunable single photon source with high purity at telecom wavelength, *Opt. Express* **21** *(2013) 10659.*

[155] *P. G. Evans, R. S. Bennink, W. P. Grice, T. S. Humble, and J. Schaake,* Bright Source of Spectrally Uncorrelated Polarization-Entangled Photons with Nearly Single-Mode Emission, *Physical Review Letters.* **105** *(2010) 253601.*

[156] *B. Brecht, D. V. Reddy, C. Silberhorn, and M. G. Raymer,* Photon Temporal Modes: A Complete Framework for Quantum Information Science, *Physical Review X* **5** *(2015) 041017.*

[157] *M. Kues, C. Reimer, P. Roztocki, L. R. Cortés, S. Sciara, B. Wetzel, Y. Zhang, A. Cino, S. T. Chu, B. E. Little, D. J. Moss, L. Caspani, J. Azaña, and R. Morandotti,* On-chip generation of high-dimensional entangled quantum states and their coherent control, *Nature* **546** *(2017) 622.*

[158] *H.-H. Lu, J. M. Lukens, N. A. Peters, B. P. Williams, A. M. Weiner, and P. Lougovski,* Quantum interference and correlation control of frequency-bin qubits, *Optica* **5** *(2018) 1455.*

[159] *V. Ansari, J. M. Donohue, B. Brecht, and C. Silberhorn,* Tailoring nonlinear processes for quantum optics with pulsed temporal-mode encodings, *Optica* **5** *(2018) 534.*

[160] *P. Imany, J. A. Jaramillo-Villegas, M. S. Alshaykh, J. M. Lukens, O. D. Odele, A. J. Moore, D. E. Leaird, M. Qi, and A. M. Weiner,* High-dimensional optical quantum logic in large operational spaces, *npj Quantum Information* **5** *(2019) 59.*

[161] *Q. Ding, R. Chatterjee, Y. Huang, and T. Yu.* High-dimensional temporal mode propagation in a turbulent environment, *2019.*

[162] *A. Eckstein, B. Brecht, and C. Silberhorn,* A quantum pulse gate based on spectrally engineered sum frequency generation, *Opt. Express* **19** *(2011) 13770.*

[163] *D. L. P. Vitullo, M. G. Raymer, B. J. Smith, M. Karpiński, L. Mejling, and K. Rottwitt,* Entanglement swapping for generation of heralded time-frequency-entangled photon pairs, *Physical Review A* **98** *(2018) 023836.*

[164] *W. H. Richardson,* Bayesian-Based Iterative Method of Image Restoration∗, *J. Opt. Soc. Am.* **62** *(1972) 55.*

[165] *L. B. Lucy,* An iterative technique for the rectification of observed distributions, *The Astronomical Journal* **79** *(1974) 745.*